

Department of Physics  
University of Lecce

---



Ph.D. Thesis

# **Ion implantation via a laser ion source**

Ph.D. Student:

Fabio Belloni

Tutor: Prof. V. Nassisi

---

XVIII Course (2003 - 2006)

# TABLE OF CONTENTS

<b>ABSTRACT</b> .....	3
<b>ABSTRACT (in lingua italiana)</b> .....	5
<b>PREFACE</b> .....	7
<b>1. INTRODUCTION</b>	
1.1 Laser ion sources.....	13
1.2 Conventional ion implantation techniques.....	15
1.3 Ion implantation from ablation plasma.....	16
1.4 Comparison between conventional techniques and LIS implantation.....	18
1.5 Potential applications.....	20
<b>2. THEORY</b>	
2.1 Phenomenology of the plasma plume.....	22
2.2 Ion-substrate interaction: basic concepts and considerations.....	29
2.3 Simulation of the ion implant.....	32
<b>3. EXPERIMENTAL</b>	
3.1 Experimental apparatus.....	33
3.2 Ion beam diagnostics.....	36
3.3 Analysis of the implanted samples.....	42
<b>4. RESULTS AND DISCUSSION ON ION DIAGNOSTICS AND     IMPLANTATION</b>	
4.1 Ion charge state abundance.....	46
4.2 Ion fluence.....	49
4.3 Ion range distribution.....	55
4.4 SEM-EDX analysis.....	61
4.5 RBS analysis.....	62

4.6	XPS analysis.....	64
4.7	LA-ICP-MS analysis.....	65
4.8	Further analyses by LA-ICP-MS.....	68
<b>5.</b>	<b>A NOVEL FAST PULSER BY TRANSMISSION LINES FOR ION EXTRACTION</b>	
5.1	Introduction.....	71
5.2	Basic theory.....	72
5.3	Experimental design.....	76
5.4	Analytical treatment.....	79
5.5	Simulation.....	82
5.6	Experimental apparatus and results.....	84
5.7	Discussion.....	86
<b>6.</b>	<b>CONCLUSIONS</b>	
6.1	Summary of the main results.....	87
6.2	Performances.....	90
6.3	Further developments.....	92
6.4	Further potential applications of LISs.....	94
	<b>APPENDIX</b>	
A.1	Introduction.....	95
A.2	Mathematical foundations.....	95
A.3	Experimental implementation.....	99
	<b>REFERENCES.....</b>	<b>103</b>
	<b>LIST OF THE MAIN ABBREVIATIONS.....</b>	<b>108</b>
	<b>ACKNOWLEDGEMENTS.....</b>	<b>109</b>

## ABSTRACT

A novel ion implantation technique, using laser ablation induced plasma as ion source, has been investigated in the present work. A compact and versatile laser ion source (LIS) was set up, characterized and tested. Experiments are reported, aimed at demonstrating the feasibility of ion implantation via LIS, at tens - hundreds keV energies.

An excimer laser (KrF, 248 nm wavelength, 70 mJ/pulse and 23 ns FWHM pulse duration) was pulsed on solid targets, in order to allow the generation of an expanding plasma bunch. Typically, the laser beam was focused in a 1 mm<sup>2</sup> spot, resulting in an irradiance of about  $3.5 \cdot 10^8$  W/cm<sup>2</sup>. By applying a high voltage on the LIS accelerating gap, ions were extracted from the ablated plasma and accelerated towards a substrate. The occurrence of arcs during the extraction stage was a major challenge that could be overcome employing a specifically-designed plasma expansion chamber. Such a set-up allowed to apply the high voltage in DC mode. Moreover, it is also proposed the use of a novel pulser to apply the accelerating voltage in AC mode, generating single or repeated high voltage fast pulses. Implantations of Al, Cu and Ge on Si substrates were carried out, operating at tens kV DC acceleration voltage and 1 Hz laser repetition rate.

Assuming a phenomenological model for the plasma plume, useful equations were derived for several physical quantities of interest in ion diagnostics, extraction and implantation. The abundance and the energy distribution of the various ion charge states produced in the laser plasma were characterized by means of electrostatic mass-to-charge spectrometers. Charge states up to +3 were revealed. The ion fluence was estimated using Faraday cup diagnostics, both on the free expanding plasma and on the accelerated beam, and was in the order of  $10^{10} - 10^{12}$  ions/cm<sup>2</sup> per pulse, depending on the ablated material. Ion doses ranging from  $10^{13}$  to  $10^{14}$  ions/cm<sup>2</sup> were implanted.

The implanted samples were characterized by means of several analytical techniques, commissioned to various national and foreign laboratories: SEM-EDX, Rutherford backscattering spectrometry (RBS), X-ray photo-electron spectrometry (XPS) and laser ablation – inductively coupled plasma – mass spectrometry (LA-ICP-MS). Analyses showed that neutral atoms were deposited and ions were implanted at

energies of tens keV per charge state unit. An implantation range larger than 100 nm was typically measured for all the implants, in good agreement with Monte Carlo simulations of the depth profiles. Furthermore, a parallel study on the LA-ICP-MS performances in the sub- $\mu\text{m}$  depth range was carried out, with a view to implementing on-site analysis of the implanted samples.

## **ABSTRACT (in lingua italiana)**

Nel presente lavoro è stata studiata una nuova tecnica di impiantazione ionica, basata sull'impiego, come sorgente di ioni, di plasma indotto per ablazione laser. È stata messa a punto, caratterizzata e testata una sorgente laser di ioni (LIS, "laser ion source") compatta e versatile. Gli esperimenti effettuati e qui riportati erano volti a dimostrare la fattibilità dell'impiantazione ionica via LIS, ad energie di decine – centinaia di keV.

Un fascio da laser ad eccimero (KrF, lunghezza d'onda di 248 nm, 70 mJ/impulso e durata dell'impulso di 23 ns FWHM) colpiva un bersaglio solido, generando un bunch di plasma in espansione. Il fascio laser era tipicamente focalizzato in uno spot di 1 mm<sup>2</sup>, dando luogo ad un'irradianza di circa  $3.5 \cdot 10^8$  W/cm<sup>2</sup>. Applicando un'alta tensione sulla gap di accelerazione della LIS, gli ioni erano estratti dal plasma ablato ed accelerati verso un substrato. Il verificarsi di scariche durante la fase di estrazione costituiva un notevole problema, che poté essere superato mediante l'impiego di una camera di espansione del plasma appositamente progettata. Tale set-up consentiva di applicare l'alta tensione in regime DC. Inoltre, si propone anche l'utilizzo di un nuovo impulsatore per applicare la tensione di accelerazione in regime AC, generando un singolo o ripetuti impulsi veloci d'alta tensione. Sono state effettuate impiantazioni di Al, Cu e Ge su substrati di Si, operando a tensioni d'accelerazione DC di decine di kV e ad una frequenza di ripetizione dell'impulso laser di 1 Hz.

Assumendo un modello fenomenologico per il plume di plasma, sono state derivate utili equazioni per diverse grandezze fisiche di interesse nella diagnostica, estrazione ed impiantazione di ioni. L'abbondanza e la distribuzione energetica dei vari stati di carica ionica prodotti nel laser plasma sono stati caratterizzati per mezzo di spettrometri elettrostatici massa/carica. Sono stati rivelati stati di carica fino a +3. La fluenza di ioni è stata valutata mediante diagnostica con coppa di Faraday, sia sul plasma in libera espansione che sul fascio accelerato, ed è risultata dell'ordine di  $10^{10} - 10^{12}$  ioni/cm<sup>2</sup> per shot, a seconda del materiale ablato. Le dosi ioniche impiantate variavano da  $10^{13}$  a  $10^{14}$  ioni/cm<sup>2</sup>.

I campioni impiantati sono stati caratterizzati mediante diverse tecniche analitiche, commissionate a vari laboratori nazionali ed esteri: SEM-EDX, Rutherford

backscattering spectrometry (RBS), X-ray photo-electron spectrometry (XPS) e laser ablation – inductively coupled plasma – mass spectrometry (LA-ICP-MS). Le analisi mostravano che gli atomi neutri venivano depositati e gli ioni venivano impiantati ad energie di decine di keV per unità di carica. Un range di impiantazione superiore a 100 nm era tipicamente misurato in tutti gli impianti, in buon accordo con le simulazioni Monte Carlo dei profili di profondità. Inoltre, è stato effettuato uno studio parallelo sulle performance della LA-ICP-MS nel range di profondità sub- $\mu\text{m}$ , con il proposito di implementare l'analisi *on-site* dei campioni impiantati.

## PREFACE

The present work was carried out from 2003 to 2006 within the PLAIA (Plasma Laser Ablation for Ion Acceleration) project, supported by the Fifth Committee of INFN (Istituto Nazionale di Fisica Nucleare), the Italian National Institute for Nuclear Physics. The PLAIA project was a collaboration between “Laboratori Nazionali del Sud” – INFN (Catania), the Department of Physics of the University of Lecce and the INFN Sections of Lecce and Messina, with the partnership of several European research institutes. This project was intended to study the basic physics of non-equilibrium plasmas generated by different kinds of pulsed lasers. A special attention was devoted to the ion charge states, their energy distribution and the techniques for ion extraction from laser plasma, as well as the ion beam characterization. Moreover, the project aimed at applying the results of this investigation in three different fields:

- development of new ion sources;
- realization of an ion implanter via laser plasma;
- medical applications of laser ablation, ion implantation and ion beams (hadrontherapy).

The research activity reported in this thesis concerns the development and characterization of a laser ion source (LIS) for ion implantation. The main goal of the experiments is to demonstrate the feasibility of LIS implantation. The experimental activity was carried out mainly at the Laboratory of Applied Electronics (LEAS) of the Department of Physics of the University of Lecce; some experiments were carried out at Laboratori Nazionali del Sud – INFN (Catania). Furthermore, an EU “Marie Curie” fellowship at the Institute of Physics of the Academy of Sciences of the Czech Republic was spent for a phenomenological study about the development of deconvolution techniques, on the time-of-flight spectrum, aimed at analysing ion groups of different charge state in laser-produced plasma.

As a part of the present work or in parallel with it, a complete characterization of plasma produced from solid targets by means of excimer UV lasers (248 nm and 308 nm wavelength), in the power density range  $0.1 - 10 \text{ GW/cm}^2$ , was carried out at the Laboratory of Applied Electronics of the Department of Physics of Lecce. By the use of time-of-flight diagnostics and electrostatic spectrometers, measurements and

analyses were performed on plasma temperature and drift velocity, ion charge states, ion energy distribution, ion angular distribution, neutral component, electron component, and recombination effects. Ion extraction also was carefully investigated, as a function of the extraction voltage, by means of ion current measurements and time-of-flight spectrometry. Substantially similar results were obtained, at the same irradiance on the targets, for the two different laser wavelengths utilized, both on the free expanding plasma and on the extracted beam. Many of this information was indispensable to realize the compact experimental set-up for ion implantation illustrated in this dissertation.

A brief overview of the laser plasma physics, LIS implantation and conventional implantation techniques is presented in Chapter 1. LIS implantation consists substantially in extracting and accelerating against a substrate ions contained in the plasma plume produced by laser ablation of the material to be implanted. Such a technique could become competitive, in a wide range of applications, with respect to the conventional beamline implantation and the modern plasma immersion ion implantation.

A phenomenological picture of the plasma plume, particularly suitable for ion diagnostics, extraction and implantation, is reported in Chapter 2. Useful mathematical expressions are derived for several physical quantities of interest. Basic concepts and considerations about the ion beam - substrate interaction are reported as well.

Experimental issues are treated in Chapter 3. The experimental set-up for ion diagnostics and implantation is fully described. There the analytical techniques employed for the characterization of the implanted samples are also described.

The results of such analyses, together with the diagnostics of the implanting ion beam, are reported and discussed in Chapter 4. In this dissertation only the implantation experiments employing a KrF excimer laser (248 nm wavelength) are reported.

A Monte Carlo code, SRIM, was used to simulate the expected depth profiles. Materials analyses proved that plasma ions were accelerated and implanted. Particular attention was dedicated to the analysis by laser ablation in combination with inductively coupled plasma – mass spectrometry (LA-ICP-MS), not only for its affinity with many topics relevant for the research on LIS and ion implantation, but

also to investigate the possibility of implementing on-site analytical characterization of the implanted sample, in the same laser ablation system used to implant.

Moreover, it is also proposed the use of a novel pulser to apply the accelerating voltage in AC mode, generating single or repeated high voltage fast pulses. This “voltage compressor”, based on the utilisation of transmission lines, is able to halve the duration and to double the amplitude of a pulse in input. Its use can be indispensable when higher accelerating voltage values (quite a lot of tens kV) or higher ion flux values are required, if one wants to retain the simple extraction-implantation configuration here employed. Such a device has been realized at the Laboratory of Applied Electronics of the Department of Physics of Lecce and is fully described in Chapter 5.

Chapter 6 summarizes the work presented in this dissertation and the major conclusions of this research. Some suggestions for future work are also given. In particular, the use of a more sophisticated expansion chamber, only just realized, is proposed.

In the Appendix a method for LA-ICP-MS signal processing is proposed, with the aim of taking into account signal dispersion and pulse mixing effects in the assessment of the depth profile, especially in the sub- $\mu\text{m}$  depth range. In particular, an algorithm for pulse mixing deconvolution was developed; it processed the accumulated signal intensity due to pulse-on-pulse stacking, *i.e.*, the latest pulse on top of all the antecedent pulses, each one exponentially decreasing with time.

The present dissertation is mostly based on the author’s publications produced during the doctoral course. Some of these publications are reported below:

1. V. Nassisi, F. Belloni, D. Doria and A. Lorusso, “Novel voltage compressor circuit by transmission lines”, *Rev. Sci. Instrum.* **74**(12), 5201-5203 (2003).
2. V. Nassisi, F. Belloni, D. Doria and A. Lorusso, “High current compressor utilizing transmission lines”, *Meas. Sci. Technol.* **15**, 244-247 (2004).
3. D. Doria, A. Lorusso, F. Belloni and V. Nassisi, “Characterization of a nonequilibrium XeCl laser-plasma by a movable Faraday cup”, *Rev. Sci. Instrum.* **75**(2), 387-392 (2004).
4. F. Belloni, D. Doria, A. Lorusso and V. Nassisi, “Study of particle acceleration of Cu plasma”, *Rev. Sci. Instrum.* **75**(11), 4763 - 4768 (2004).
5. V. Nassisi, F. Belloni, D. Doria and A. Lorusso, “Temperature measurement by Maxwell-Boltzmann distribution of a plasma-laser and characterization of the ion

- beam”, in: “*Plasma Production by Laser Ablation (PPLA 2003)*”, S. Gammino, A. M. Mezzasalma, F. Neri, L. Torrisci, Eds., World Scientific Publishing, Singapore, 2004, pp. 127 - 132.
6. A. Lorusso, F. Belloni, D. Doria and V. Nassisi, “Study of the laser plasma by Faraday cups and characterization of the laser beam spot”, in: “*Plasma Production by Laser Ablation (PPLA 2003)*”, S. Gammino, A. M. Mezzasalma, F. Neri, L. Torrisci, Eds., World Scientific Publishing, Singapore, 2004, pp. 184 - 190.
  7. D. Doria, F. Belloni, A. Lorusso and V. Nassisi, “Energy distribution of the ions generated by a 308 nm laser beam”, in: “*Plasma Production by Laser Ablation (PPLA 2003)*”, S. Gammino, A. M. Mezzasalma, F. Neri, L. Torrisci, Eds., World Scientific Publishing, Singapore, 2004, pp. 170 - 176.
  8. F. Belloni, D. Doria, A. Lorusso and V. Nassisi, “Comparison of the plasma characteristics induced by excimer laser pulses of different width”, in: “*Plasma Production by Laser Ablation (PPLA 2003)*”, S. Gammino, A. M. Mezzasalma, F. Neri, L. Torrisci, Eds., World Scientific Publishing, Singapore, 2004, pp. 156 - 162.
  9. D. Doria, A. Lorusso, F. Belloni, V. Nassisi, L. Torrisci and S. Gammino, “A study of the parameters of particles ejected from a laser plasma”, *Laser Part. Beams* **22**, 461 - 467 (2004).
  10. F. Belloni, D. Doria, V. Nassisi and G. Palamà, “Fixed energy voltage compressor: theory, simulation and experiments”, *Nucl. Instrum. Meth. A* **537**(3), 614 – 620 (2005).
  11. A. Lorusso, J. Krása, K. Rohlena, V. Nassisi, F. Belloni and D. Doria, “Charge losses in expanding plasma created by a XeCl laser”, *Appl. Phys. Lett.* **86**, 081501 – 2 (2005).
  12. F. Belloni, D. Doria, A. Lorusso, V. Nassisi and L. Torrisci, “Study of Cu ions acceleration via UV laser ablation”, *Proc. SPIE Int. Soc. Opt. Eng.* **5777**, 974 - 977 (2005).
  13. F. Belloni, D. Doria, A. Lorusso and V. Nassisi, “Study of acceleration of Cu ions”, *Proceedings del XVII Congresso dell’Associazione Italiana del Vuoto*, Venezia Lido, Italy, June 28 – July 2, 2004, pp. 55 – 60.
  14. D. Doria, A. Lorusso, F. Belloni, V. Nassisi, L. Torrisci and S. Gammino, “Energy distribution of Cu ions generated by excimer laser ablation”, *Proceedings del XVII Congresso dell’Associazione Italiana del Vuoto*, Venezia Lido, Italy, June 28 – July 2, 2004, pp. 195 – 199.
  15. F. Belloni, D. Doria, A. Lorusso, V. Nassisi, L. Torrisci, L. Calcagnile, G. Quarta, D. Bleiner and D. Manno, “Characterization of ablation plasma ion implantation”, *Nucl. Instrum. Meth. B* **240**, 36 – 39 (2005).

16. A. Lorusso, F. Belloni, D. Doria, V. Nassisi, J. Wolowski, J. Badziak, P. Parys, J. Krása, L. Láska, F. P. Boody, L. Torrasi, A. Mezzasalma, A. Picciotto, S. Gammino, L. Calcagnile, G. Quarta and D. Bleiner, “Modification of materials by high energy plasma ions”, *Nucl. Instrum. Meth. B* **240**, 229 – 233 (2005).
17. F. Belloni, D. Doria, A. Lorusso and V. Nassisi “Results on particle acceleration of metal ions”, *Nucl. Instrum. Meth. B* **240**, 40 – 43 (2005).
18. D. Doria, A. Lorusso, F. Belloni and V. Nassisi, “On the dynamics of a non-equilibrium Cu plasma produced by an excimer laser interaction with a solid”, *J. Plasma Phys.* **72**(2), 229 – 239 (2006).
19. J. Krasa, A. Lorusso, D. Doria, F. Belloni, V. Nassisi and K. Rohlena, “Time-of-flight profile of multiply-charged ion currents produced by a pulse laser”, *Plasma Phys. Control. Fusion* **47**, 1339 – 1349 (2005).
20. D. Bleiner, F. Belloni, D. Doria, A. Lorusso and V. Nassisi, “Overcoming pulse mixing and signal tailing in laser ablation inductively coupled plasma mass spectrometry depth profiling”, *J. Anal. At. Spectrom.* **20**, 1337 – 1343 (2005).
21. A. Lorusso, F. Belloni, D. Doria, V. Nassisi, J. Krása and K. Rohlena, “Significant role of the recombination effects for a laser ion source”, *J. Phys. D: Appl. Phys.* **39**, 294 – 300 (2006).
22. L. Marra, F. Belloni, A. Lorusso, L. Martina and V. Nassisi, “A study of electron beams ejected from a plasma produced by a laser interaction with a solid target”, *Rad. Eff. Def. Solids* **160**, 621 – 629 (2005).
23. D. Doria, F. Belloni, A. Lorusso, J. Krása, V. Nassisi, K. Rohlena and L. Velardi, “Recombination effects during the laser-produced plasma expansion”, *Rad. Eff. Def. Solids* **160**, 663 – 668 (2005) .
24. F. Belloni, G. Caretto, A. Lorusso, V. Nassisi, A. Perrone and M.V. Siciliano, “Photo-emission studies from Zn cathodes under plasma phase”, *Rad. Eff. Def. Solids* **160**, 587 – 594 (2005).
25. F. Belloni, D. Doria, A. Lorusso, V. Nassisi and J. Krasa, “Pre- and post-extraction analyses of different charge state ion components produced in a laser ion source”, *Rev. Sci. Instrum.* **77**, 03B301 (2006).
26. F. Belloni, G. Buccolieri, A. Castellano, D. Doria, A. Lorusso and V. Nassisi, “Ab initio selective UV laser cleaning”, *Proc. SPIE Int. Soc. Opt. Eng.* **5777**, 932 - 935 (2005).
27. A. Lorusso, V. Nassisi, F. Belloni, G. Buccolieri, G. Caretto, A. Castellano, “Sulphur selective ablation by UV laser”, *Proc. SPIE* **5857**, 32 - 40 (2005).
28. F. Belloni, V. Nassisi, P. Alifano, C. Monaco, A. Talà, M. Tredici and A. Rainò, “A new technique by a suitable plane transmission line at 900 MHz RF fields for *E. coli* DNA studies”, *Rev. Sci. Instrum.* **76**, 0543021 - 6 (2005); republished as a “selected paper” in *Virtual Journal of Biological Physics Research*, **9**(9) (2005).

29. F. Belloni, D. Doria, A. Lorusso and V. Nassisi, “Novel pulse amplifying circuits by different characteristic impedance transmission lines”, *Nucl. Instrum. Meth. A* **556**, 296 - 301 (2006).
30. A. Talà, F. Belloni, C. Monaco, A. Lorusso, V. Nassisi and P. Alifano, “Effects of XeCl UV<sub>308nm</sub> laser radiation on survival and mutability of *recA*-proficient and *recA*-defective *Escherichia coli* strains”, *Rad. Res.* **165**, 532 – 537 (2006).
31. F. Belloni, V. Nassisi, P. Alifano, C. Monaco and S. Panzanaro, “The effects of UV laser radiation as sterilizer for cultural heritage”, *Macromolecular Symposia* **238**, 52 – 56 (2006).
32. F. Belloni, D. Doria, A. Lorusso, V. Nassisi, P. Alifano, C. Monaco, A. Talà, M. Tredici and A. Rainò, “Experimental analysis of a TEM plane transmission line for DNA studies at 900 MHz EM fields”, *J. Phys. D: Appl. Phys.* **39**, 2856 – 2861 (2006).
33. A. Lorusso, F. Belloni, D. Doria, V. Nassisi and L. Velardi, “Determination of recombination length of a non-equilibrium plasma produced by laser ablation”, *Nuovo Cimento C*, in press.

# 1. INTRODUCTION

## 1.1 Laser ion sources

A lot of new applications with ion beams, not only in research laboratories, but also in the fields of industry, engineering and medicine, have stimulated great interest in the development of novel ion sources, based on non-conventional techniques. Among these, it seems to be particularly promising the possibility of exploiting the interaction of high energy pulsed laser beams with the matter. In fact, pulsed laser irradiation has become a technique employed in the last few years for several purposes: from the ablation of targets to the deposition of thin films and from the plasma production to the high-energy ion acceleration.

Pulsed laser beams of high intensity allow the production of etched material, by acting directly on solid targets without the application of special devices for evaporation. Increasing the laser energy usually results in an exploding plasma plume consisting of highly concentrated electrons, ions and neutral particles. The plume, which is generally produced in a vacuum chamber, evolves in adiabatic expansion predominantly along the direction normal to the target surface, independently on the incidence angle of the laser beam. The emitted ions have a shifted Maxwell-Boltzmann velocity distribution [1-3], which moves towards higher energy as the ion charge state increases [4, 5]. Depending on the kind and parameters of the used laser, ions with charge states from +1 up to more than +50 can be produced, with ion energies ranging from hundreds of eV up to hundreds of MeV (with no external acceleration) [6]. As an example, at a laser power density of the order of  $10^{10}$  W/cm<sup>2</sup> and a laser pulse duration of 10 – 20 ns, an average kinetic energy of the order of 1 keV per charge state resulted for heavy ions in many experiments [7].

Ion energy is thought to be increased up to such values by two important processes which act separately on plasma temperature and drift velocity. Plasma temperature is enhanced by inverse-bremsstrahlung absorption of the laser light in a free – free transition of an electron – ion pair. Significant absorption occurs at plasma density of the order of  $10^{19}$  cm<sup>-3</sup>, a value generally found at distances below 50  $\mu$ m from the target in the first nanoseconds of plasma generation [8]. Plasma drift velocity is determined, apart from hydrodynamic effects acting on neutral atoms as well (*e.g.*, Knudsen-layer formation [1]), by the existence of a high electric field inside the

plasma itself, which accelerates the ions just in the first stage of the plume expansion. Preliminary evaluations of this field, obtained on the base of experimental data, indicated a value in the order of tens of MV/cm at the edge of the plasma core [7].

The ionization yield in the plume depends mainly on the high plasma temperature, can be enhanced by photoionization induced by the laser light or other plasma radiative processes (*e.g.*, soft X-rays generation), and is affected by ion – electron recombination processes occurring during the plume expansion [9]. The angular distributions of the different species composing the plasma plume are different and they usually exhibit a strong forward peaking. Higher charge state ions exhibit more forward peaked distributions and are concentrated at smaller angles. The abundance of each ion species decreases with increasing the charge state [10].

The peculiar characteristics of the laser-induced plasma bunch makes it an ideal candidate for ion production, extraction and acceleration. Ion sources based on laser plasma, or “laser ion sources” (LISs) have proved to be very efficient sources of highly charged ions and high current beams. Moreover, any solid material can be easily evaporated and ionized in a single step. Different demands on the kind, energy and yield of ions influence the laser choice, and, on the contrary, parameters and properties of the laser determine properties and parameter limits of the generated ions. With LIS, therefore, several variables can and must be controlled. The proportions of ions and neutrals, their angular and energy distributions, ion current densities and ion charge states are determined by the target material and the laser energy, pulse duration and intensity on the target. Generally, lasers with some repetition frequency are preferred for technical applications, while single shot lasers are used mainly for fundamental research.

LISs can be used for different purposes and applications, *e.g.*, for the preinjectors of large colliders [11, 12], for hybrid ion sources based on a combination of LIS and electron cyclotron resonance ion sources (ECRIS) [7], and for ion implantation, with [13, 14] or without [15] ion acceleration by means of an external electric field.

LIS ion implantation driven by an external electric field shows several interesting aspects and seems to have some advantages over the conventional ion implanters. Source characterization and implantation experiments are reported and discussed in the present study.

## 1.2 Conventional ion implantation techniques

The rapid growth in semiconductor performance, combined with the constant size reduction, has been pushed by the improvements in ion implantation technology. Ion implantation is a process by which ions are accelerated to a target at energies high enough to bury them below the target surface. In the early 1970s, it was found that ion implantation of metal surfaces could improve their wear, hardness, friction and corrosion properties [16-23].

Ion implantation has been traditionally done by means of ion gun facilities, where the setup extracts ions from the source, accelerates and focuses them into a beam, which is rastered over the target. Often the sample must be rotated and manipulated in the vacuum to insure all parts have been processed homogeneously. A schematic drawing of a typical ion implanter is reported in Fig. 1.1. The detail of its typical plasma source is reported in Fig. 1.2.

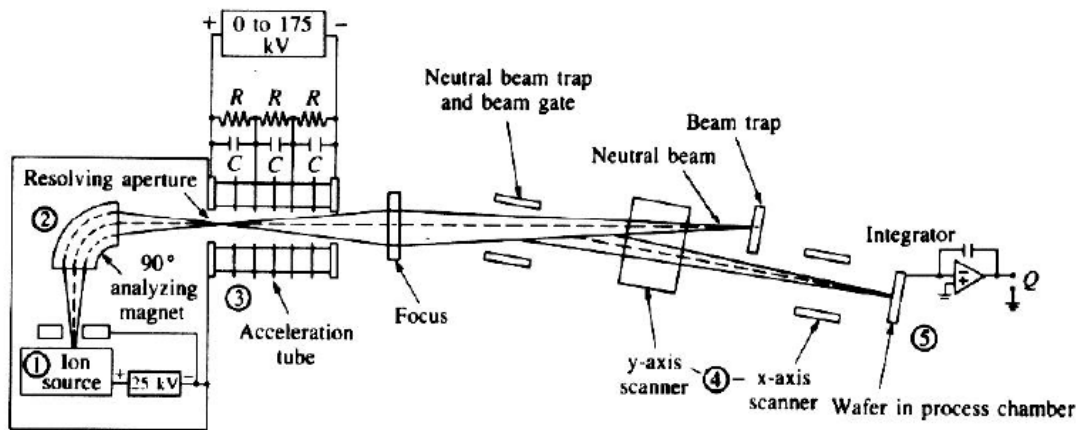


**Fig. 1.1.** Schematic drawing of a typical ion implanter, showing the ion source (1), the mass spectrometer (2), the high voltage accelerator column (3), the x- and y-axis deflection system (4), and the target chamber (5).

A recent advance in ion implantation technology is represented by plasma-immersion ion implantation (PIII) [23-28]. In this technique, the target is inside a plasma, and high voltage negative pulses drive ions toward the sample surface. Thus, all parts of the target are being implanted at normal incidence. The PIII technique has

been shown to be very efficient for the superficial modification of several materials, such as, for example, in the hardening of tools, in the ion implantation for semiconductor devices, in the improving of the properties of resistance to corrosion and wear of metals and alloys, and, most recently, in the improving of the biocompatibility of biomedical materials. Plasma is generated by thermionic cathodes, radiofrequency, microwaves, magnetron sputtering or vacuum arc discharges. From 80's many developments have been made in this field and also variations of such technique have been devised [29-34].

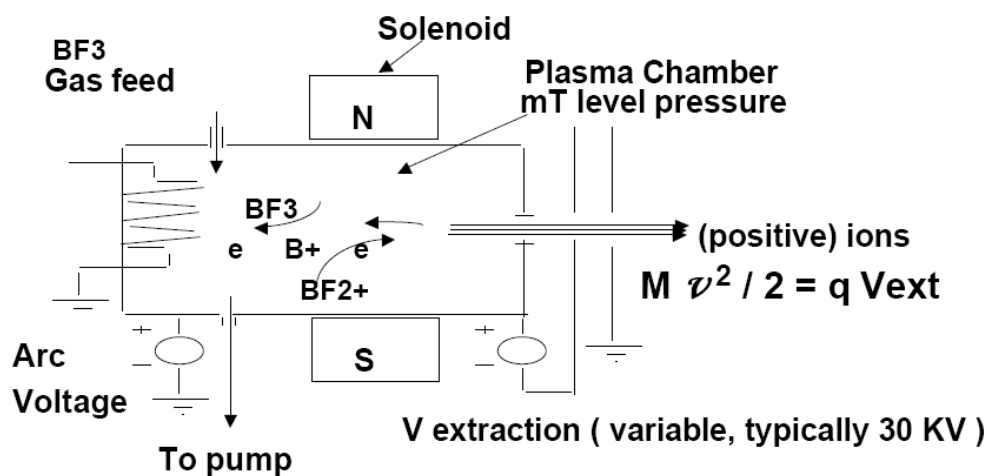


*Fig. 1.2. Schematic drawing of a typical plasma source for commercial ion implanters. Primary electrons causing discharge ionization are produced by the filament on the left side of the plasma chamber.*

### 1.3 Ion implantation from ablation plasma

Implantation of ions from laser-produced plasma has been demonstrated and described in recent papers [13, 14, 35-38]. In fact, the development of high intensity laser beams has allowed to improve the ion production by laser ablation. Moreover, laser ablation induces plasmas that have many interesting and peculiar characteristics for ion implantation, as discussed below.

Ablation plasma ions can be led against a substrate for direct ion implantation [36, 38] or by means of an accelerating voltage [13, 14]. Direct ion implantation needs

very high power laser systems and seems not very exploitable on a large scale from the commercial point of view, both for economical reasons and for performance flexibility (for example, fixed ion energy spectrum). Instead, the ablation plasma ion implantation driven by an external electric field appears to be a more easy-to-use, cheap and flexible technique.

In line of principle, two experimental configurations can be employed, as shown in Fig. 1.3:

- i. the standard orientation for pulsed laser deposition (PLD), in which the substrate and laser target surfaces are oriented parallel to one another (Fig. 1.3a);
- ii. the target is perpendicular to the substrate (Fig. 1.3b).

The physical basis of the orientation i) is that the ablation plume constituents (electrons, ions, neutral atoms and particulate) are ejected primarily perpendicularly to the target and the impact with the substrate occurs under the action of an external longitudinal electric field. So, neutral atoms are deposited and ions are implanted. In the configuration ii) electrons are expelled from the gap between target and substrate, reducing the occurrence of arcing. The negatively biased substrate accelerates the ablated ions, while extremely small ballistic deposition of neutral atoms and particulate is expected in this case, so achieving pure ion implantation.

The implantation method i) presents the disadvantage of formation of arcs during the acceleration process, especially when DC high voltage (HV) is used. This results in the lessening of fluence and depth of the implanted ions. A HV pulse, suitably delayed with respect to the laser pulse, was utilised for this geometry by Qi *et al.* [13] in order to avoid arcing between negatively biased substrate and target. Nevertheless, such a solution requires the application of a rather complex timing technique. An alternative approach was developed at the LEAS laboratory and employed in the present work, which allowed to get implantation by means of DC HV. This was accomplished inserting a specifically designed “expansion chamber” between target and extraction gap. The efforts done to avoid arcs are fully reported in Chapter 3.

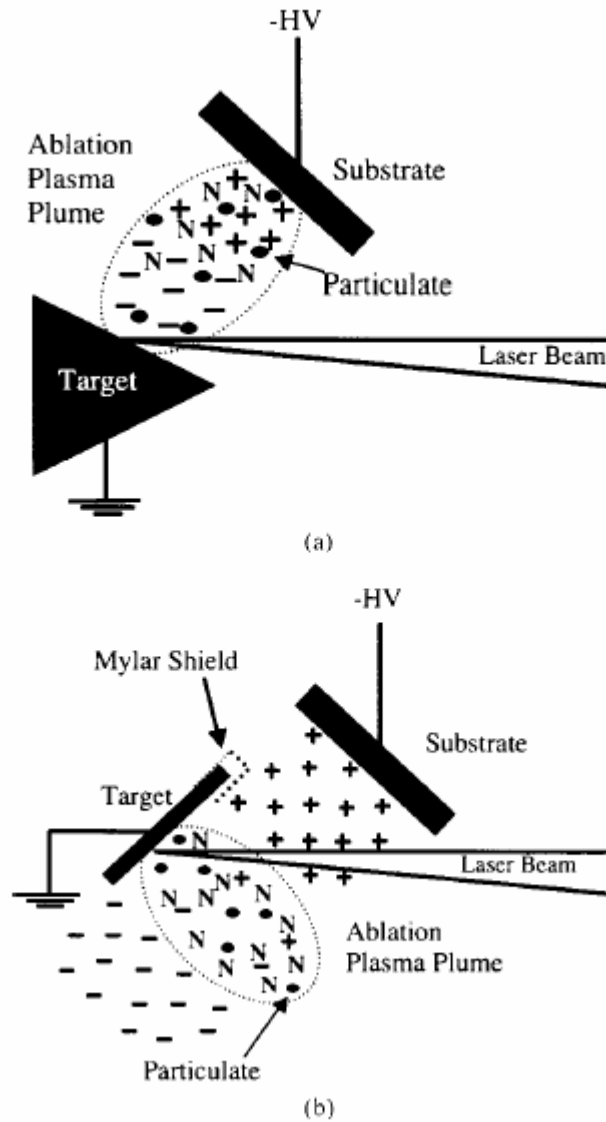


*Fig. 1.3. Experimental configurations for two geometries of ablation plasma ion implantation: target parallel to substrate (a) and target perpendicular to substrate (b). Reproduced from Qi et al. [22].*

#### 1.4 Comparison between conventional techniques and LIS implantation

Ion implantation via LIS could be competitive in a wide range of applications with respect to the conventional implantation techniques. First of all, laser ablation of materials can generate a significant amount of ions for implantation. As a consequence, LIS implantation can achieve high dose rates, improving the implantation efficiency. Then, the coexistence of several charge states in the plasma

plume makes it possible a greater depth of implantation with respect to traditional ion implanters, at the same accelerating potential. In fact, ions with charge state  $+z$  will acquire a kinetic energy  $z$  times higher than  $+1$  ions in the acceleration stage. On the other side, such a “non-monoenergetic” ion beam, with a discrete energy spectrum, allows to implant ions into different depths of the substrate simultaneously, without changing the accelerating potential. This offers the possibility to achieve some spatial periodicity in the implant profile in a very simple way.

Another important aspect is the possibility to implant ions and/or deposit thin films. Thin film quality can be greatly improved because LIS implantation has the intrinsic advantage of ion beam assisted deposition (IBAD). Moreover, many characteristics and advantages of LIS implantation are common to PLD:

- direct plasma generation from any solid material, even refractory and compound;
- implantation “congruent” to the target stoichiometry;
- easiness and readiness of the process, with low operation costs;
- versatility of the technique, for example in the change of the ion species to be implanted, achievable by using multiple targets or simply mounting different materials on the same target and controlling the target rotation speed;
- treatment of relatively wide surfaces with high dose rate and low implantation energy;
- very low environmental impact, since the use of toxic gaseous precursors (*e.g.*, silane for Si ions or diborane for B ions) is not required, unlike PIII.

Furthermore, the following considerations should be stressed here:

- i. Co-implantation of several kinds of ions (especially metal ions) into a workpiece would be very challenging for traditional ion implantation techniques.
- ii. One intrinsic disadvantage of PIII is the non-uniform energy distribution which makes it difficult to control the implantation profile because of the finite rise time of the bias voltage pulse. In LIS implantation the bias voltage is at a steady state before the laser pulse is applied (in DC mode) or before the gross of the plasma plume reaches the extraction gap (in AC mode), thereby yielding a more uniform ion energy distribution.

- iii. In this sense, LIS implantation presents the advantage of traditional line-of-sight ion implantation which uses an ion accelerator.
- iv. Although LIS can be implemented on an ion gun as well, instead of the conventional ion sources, the technique studied in this work focuses on a compact device in which the implantation stage is integrated at the level of the ion source itself, without the presence of a beamline.

Nevertheless, LIS implantation presents also the following important shortcomings, which can become limitative in certain applications:

- low accuracy in the implantation profile;
- relatively low implantation energy, and so small implantation range (at least in the minimal set-up, in which a distributed-gradient accelerating field is not used);
- the deposition of the plume neutral component, that in some cases can be unwanted.

Conventional beamline implantation remains the unique technique able to overcome all the above mentioned problems, although with a great technological cost. Of course, for high precision applications it is unreplaceable.

## **1.5 Potential applications**

In the experimental set-up investigated in the present work (minimal configuration), LIS implantation is the ideal process for applications which do not need monoenergetic beams and/or high implantation energy (higher than one hundred keV). Really, the abundance of the ion charge states present in the plasma plume and the shape of the energy spectrum of the accelerated ions are correlated, as better explained in the next chapters. Of course, the lower the maximum charge state is, the lower the spectrum endpoint is. Disregarding the plume neutral component (sub-keV particles), monoenergetic implanting beams can be achieved by producing plasma in which the presence of ion charge states higher than +1 is negligible. It can be performed by suitably choosing the laser irradiance on the target, although at the expense of the ion flux.

Some fields of application are summarized below:

- modification of the surface properties of materials, in order to increase their hardness and resistance to wear, oxidation, corrosion (for example, doses of the order of  $10^{17}$  ions/cm<sup>2</sup> are typically required for metals);
- improvement of the surface mechanical resistance and modification of the properties of fusion, solubility and surface tension for polymeric materials (for example, by dehydrogenation, with doses of the order of  $10^{15}$  ions/cm<sup>2</sup>);
- development of innovative materials with special chemical, electrical and optical properties;
- protective coatings with refractory materials (TiN, CrN or other nitrides).

In thin film deposition and IBA applications, LIS implantation can form an atomically intermixed layer between the substrate and film, improving adhesion. For example, making alloy coatings could be simplified via LIS implantation, by mounting the desired film materials on the same target.

LIS implantation could be favourably used to prepare hard, amorphous, hydrogenated diamond-like-carbon (DLC) films, which are characterized by high hardness, chemical inertness, optical transparency, and high electrical resistivity [39]. DLC films can be used in many areas, which include hard transparent optical coatings and protective wear-resistant coatings [40-42]. Currently DLC films are prepared either from glow discharge techniques using hydrocarbon gas, or from solid sources (vacuum plasma arc, ion beam sputtering) [40]. LIS implantation, which combines the advantage of ion beam assisted deposition and ion beam mixing (C and H ions), is ideally suited to produce DLC films, by exploiting, for example, the ablation of polymers.

By rastering the substrate and the target and using multiple laser beams, the applications of the LIS implantation could be no longer limited by the small size of the deposition or implantation area, and by non-uniformity of the film thickness.

## 2. THEORY

### 2.1 Phenomenology of the plasma plume

A phenomenological picture of the ion and neutral components of the plasma plume is described in the present Section, with emphasis on aspects relevant for ion diagnostics and extraction, such as presence of various ion charge states; particle density; angular distribution and forward peaking; ion current and ion fluence.

Usually the so-called “shifted” Maxwell-Boltzmann distribution is assumed for the velocity of ions and neutrals in the free expanding plume [1-3]:

$$f(v_x, v_y, v_z; v_d, T) = A \exp\left\{-\beta\left[(v_z - v_d)^2 + v_x^2 + v_y^2\right]\right\} \quad (2.1)$$

with

$$A \equiv \left(\frac{M}{2\pi kT}\right)^{\frac{3}{2}} \quad (2.2)$$

$$\beta \equiv \frac{M}{2kT} \quad (2.3)$$

where Cartesian coordinates  $(x, y, z)$  are used, taking the  $z$  direction perpendicular to the target surface;  $f(v_x, v_y, v_z)dv_x dv_y dv_z$  is the number of particles having velocity values within  $(v_x, v_x + dv_x)$ ,  $(v_y, v_y + dv_y)$ ,  $(v_z, v_z + dv_z)$ ;  $v_d$  is the plume drift velocity;  $T$  is the ion temperature;  $M$  is the ion mass; and  $k$  is the Boltzmann constant. Figure 2.1 shows a schematic drawing of the plume expansion and ion extraction.

Generally values of the order of  $10^4$  m/s and  $10^5$  K are found for  $v_d$  and  $T$ , respectively, for laser power densities in the range 0.1 - 10 GW/cm<sup>2</sup> and laser pulse duration of the order of 10 ns. Nevertheless, in the literature there is an increasing evidence that the neutrals and the various ion groups with different charge state contained in the laser plasma exhibit different energy spectra, each according to a shifted Maxwell-Boltzmann distribution with its own values for drift velocity and temperature [1-5]. However, there are theoretical reasons and experimental results which indicate that the temperature is roughly the same for all the ion groups. On the

contrary, the drift velocity, meant as the center-of-mass velocity of an ion group, is strongly dependent on the charge state. In fact, apart from hydrodynamic effects acting on neutral atoms as well (*e.g.*, Knudsen-layer formation), it is determined by the existence of a high electric field inside the plasma itself, which accelerates the ions just in the first stage of the plume expansion. This explains the observed increase of the drift velocity with the charge state.

In what follows, it will be considered an outline in which the neutrals and the various ion groups have thermalized to the same temperature and have different drift velocities. Many experimental findings confirm this picture for laser power densities in the range 0.1 - 10 GW/cm<sup>2</sup> and laser pulse duration of the order of 10 ns. Thus, the  $j$ -th ion group will have got a shifted Maxwell-Boltzmann distribution  $f_j(\mathbf{v}; v_{d,j}, T)$  and a number of particles  $C_j$ . The notation  $j = 0$  will be adopted for the neutral atoms.

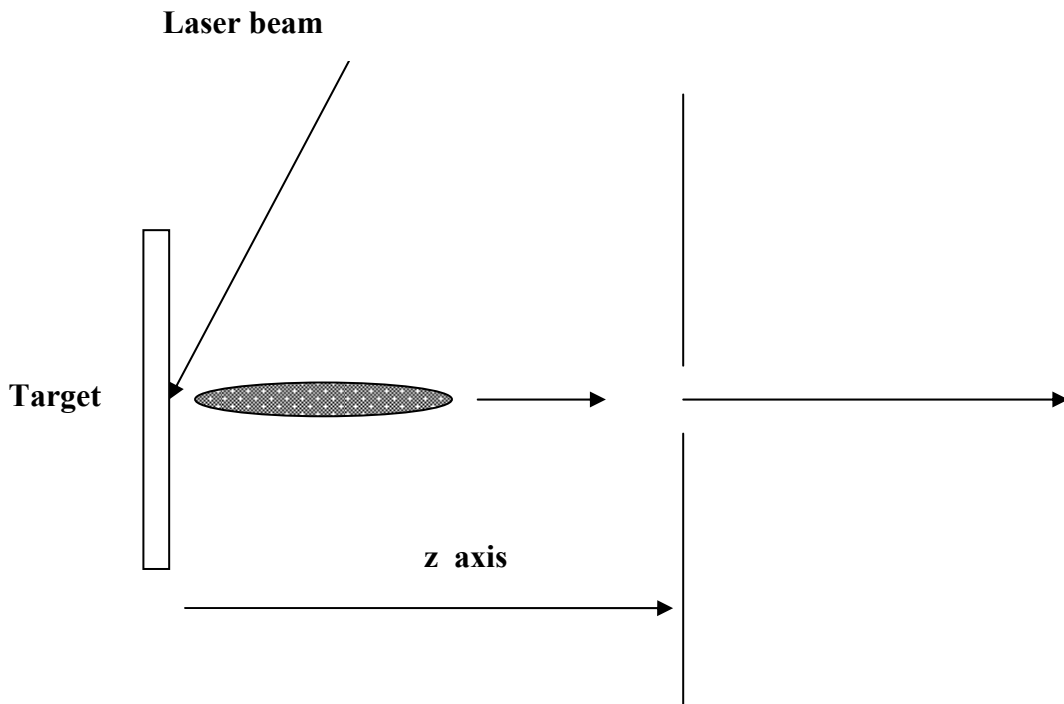


**Fig. 2.1.** Schematic drawing of the plume expansion and ion extraction.

Assuming a free expansion from a point-like source, readjusting and generalizing the results of Utterback *et al.* [43], the following expression can be derived for the

number of particles per unit volume,  $\eta_j(\mathbf{r}, t)$ , at the point  $\mathbf{r}$  and time  $t$  from the laser pulse:

$$\eta_j(z, r, t) = AC_j t^{-3} \exp\left[-\beta\left(\frac{r}{t}\right)^2\right] \cdot \exp\left[-\beta\left(\frac{z}{t} - v_{d,j}\right)^2\right] \quad (2.4)$$

where cylindrical coordinates  $\mathbf{r} = (z, r, \varphi)$  have been introduced due to the symmetry of the plume with respect to the  $z$  axis. The overall particle density,  $\eta(z, r, t)$ , is obtained by the following straightforward superimposition:

$$\eta(z, r, t) = \sum_{j=0} \eta_j(z, r, t) \quad (2.5)$$

The “partial” particle current density,  $\mathbf{J}_j(\mathbf{r}, t)$ , *i.e.*, the number of particles per unit time per unit area, is given by

$$\mathbf{J}_j(\mathbf{r}, t) = \eta_j(\mathbf{r}, t) \mathbf{v} \quad (2.6)$$

where

$$\mathbf{v} = \mathbf{r}/t \quad (2.7)$$

due to the self-similar plume expansion. A relation analogous to Eq. (2.5) holds for the overall particle current density,  $\mathbf{J}(\mathbf{r}, t)$ .

The  $j$ -th component of the particle current,  $i_j(t)$ , through a surface  $S$ , can be calculated by the general equation for a radial expansion:

$$i_j(t) = \int_S \mathbf{J}_j(\mathbf{r}, t) \hat{\mathbf{r}} \cdot \hat{\mathbf{n}} dS \quad (2.8)$$

where  $\hat{\mathbf{r}}$  and  $\hat{\mathbf{n}}$  are the position and surface versors, respectively. For a plane circular surface with radius  $R$ , placed at a distance  $L$  from the target and centred on the  $z$  axis (see Fig. 2.1), such as the extraction hole or the collector of a Faraday cup used for diagnostics, the integral in Eq. (2.8) becomes:

$$i_j(t) = 2\pi AC_j Lt^{-4} \exp\left[-\beta\left(\frac{L}{t} - v_{d,j}\right)^2\right] \cdot \int_0^R \exp\left[-\beta\left(\frac{r}{t}\right)^2\right] r dr \quad (2.9)$$

After some calculations, it is found that

$$i_j(t) = AC_j Lt^{-2} \exp\left[-\beta\left(\frac{L}{t} - v_{d,j}\right)^2\right] \cdot g\left(\frac{R}{t}\right) \quad (2.10)$$

where

$$g(R/t) \equiv \pi\beta^{-1} \{1 - \exp[-\beta(R/t)^2]\} \quad (2.11)$$

Note that, under the condition

$$\frac{1}{2}\beta\left(\frac{R}{t}\right)^2 \ll 1 \quad (2.12)$$

fulfilled, for example, for a small solid angle of collection, it is possible to neglect  $o[\beta(R/t)^2]$  in the series expansion of the exponential term in Eq. (2.11), obtaining  $g(t) \approx \pi R^2 t^{-2}$  (independent on  $T$ ), and Eq. (2.10) reduces to an expression more manageable for data analysis and calculations:

$$i_j(t) \approx C_j Lt^{-4} \exp\left[-\beta\left(\frac{L}{t} - v_{d,j}\right)^2\right] \quad (2.13)$$

The overall ion current,  $I(t)$ , like that recordable by a Faraday cup, can be written as

$$I(t) = e \sum_j j i_j(t) \quad (2.14)$$

where  $e$  is the electron charge.

The number of particles of the  $j$ -th group,  $N_j$ , which can be collected, revealed, deposited or extracted through the circular surface  $S$ , is given by the obvious relation:

$$N_j = \int_0^\infty i_j(t) dt \quad (2.15)$$

The integration is rather laborious and results in the complicated expression

$$N_j(\Theta; \mu_j) = \frac{C_j}{2} \left\{ 1 + \operatorname{erf}(\mu_j) - \cos \Theta \exp(-\mu_j^2 \sin^2 \Theta) [1 + \operatorname{erf}(\mu_j \cos \Theta)] \right\} \quad (2.16)$$

where  $\operatorname{erf}(\xi)$  is the standard error function,

$$\operatorname{erf}(\xi) = \frac{2}{\sqrt{\pi}} \int_0^\xi \exp(-\chi^2) d\chi \quad (2.17)$$

and the angular variable  $\Theta$  and the parameter  $\mu_j$  have been introduced, as defined respectively by the following relations:

$$\tan \Theta = \frac{R}{L} \quad (2.18)$$

$$\mu_j = v_{d,j} \sqrt{\beta} \quad (2.19)$$

Then, the mean fluence,  $F_j$ , of particles of the  $j$ -th group passing through the circular surface  $S$  can be calculated as

$$F_j(\Theta; \mu_j) = \frac{N_j(\Theta; \mu_j)}{\pi R^2} \quad (2.20)$$

It is simple to see that the quantity  $\mu_j^2$  is proportional to the ratio between the translational kinetic energy of the  $j$ -th group,  $\frac{1}{2} C_j M v_{d,j}^2$ , and its internal kinetic energy,  $\frac{3}{2} C_j kT$ . Thus, as it is intuitive, the parameter  $\mu_j$  expresses how much the expansion of a group of particles is forward peaked along the direction of motion of its

centre of mass ( $z$  axis). Usually  $0 < \mu_j < 10$  is found or expected for laser power densities in the range 0.1 - 10 GW/cm<sup>2</sup> and laser pulse duration of the order of 10 ns.

It is also found that higher charge state ion groups have higher  $v_d$  values, and so, higher  $\mu$  values. Accordingly, they exhibit more forward peaked angular distributions and their particles are concentrated at smaller polar angles with respect to the  $z$  axis.

Such considerations are particularly important in ion diagnostics or extraction, since the relative abundance of the various ion species in the diagnosed or extracted bunch depends on the amplitude of the sampling or extraction solid angle. This, in turn, determines the energy spectrum of the ions accelerated after the extraction, since the  $N_j$  ions with charge state  $+j$  acquire a kinetic energy,  $E_j$ , given by

$$E_j = jeV_a \quad (2.21)$$

under the accelerating potential  $V_a$ . Furthermore, an important LIS figure of merit such as the extraction (or implantation) efficiency,  $\varepsilon$ , also depends on the amplitude of the extraction angle. It is defined as the ratio between the number of  $+j$  ions extracted and the overall number of  $+j$  ions produced, and can be estimated as

$$\varepsilon_j(\Theta) = \frac{N_j(\Theta)}{C_j} \quad (2.22)$$

apart from space charge effects which can limit the actual yield of extracted ions with respect to the  $N_j$  value.

Useful approximations of Eq. (2.16) can be deduced in the two cases  $\mu_j \ll 1$  (quasi-spherical expansion) and  $\mu_j \gg 1$  (strong forward peaking):

$$N_j(\Theta) = a_\mu \frac{C_j}{2} [1 - \cos \Theta \exp(-\mu_j^2 \sin^2 \Theta)] \quad (2.23)$$

where

$$a_\mu = \begin{cases} 1/2 & \text{for } \mu \ll 1 \\ 1 & \text{for } \mu \gg 1 \end{cases}$$

It should be underlined that Eq. (2.16) and its approximated form, Eq. (2.23), result in the usual scaling law  $N_j \approx L^{-2}$  for enough large values of  $L$  ( $L \rightarrow \infty$ ), *i.e.*, small angles ( $\Theta \rightarrow 0$ ).

A convenient approximated expression can be carried out at small angles instead of Eq. (2.16), if the well-known law [44]

$$h(\theta) \approx A \cos^p \theta \quad (2.24)$$

is used for the plume angular distribution,  $h(\theta)$ . In Eq. (2.24),  $h$  is the number of ejected particles per solid angle unit,  $\theta$  is the polar angular coordinate with respect to the  $z$  axis,  $A$  is the amplitude, and  $p$  is an empirical parameter expressing the plume forward peaking ( $p \geq 0$ ). Assuming that each particle group has an angular distribution of the form of Eq. (2.24),  $h_j(\theta)$ , with its own parameters  $A_j$  and  $p_j$ , the following obvious relation holds for  $N_j$ :

$$N_j(\Theta) = 2\pi \int_0^\Theta h_j(\theta) \sin \theta \, d\theta \quad (2.25)$$

The integration is straightforward and gives the following expression for  $N_j(\Theta)$ :

$$N_j(\Theta) = N_{0,j} \cdot \left(1 - \cos^{p_j+1} \Theta\right) \quad (2.26)$$

or, in terms of  $L$ :

$$N_j(L) = N_{0,j} \cdot \left\{ 1 - \left[ 1 + \left( \frac{R}{L} \right)^2 \right]^{-\frac{1}{2}(p_j+1)} \right\} \quad (2.27)$$

where

$$N_{0,j} \equiv \frac{2\pi A}{p_j + 1} \quad (2.28)$$

Note that  $N_{0,j}$  has the same physical meaning than  $C_j$ .

## 2.2 Ion-substrate interaction: basic concepts and considerations

Upon entering the substrate, the accelerated ion undergoes a series of collisions with the bulk atoms, reducing progressively its energy up to a complete stopping. The ion slowing down is due to two main electromagnetic interaction processes: nuclear and electronic stopping.

Nuclear stopping is due to the energy transfer from the incident ion to the substrate nuclei. Such a kind of elastic scattering is significant for slow ions and the amount of energy transferred through this mechanism is enhanced when the masses of the ion and target atom are nearly the same. A deflection of the particle from its incident direction occurs, at an extent depending on the transferred energy and the ratio between the projectile and target masses. The interaction may be strong enough to displace the bulk atom from its site; for example, only 15 eV need to displace one Si atom. The displaced atom may even have enough kinetic energy to displace several other lattice atoms. Nuclear stopping is the main cause of crystal damage.

Electronic stopping is due to the energy transfer from the ion to the electrons of the host material, causing atom excitation (“soft” collisions) or ionization (“hard” collisions). The amount of energy transferred in each collision is generally a very small fraction of the particle total kinetic energy; however, in normally dense matter, the number of collisions per unit path length is so large that a substantial cumulative energy loss is observed even in relatively thin layers of material. In fact, the interaction cross section is generally of the order of  $10^{-16} - 10^{-17} \text{ cm}^2$ . Such a kind of inelastic scattering is predominant for high energy ions (generally above 100 keV). Even in this case a deflection of the particle from its incident direction occurs, but at an extent generally much smaller in comparison with the nuclear Coulomb scattering. Electronic stopping is not directly responsible for crystal damage.

During its slowing down, the path followed by the incident ion can be described as a broken line in which each vertex represents an interaction point between the ion and a lattice atom. The projection of the final position of the ion on its incidence direction is usually called “projected range” and will be denoted hereafter by  $R$ .

Such a quantity is statistically distributed, due to the fact that the ion energy loss is not a continuous process, but a discrete-event process statistical in nature. In other words, an ensemble of identical particles will show a statistical distribution of values

of  $R$ , generating a wide profile, as a function of depth, for the number density inside the implanted sample. The mean value of the range distribution is usually referred as the “mean range” or simply the “range”. The standard deviation of the range distribution is known as “range straggling” or simply “straggling”, hereafter denoted by  $\sigma$ .

In a first approximation, the range distribution is gaussian in form. At a depth  $x$ , the number density (number of atoms per unit volume) of implanted ions,  $\rho(x)$ , can be therefore expressed by the following relation [45]:

$$\rho(x) = \frac{D}{\sqrt{2\pi} \sigma} \exp\left[-\frac{1}{2} \left(\frac{x-R}{\sigma}\right)^2\right] \quad (2.29)$$

where  $D$  is the dose of incident ions (number of ions per unit surface).

Different approaches exist for the determination of the values of  $R$  and  $\sigma$ . Calculations and experiments lead to many theoretical and semi-empirical formulas which cover many energy ranges and materials [46]. An alternative technique is the simulation of the transport of ions in matter by the Monte Carlo method. Such an approach has been followed in the present work.

From the point of view of applications, it should be pointed out that, denoting by  $E$  the initial energy of the incident ion, by  $M$  its mass and by  $M_a$  the mass of the target atom, the following simple scaling law roughly holds for  $R$  and  $\sigma$  at  $E$  values of the order of hundreds of keV or lower:

$$R, \sigma \propto E \frac{M_a}{M} \quad (2.30)$$

Some examples of  $R$  vs.  $E$  and  $\sigma$  vs.  $E$  curves in Si, obtained by simulation, are reported in Fig. 2.2. Implantation energies of the order of tens of keV (up to about 100 keV) were employed in the experiments reported in the present work.

The dependence of  $R$  and  $\sigma$  upon  $E$  is particularly important when implantation at different energies is carried out. In the present case an ion beam with several energy components was generated. A straightforward generalization of Eq. (2.29) gives the following relation for the cumulative ion density,  $\rho_t(x)$ , in such a kind of implantation:

$$\rho_i(x) = n \left[ \rho_0(x) + \sum_z \rho_z(x; F_z, R_z, \sigma_z) \right] \quad (2.31)$$

where  $n$  is the number of laser shots;  $\rho_0(x)$  is the density due to the implantation of the neutral particles; and  $\rho_z(x; F_z, R_z, \sigma_z)$  is the “partial” density due to the implantation of the  $+z$  charge state ions, depending on the parameters  $F_z$ ,  $R_z$  and  $\sigma_z$ . Ultimately,  $R_z$  and  $\sigma_z$  depend on the accelerating potential through  $z$ , see Eqs. (2.21) and (2.30).

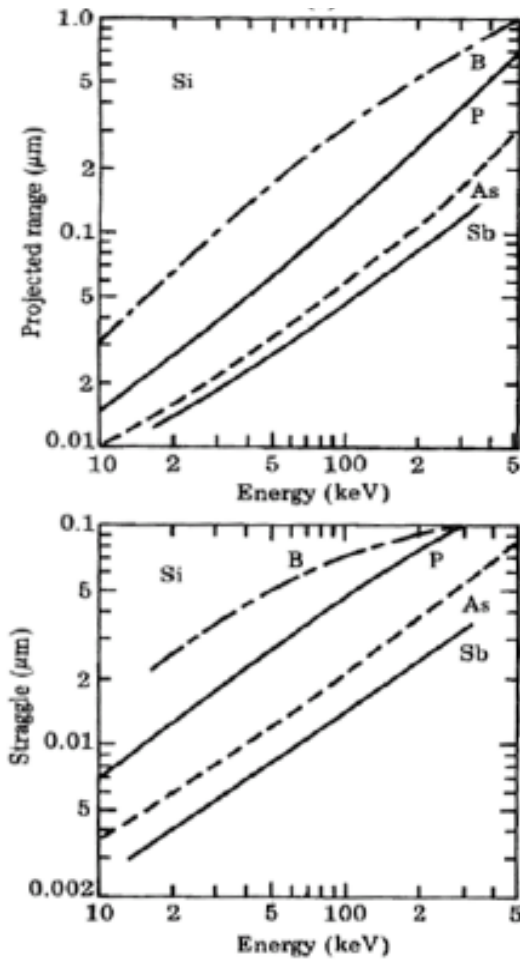


**Fig. 2.2.** Simulated curves showing the projected range,  $R$ , and the straggle,  $\sigma$ , in Si for various projectiles, as a function of their initial energy. Adapted from Gandhi et al. [47].

It is important to note that, in line of principle, one could modulate the depth profile by acting separately on the laser fluence on the target (and so on  $z$  and  $F_z$ ) and on the accelerating potential. Such an aspect is remarkable for practical applications of the LIS implantation. Nevertheless, careful diagnostics and calibration would need in order to find a relationship between the laser fluence and the ion charge state distribution.

### 2.3 Simulation of the ion implant

The well-known software SRIM-2003 [48] was employed to calculate the values of  $R$  and  $\sigma$  in amorphous Si for the various species and energies of implanted ions. Then, simulations of the concentration profiles  $\rho_i(x)$  also were carried out by means of SRIM. The results were compared with the depth profiles characterized experimentally. Details on the input parameters and approximations used for the simulations are given in Chapter 4.

SRIM is a group of programs which calculate the stopping and range of ions into matter, in the energy range 10 eV - 2 GeV/amu, using a full quantum mechanical treatment of ion - target atom collisions. The simulation of the transport of ions in matter is carried out by the Monte Carlo method.

During the collisions, the ion and atom have a screened Coulomb interaction, including exchange and correlation interactions between the overlapping electron shells. The ion has even long range interactions creating electron excitations and plasmons within the target. The calculations take into account the target collective electronic structure and the interatomic bond structure. The charge state of the ion within the target is described using the concept of effective charge, which includes a velocity dependent charge state and long range screening due to the collective electron sea of the target. A full description of the calculation can be found in Ziegler *et al.* [49].

## 3. EXPERIMENTAL

### 3.1 Experimental apparatus

The implantation system consisted of a KrF excimer laser (Lambda Physik, mod. COMPex) and a vacuum chamber made of stainless steel. The KrF laser provided a beam of 248 nm wavelength (5 eV photon energy) with a pulse duration (FWHM) of about 23 ns. In this experiment a pulse energy value reduced to 70 mJ was used. Figure 3.1 shows the implantation chamber.

The laser beam entered the implantation chamber through a thin quartz window. It was focused in a spot of about  $0.01 \text{ cm}^2$  on the surface of the target (T in Fig. 3.1), *i.e.*, the sample of the doping element to be implanted, by a 15 cm focal length lens. The angle between the normal to the target surface and the laser beam was  $70^\circ$ . In these conditions the average laser fluence value was about  $7 \text{ J/cm}^2$  per pulse, with a maximum value of  $20 \text{ J/cm}^2$  in the spot central region [50, 51]. Correspondingly, the beam average power density was estimated in  $3.5 \cdot 10^8 \text{ W/cm}^2$ .

The implantation chamber was fairly versatile and could be arranged in different configurations. It consisted of a plasma generation chamber (GC), 26.5 cm long, and a removable expansion chamber (EC), which allowed an initial free expansion of the plasma before the ion extraction [52]. The target support was a stem (2 cm in diameter) mounted on the GC by an insulating flange (IF) and kept to positive high voltage, in DC mode. The EC was connected mechanically and electrically to the target stem. A grounded electrode (GE) in front of the EC allowed to generate an intense electric field which was able to extract and to accelerate the ions. Such an arrangement presents the advantage to apply the HV directly to the target stem, keeping the GC and the vacuum system to ground. A set of four buffer capacitors, each of 1 nF, was connected between the target stem and the GE to stabilize the voltage during the extraction process. In such a way the capacitor stored charge was much higher than the extracted one, maintaining constant the accelerating voltage value.

The EC was an almost hermetic cylinder, 18.5 cm long, 9.0 cm in diameter, having the hole (1.0 cm in diameter) necessary for the ion extraction worked on its basis-electrode, see Fig. 3.2. On its lateral surface an optical hole was bored, as inlet port for the laser beam, and was closed by a thin quartz window. The distance between

the EC pierced electrode and the target was 16.8 cm. The GE was an aluminum pierced disc fixed at 1.3 cm from the perforated EC electrode.

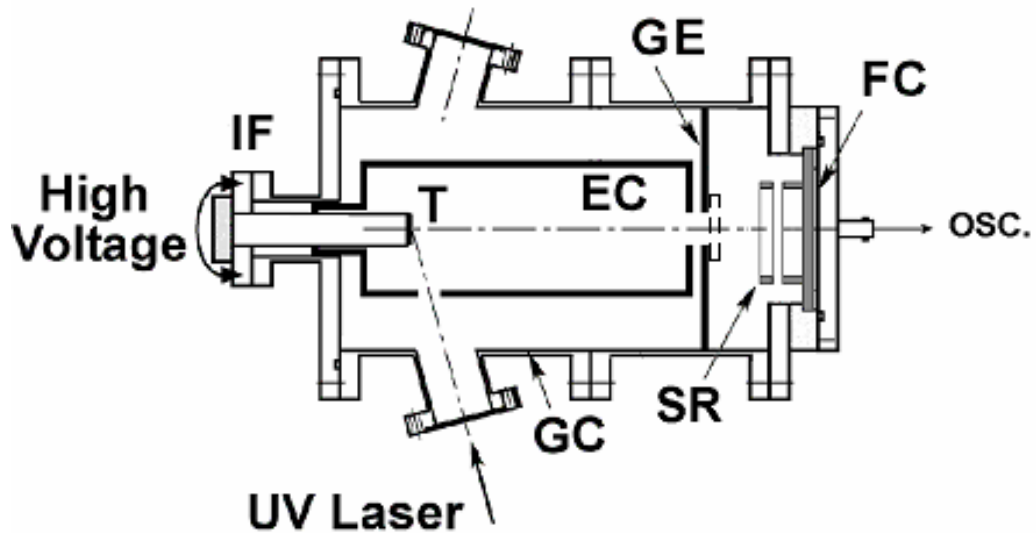


**Fig. 3.1.** Experimental apparatus. GC: Generation Chamber; EC: Expansion Chamber; T: Target; IF: Insulating Flange; GE: Grounded Electrode; FC: Faraday Cup; SR: Suppression Ring; osc.: oscilloscope. The substrate to be implanted is behind the GE hole (dashed contour).

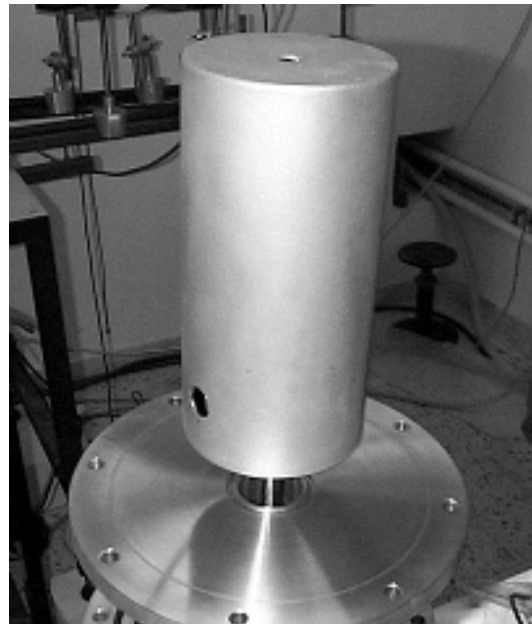


**Fig. 3.2.** A photograph of the expansion chamber. Note the target stem on which it is mounted and the flange of the GC. The inlet port for the laser beam, bored on its lateral surface, and the extraction hole, worked on a basis, are also shown.

In such a configuration, when the EC was biased at +HV, plasma electrons were expelled by the intense electric field as the plasma in the plume approached the EC hole [53]. The expelled electrons left behind a shallow ion sheath near the EC hole. Beyond the sheath the plasma was neutral.

In order to get implantation, Si(100) or Si(111) wafers (n type) were placed just on the GE hole (1.0 cm in diameter), outside the acceleration gap. The implantation zone area was 0.78 cm<sup>2</sup>.

Many attempts were done in order to accelerate ions without the EC, but arcs were present [54]. As a consequence, the extraction voltage value decreased, provoking a power supply extra-current. The presence of the EC eliminated arcs for accelerating voltages up to 50 kV. In fact, by means of such an expedient, the plasma density at the extraction point decreased to a value such that the occurrence of arcs was avoided for the typical values of laser irradiance (0.1 - 10 GW/cm<sup>2</sup>), laser repetition rate (~ 1 Hz) and extraction voltage (tens kV) used in these experiments.

However, the use of the HV AC mode becomes indispensable, if one wants to retain the simple extraction-implantation configuration here employed, when higher accelerating voltage values (quite a lot of tens kV) and/or higher ion flux values are required. In such a case, the gap bias voltage has to be delayed for several microseconds with respect to the laser pulse [13] and/or the bias pulse duration has to be suitably reduced with respect to the plasma bunch one. In extreme conditions, a single or repeated HV fast pulses, with duration of tens or hundreds ns, could be necessary. For this purpose, a novel pulser, based on the utilisation of transmission lines, was developed in a parallel research activity [55, 56] during this thesis work. It might be easily applied to the present experimental set-up to polarize the extraction gap. Further details are reported in Chapter 5.

The EC sizes realized a good compromise between the suitable plasma dilution and the reduction of the extracted ion flux due to the decrease of ion density with the distance from the target [57, 58]. The extraction gap had an acceptance solid angle of about  $3 \cdot 10^{-3}$  sr with respect to the plasma point-source on the target. Despite this low geometrical acceptance, a considerable fraction of the overall ion yield was extracted thanks to the strong forward peaking of the plasma plume [59].

Three kinds of implant were carried out. Si substrates were implanted one at a time with Al, Cu and Ge, separately. Al, Cu and Ge were chosen not for particular

practical applications of their implants in Si, but simply because their ablation plasma had been very well characterized in previous experiments at the Laboratory of Applied Electronics of Lecce. Therefore, these elements could be immediately employed to test the feasibility of the LIS implantation. On the other side, Si is the most obvious choice for a substrate to be implanted. Moreover, it should be pointed out that the majority of the analytical techniques are, by custom, already well calibrated and ready to use for analyses on Si substrates.

99.99% pure samples were used as laser targets, in the form of little thin discs. The laser shots on the reservoir material were 400 for Al, 200 for Cu and 500 for Ge implantation. The laser was operated at 1 Hz repetition rate. The accelerating voltage was fixed at 40 kV, the maximum value allowed by arcing. The vacuum chamber was evacuated by a turbo-molecular pump down to  $10^{-6}$  mbar (base vacuum).

### 3.2 Ion beam diagnostics

Before the implantation process, a measurement of the extracted ion current by means of a Faraday cup (FC) was performed to estimate the number of implanting ions per unit surface produced per laser pulse (ion fluence), see Fig. 3.1. The FC, 8 cm in diameter, was placed beyond the acceleration gap, at a distance of 2.5 cm, and was equipped with a suppression ring (SR) in order to avoid the current due to secondary electron emission from the collector [60].

A slight negative bias voltage,  $V_c$ , was applied to the FC, see Fig. 3.3. A 5  $\mu$ F capacitor was used to decouple the measuring circuit from the bias voltage. The FC signal was closed on a 50  $\Omega$  load resistor via a transmission line. The suppression of the secondary electron current was achieved by charging the SR to a suitable polarization potential lower than the FC one. By such a configuration the FC waveform represented the real-time evolution of the extracted ion pulse.

Fixing  $V_c = -50$  V, the FC output current decreased progressively when the SR polarization voltage,  $V_s$ , was varied from 0 to about  $-200$  V. No further variation was observed for  $V_s < -200$  V. At  $V_s = -200$  V the peak current decreased by a factor of 30% in comparison with the case of null bias ( $V_s = 0$ ). The bias  $V_s = -200$  V was chosen as the working value.

The various ion charge states present in the free expanding plasma bunch and their relative abundance were assessed by means of two different mass-to-charge spectrometers: a potential barrier filter (PBF) [61] and a cylindrical ion energy analyzer (IEA) [60, 62].

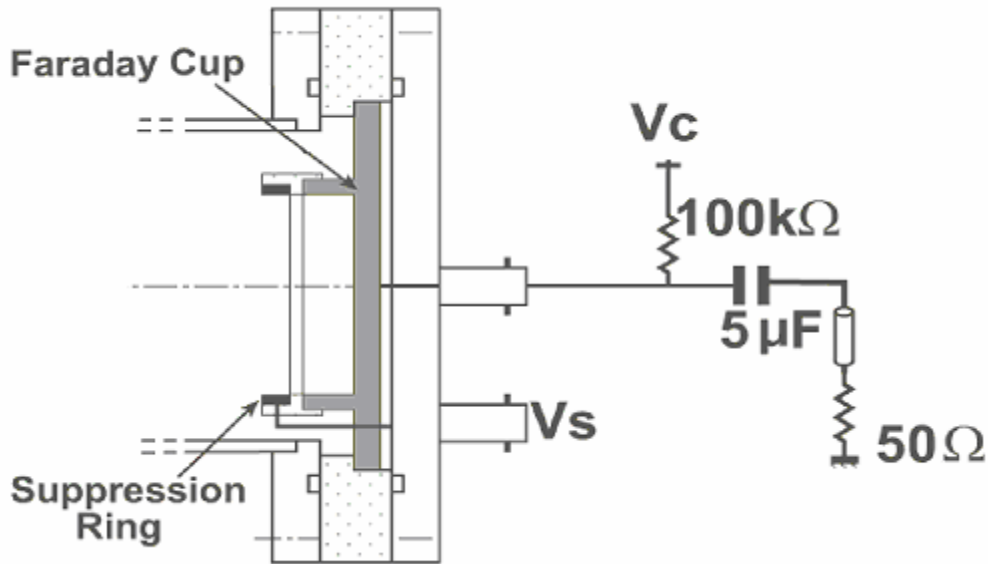


**Fig. 3.3.** Detail of the Faraday cup.  $V_c$ : Faraday cup polarization voltage;  $V_s$ : suppression ring polarization voltage.

As regards the potential barrier spectrometer, it allowed to recover the ion energy distribution for each charge state present in the plasma plume. This was obtained substantially by selecting the particles by a stopping potential, step-by-step variable, and analyzing the resulting “filtered” time-of-flight (TOF) spectra, recorded by a Faraday cup. Nevertheless, it should be pointed out that, for the present study, the main interest was not just about the shape and range of the energy spectra, but rather about the ratio between their integrals, expressing the relative abundance of the various ion charge states in the solid angle of sampling.

An electrostatic barrier made of three meshes, 1 cm apart from each other, was inserted in front of the FC (see Fig. 3.4) and placed inside a short drift tube connected to the GC as shown in Fig. 3.5. The PBF position was such that it diagnosed all the

ions in the same solid angle subtended by the implantation area with respect to the centre of the target. No difference of potential was applied to the acceleration gap during this measurement.

The central mesh of the barrier was biased to different positive voltages,  $V_b$ , while the two external ones were connected to ground, so that the stopping potential was present only in a short gap with respect to the total drift length and shielded outside. The modification of the TOF of the ions able to cross the electrostatic barrier was therefore negligible. Ions with charge  $z$  could cross the potential barrier only if they had kinetic energy,  $E$ , higher than  $zeV_b$ , being  $e$  the electron charge. On the contrary, ions with energy  $E < zeV_b$  were blocked. An amount of energy equal to  $zeV_b$  was subtracted to ions with energy  $E > zeV_b$  in the path between the first and the second mesh, and it was re-gained in the gap between the second and the third mesh.

As an example, the effect of the stopping potential on the plasma TOF signal is shown in Fig. 3.6. The 0 V-signal refers to the not perturbed plasma plume. Two series of abrupt drops are evident for each positive barrier voltage value; for each spectrum, one shoulder is located near the leading edge (marked by a black dot), while a knee occurs at higher TOF values. This behavior can be ascribed to the predominant concentration of +1 and +2 ions in the plasma bunch. In fact, it is easy to show that, at a given  $V_b$ , the two cutoff TOF values,  $t_c$ , satisfy the following relation:

$$t_c = \frac{d}{v_c} \quad (3.1)$$

where  $d$  is the target-FC distance and  $v_c$ , the  $z$ -dependent threshold velocity, is given by the following equation:

$$v_c = \sqrt{\frac{2zeV_b}{M}} \quad (3.2)$$

where  $M$  is the ion mass.

The full procedure to deconvolute the energy spectrum of each ion component with charge state  $z$  from the overall TOF spectrum is fully described in Ref. 61 and will not be reported here.

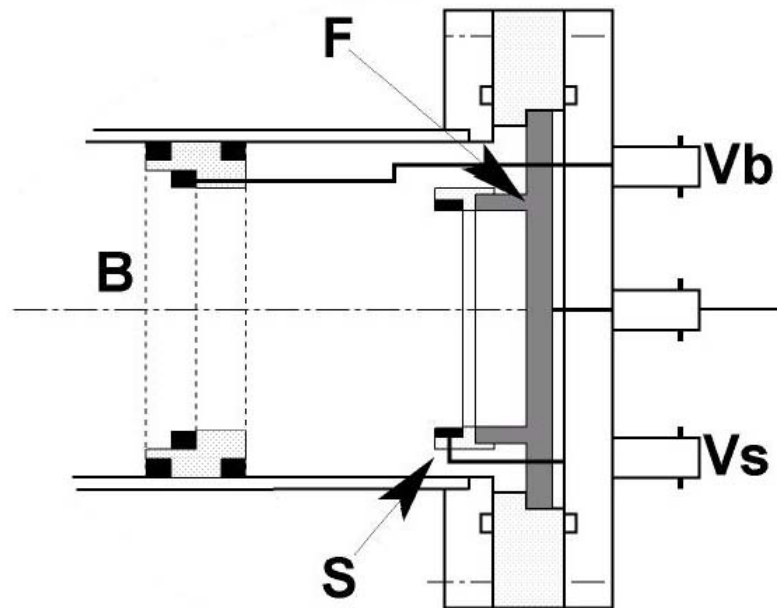


**Fig. 3.4.** Detail of the potential barrier (B) spectrometer. *F*: Faraday cup; *S*: suppression ring;  $V_s$ : suppression ring polarization voltage;  $V_b$ : polarization voltage of the central grid of the barrier. The external grids are grounded. The bias-readout circuit of the Faraday cup, here not shown, is like in Fig. 3.3.

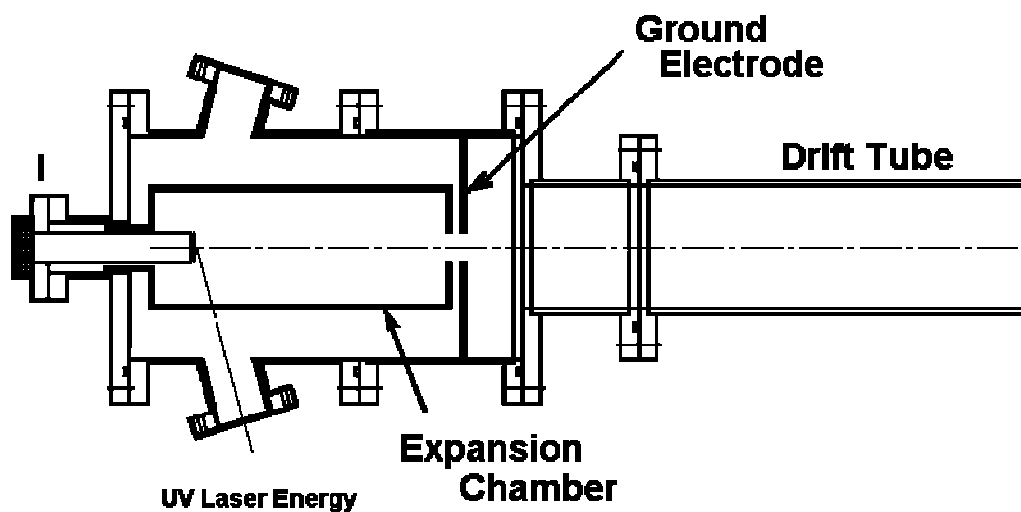


**Fig. 3.5.** The experimental chamber equipped with a drift tube utilised for mounting PBF and IEA spectrometers.

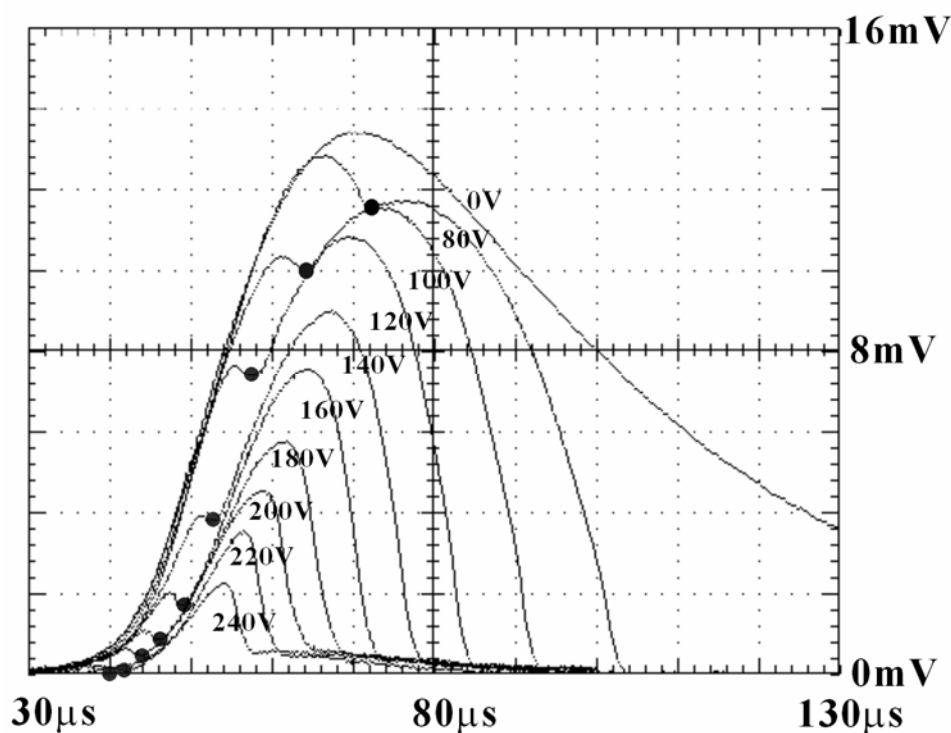


**Fig. 3.6.** Typical ion TOF spectra under the action of the PBF. The dots on the traces mark the TOF values corresponding to cutting off +2 ions with energy lower than  $2eV_b$ . The knees at the bottom are due to cutting off +1 ions with energy lower than  $eV_b$ .

As regards the IEA, it is more sensitive than the potential barrier spectrometer and allows to detect the presence of higher charge states with very low abundance (even in trace). The device is shown in Fig. 3.7. It was connected to the GC through a drift tube, mounted as shown in Fig. 3.5. No difference of potential was applied to the acceleration gap during the IEA measurements.

The IEA consists of two charged baffle-plates, with bend radii  $R_1$  and  $R_2$ , and a windowless electron multiplier (WEM) for the signal amplification. The voltages of the two baffle-plates,  $V_1$  and  $V_2$ , are equal and opposite,  $V_1 = -V_0$  and  $V_2 = V_0 > 0$ , and  $V_0$  is changed to obtain a selection of the ion energy-to-charge ratio. In fact, depending on the value of  $V_0$ , only ions with a certain  $E/z$  ratio are able to pass the IEA filter, following the bent trajectory sketched in Fig. 3.7. The following equation [60] holds for  $E/z$ :

$$E/z = 2\gamma eV_0 \quad (3.3)$$

where  $\gamma$  is a constant depending on the system geometry:

$$\gamma \cong \frac{1}{2\ln(R_2/R_1)} \quad (3.4)$$

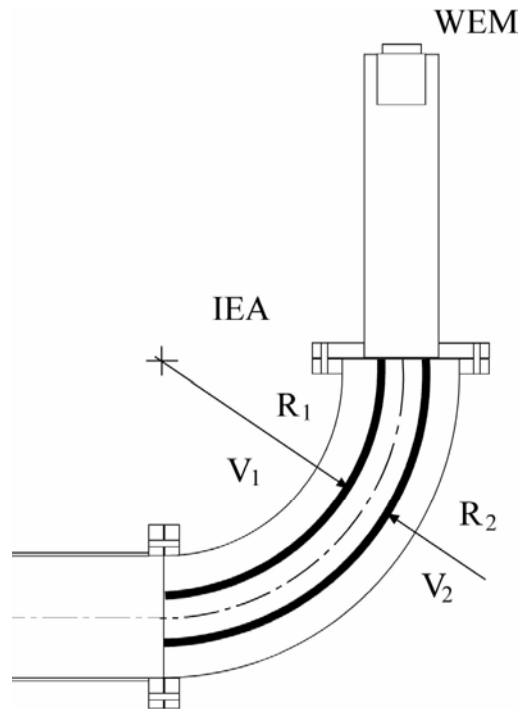


**Fig. 3.7.** Sketch of the ion energy analyzer (IEA).  $R_1$  and  $R_2$ : electrode radii;  $V_1$  and  $V_2$ : electrode voltages; WEM: windowless electron multiplier.

Therefore, the TOF values of the particles reaching the WEM is given by the following equation:

$$TOF = L \sqrt{\frac{m/z}{4\gamma eV_0}} \quad (3.5)$$

where  $L$  is the distance between the target and the WEM. By the TOF analysis according to Eq. (3.5), it was possible to recognize, on the oscilloscope trace, WEM signals corresponding to the detection of ions with different  $m/z$  ratios. The interested reader is addressed to Ref. 60 for further details on the IEA diagnostics.

For the discussion in Chapter 4 about the IEA measurements, it is important to point out here that the acceptance solid angle of this device was much smaller than the PBF one, due to the narrow IEA input slit (not shown in Fig. 3.7). Practically speaking, IEA analyzed only ions traveling along the axis of the implantation chamber.

### 3.3 Analysis of the implanted samples

The implanted samples were characterized by means of several analytical techniques: energy dispersive X-ray spectroscopy (EDX), Rutherford backscattering spectrometry (RBS), X-ray photo-electron spectrometry (XPS) and laser ablation – inductively coupled plasma – mass spectrometry (LA-ICP-MS). The analyses were commissioned to various national and foreign laboratories. Table 3.1 summarizes the situation of the various implanted samples and of the techniques used for their characterization.

*Table 3.1. Summary of the implanted samples and of the analytical techniques employed for their characterization.*

<b>Implanted element</b> <b>Substrate</b>	<b>Al</b>	<b>Cu</b>	<b>Ge</b>
<b>Si(111)</b>	SEM-EDX RBS XPS	XPS LA-ICP-MS	RBS LA-ICP-MS
<b>Si(100)</b>	SEM-EDX RBS LA-ICP-MS	LA-ICP-MS	LA-ICP-MS

EDX analysis was performed on the Al implanted samples by means of a scanning electron microscope (SEM-EDX), at the Department of Materials Science of the University of Lecce, Italy.

RBS analysis [63] was performed on two samples: an Al implanted sample, at CEDAD (Centro di Datazione e Diagnostica / Centre for Dating and Diagnostics), University of Lecce, Italy; and a Ge implanted sample, at the Swiss Federal Institute of Technology (ETH), Zurich, Switzerland. 2.0 MeV He ions were used as probe beam in both cases, accelerated by a tandem type Van de Graaff accelerator. Particles backscattered at an angle of  $170^\circ$  with respect to the incidence direction (normal to the sample surface) were revealed at CEDAD. In order to increase the sensitivity, a different experimental configuration was employed at ETH, operating at normal incidence and at a detection angle of  $115^\circ$  (“grazing exit”); see Fig. 3.8.

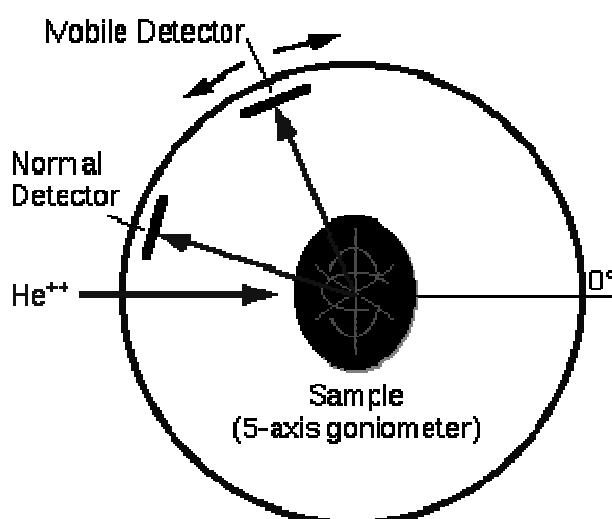


**Fig. 3.8.** Sketch of the experimental configuration used at ETH for RBS measurements. The position of the mobile detector was fixed at an angle of  $115^\circ$  with respect to the direction of incidence of the He ions probe beam.

XPS analysis [63] was carried out on Al and Cu implanted samples at the Advanced Materials Research Institute of the University of Northumbria, Newcastle, UK. A monochromatic Al  $K_\alpha$  (1486.6 eV) photon source was employed. 2p electrons were diagnosed for Si, Al and Cu. The measurements were performed in the “dynamic” mode to obtain a fine depth profile (3 nm resolution). An argon ion gun,

producing 4 keV Ar<sup>+</sup> ions, was used to sputter the sample. A careful measurement of the etching rate provided the calibration of the depth scale vs. the etching time.

LA-ICP-MS analysis was performed on Al, Cu or Ge implanted samples, in collaboration with the Swiss Federal Laboratories for Materials Research (EMPA), Duebendorf, Switzerland. Laser ablation combined to inductively coupled plasma - mass spectrometry is a relatively recent analytical technique with high elemental detection power but low depth resolution. Its utilisation in the present work was aimed by the attempt to test the performances of this technique in the sub-micron depth range. Furthermore, it should be not underestimated that the laser ablation facility used for the implantation might as well be implemented for on-site analytical characterization of the implanted samples.

The working principle of LA-ICP-MS consists in the following steps: laser irradiation of the sample; transport of the laser-induced aerosol by a flowing gas (Ar, He); ionization of the aerosol by an ICP plasma source; ion extraction from the plasma; and, finally, analysis by a mass spectrometer [64]. A brief description of the instrumentation used at EMPA follows; the system is fully described elsewhere [37]. A schematic drawing of a LA-ICP-MS apparatus is reported in Fig. 3.9.

A Nd:YAG laser microsampler (Quanta-Ray DCR-11, Spectra-Physics) was employed, suitably in-house modified. Frequency-quadrupled light (266 nm, Q-switched with 6 ns pulse duration) was pulsed at 10 Hz, and a fluence of 10 J/cm<sup>2</sup> for a 150 μm spot size was obtained using a 40 mm focal distance lens. The ablation cell was a 30 cm<sup>3</sup> cylindrical cell, provided with a 0.5 mm inlet nozzle to ensure a steady gas inlet. The transport tube was a 1.5 m long PVC tube, 4 mm in diameter. Argon was used as carrier gas at a flow of 0.9 l/min. The ICP-MS was a plasma quadrupole mass spectrometer (PE/Sciex Elan 6000) operated under standard conditions, *i.e.*, plasma gas 16 l/min, auxiliary gas 0.9 l/min, RF power 1300 W. Profilometry measurements were carried out to determine the ablated depth and to calibrate the time scale with the depth scale.

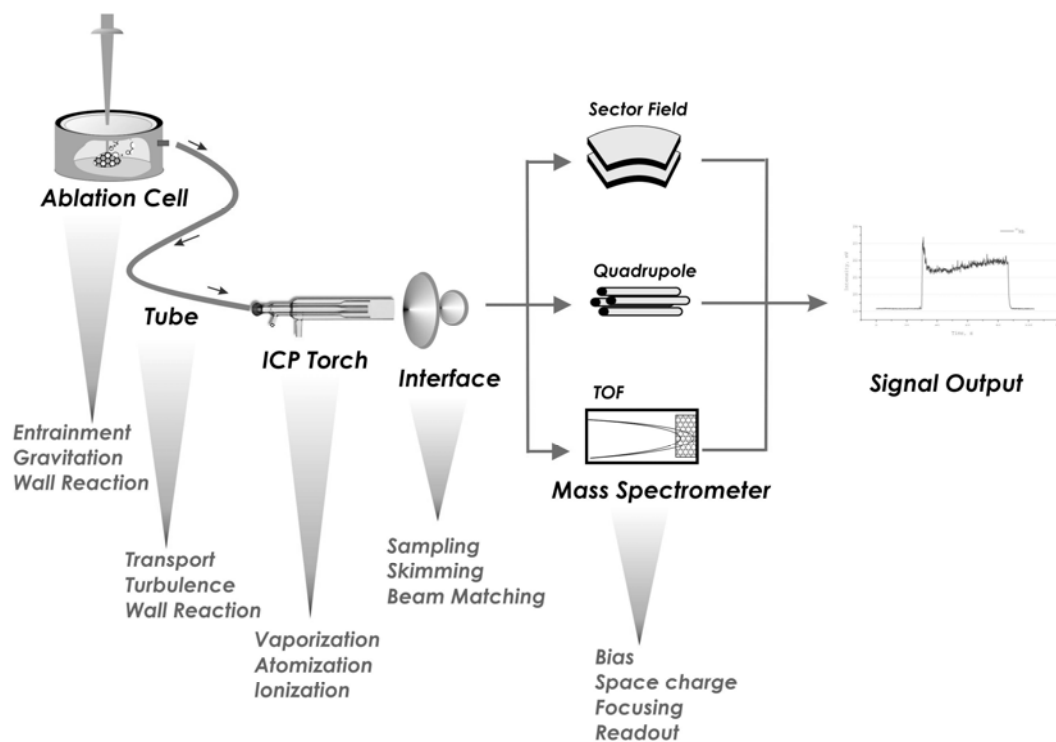


**Fig. 3.9.** Sketch of a LA-ICP-MS apparatus. The main mechanisms responsible for losses in the laser-induced aerosol and for signal dispersion are also indicated. The inlet nozzle of the carrier gas in the ablation cell is not shown. The system used at EMPA for the present measurements was equipped with a quadrupole mass spectrometer. Courtesy by D. Bleiner, University of Antwerp, Belgium.

## 4. RESULTS AND DISCUSSION ON ION DIAGNOSTICS AND IMPLANTATION

### 4.1 Ion charge state abundance

The coexistence in the plasma plume of ions with different charge states implies that the accelerated beam is composed of several energy components. According to Eq. (2.21), ions with charge state  $+z$  acquire a kinetic energy  $E_z = zeV_a$  after crossing the acceleration gap. It is therefore of basic importance to know in advance the abundance of the charge states in order to estimate the energy spectrum of the implanting ions [65, 66]. As mentioned in Section 3.2, the relative abundance of the various ion charge states present in the free expanding plasma bunch was assessed by means of two different mass-to-charge spectrometers: PBF, a potential barrier filter, and IEA, a cylindrical-plate electrostatic analyzer.

The result of the PBF deconvolution for the Cu laser plasma is reported in Fig. 4.1. Three charge states were identified. The bold curve corresponds to  $+1$  ions, the dotted one to  $+2$  ions, and the light one to  $+3$  ions. According to Eq. (2.14), the sum of these three signals resulted in the overall TOF voltage signal, here not shown, recorded by the FC when the PBF was not biased. The waveforms of the partial currents follow Eq. (2.10) and its approximation for axial currents, Eq. (2.13). The TOF values of these spectra indicate a kinetic energy of the order of hundreds eV, up to 700 – 800 eV.

The relative abundance (with respect to the number of particles),  $a_z$ , of the charge state  $+z$ , was calculated by the integrals of the deconvoluted TOF signals,  $V_z(t)$ , according to the following equations:

$$a_z = \frac{Q_z/z}{\sum_k Q_k/k} \quad (4.1)$$

where

$$Q_k \equiv \int V_k(t) dt \quad (4.2)$$

is a quantity proportional to the overall collected charge of  $+k$  ions.

For example, the following abundance values were found for Cu ions:  $a_1 = 0.75$ ;  $a_2 = 0.22$ ;  $a_3 = 0.03$ . Similar results were found for Al and Ge ions.

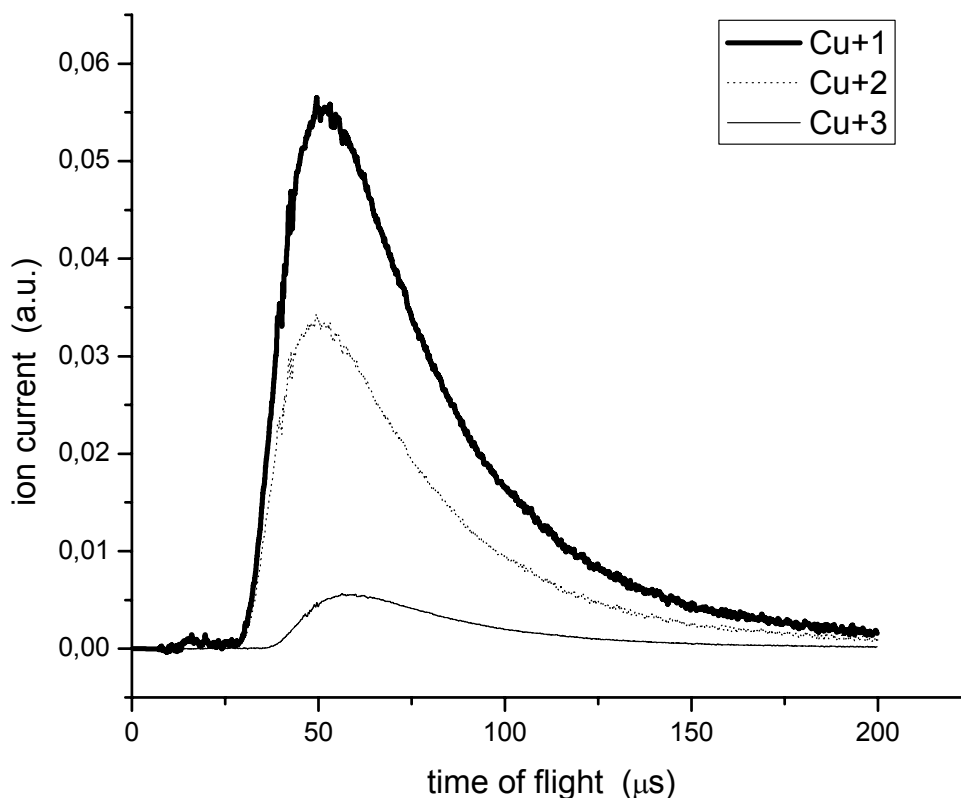


**Fig. 4.1.** PBF deconvolution of the ion current signal for Cu laser plasma. The sum of these three signals resulted in the overall TOF voltage signal recorded by the FC when the PBF was not biased.

The results of the IEA measurements on the Cu laser plasma are reported in Fig. 4.2. The presence of three charge states was confirmed and their energy spectra were directly measured. The higher sensitivity of the IEA allowed to reveal  $\text{Cu}^{+3}$  ions with energy up to about 1.1 keV. Although the energy of the ions generated by pulsed laser ablation was relevant in comparison with other processes for ion production, nevertheless it was too low to be useful for most of the applications without the recourse to an external acceleration.

One can note that the IEA spectra are quite irregular in comparison with the PBF ones. It depends on several factors which will be only mentioned here, referring to

Krasa *et al.* [67] for a more comprehensive discussion. First of all, an electron multiplier is employed to record very low ion currents by the IEA; in this way, it is recorded not just the incoming ion current, but an amplified current due to the electron multiplication by the dynodes. The gain of the electron multiplier depends not only on the detected ion species, its impact velocity and charge state, but also on the impact position on the first dynode. Apart from this latter factor, it is clear that the quality of the reconstruction of the ion spectra depends on the accuracy of the calibration of the electron multiplier. On the other side, the ion impact position on the first dynode can not be determined univocally. Lastly, shot-to-shot fluctuations in the plasma generation, *i.e.*, the intrinsic statistical uncertainty, would require several laser pulse for each spectrum point to get a satisfactory statistics.

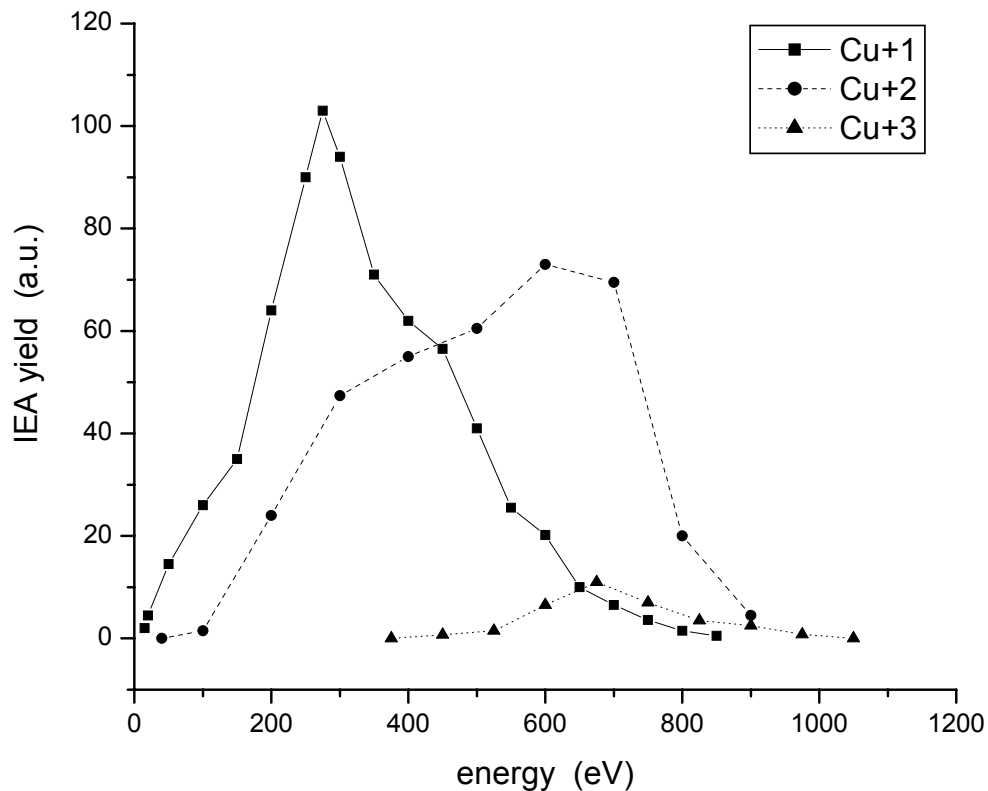


**Fig. 4.2.** Ion energy spectra for different charge states. The data were obtained by means of the IEA spectrometer.

It is evident that the relative abundance of the ion charge states is different in the PBF and IEA spectra. It depends on the acceptance angle of the spectrometer and on

the charge state angular distribution, as explained in Section 2.1. According to a common explanatory trend in the literature, very probably the reported data confirm the fact that higher charge state ions have more forward peaked angular distributions and are concentrated at small angles with respect to the plume axis. In fact, when recorded in the very small IEA acceptance angle, +2 ions reach about the same abundance than +1 ones and, correspondingly, the relative abundance of +3 ions increases slightly in comparison with the PBF spectra; see Eqs. (2.16) and following. Nevertheless, a suitable rescaling on the collection angle [59, 67], considering an expansion dynamics based on charge state-dependent shifted Maxwell-Boltzmann velocity distributions, allows to obtain the PBF spectra starting from the IEA ones, and vice versa. Anyway, due to the fact that the PBF spectrometer and the implantation area subtended the same solid angle with respect to the plasma point-source, the PBF results on charge state abundance have to be considered for the evaluation of the ion beam fluence and energy spectrum “seen”, on the average, by the implanted surface.

## 4.2 Ion fluence

The ion fluence available for implantation was estimated using FC diagnostics, as explained in Section 3.2, and taking into account the charge state distribution previously assessed. Typical ion current signals recorded by the FC are shown in Fig. 4.3, both for ions in free expansion and for accelerated ions. The data refer to Cu ions and to a single laser pulse.

The continuous curve is the TOF spectrum of ions in free expanding plasma. This trace lasts about 20  $\mu\text{s}$  and determines the duration of the extraction-implantation phase. The dotted curve is the signal recorded when the ions were accelerated, without suppression of the current due to the emission of secondary electrons from the FC surface. The dashed curve refers to the accelerated ions, with suppression of the secondary electron current. The effective duration (signal “on”) of the implanting bunch is about 15  $\mu\text{s}$ .

First of all, it is evident the shift of the leading edge of the TOF spectrum when the accelerating voltage was applied. The shift of the peak TOF is in good agreement with the calculation of the reduction in TOF, with respect to the free expansion, for

63.5 amu +1 ions crossing the 1.3 cm wide HV gap roughly in regime of uniformly accelerated motion and travelling from the GE to the FC (2.5 cm path length) in regime of uniform motion at 40 keV energy.

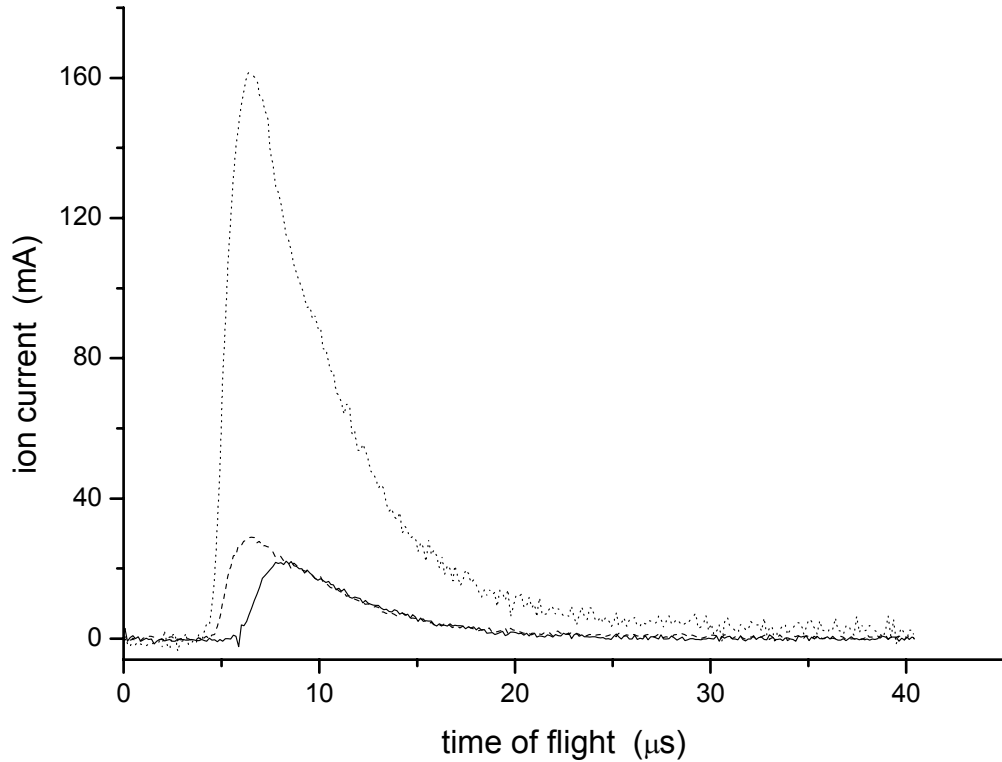


**Fig. 4.3.** Current signals of Cu ions recorded by the FC. Continuous curve: ions in free expanding plasma; dotted curve: accelerated ions, without suppression of the current due to the emission of secondary electrons from the FC; dashed curve: accelerated ions, with suppression of the secondary electron current. Note the shift of the leading edge of the time-of-flight spectrum when the accelerating voltage was applied.

Then, one can note also the dramatic decrease of the FC signal when the SR bias was applied, denoting a large yield of secondary electrons, as expected for the impact on metals of ions with energy of tens keV [60]. This finding confirms the prominent role of the secondary electrons ejected from the substrate and the aluminum GE in the striking of discharges during the acceleration stage. Such electrons are accelerated towards the EC and induce ionization mainly in the abundant neutral component.

*Inter alia*, such secondary ionization plays a significant role also in the increase of the overall charge revealed when the accelerating field was present in the gap, as it is evident by a comparison between the dashed and continuous curves in Fig. 4.3. Due to the acceleration of ions, the ionization process by ion – neutral impact yields a contribution as well. Actually, the effect of increasing the overall charge of the accelerated bunch is also provoked by the action of the gap electric field, whose lines of force tend to collect some of those ions which otherwise, moving in free expansion, would stay outside the geometrical acceptance of the GE hole after passing through the EC hole.

High current values were achieved, both for the free expanding ions and for the accelerated ones [68, 69]. For example, the current peak value for the accelerated Cu bunch reached about 30 mA. A peak value of about 40 mA/cm<sup>2</sup> could be estimated for the ion current density, averaged over the implantation area. The mean values for current and current density, averaged over the duration of the ion bunch, resulted in 15 mA per shot and 20 mA/cm<sup>2</sup> per shot, respectively.

The FC measurements were carried out before and after the implantation process, in order to check the stability of the ion fluence value even after some hundreds shots. Really, a slight decrease of the ion fluence was observed (10% - 20% after 500 shots, depending on the target material), due to the crater excavation. This effect was taken into account either calculating the mean value between the initial and final ion fluence or rotating the target from time to time during implantation. Nevertheless, in recent experiments the FC was utilized as an on-line beam monitor by letting a small leak not covered by the substrate in the GE hole. In this way the FC was able to detect a small portion of the accelerated beam and it was possible to record on the oscilloscope the relative variation of the ion fluence during implantation.

The number of accelerated ions corresponding to the +z charge state,  $N_z$ , was calculated by integrating the overall FC voltage signal,  $V_{ac}(t)$  (dashed curve in Fig. 4.3), and weighting it by the corresponding abundance coefficient. In detail, denoting by  $I_{ac}(t)$  the detected ion current, flowing through the FC load resistance,  $R$ , the Ohm's law gives:

$$I_{ac}(t) = \frac{V_{ac}(t)}{R} \quad (4.3)$$

where  $R = 50 \Omega$ , see Section 3.2. Then,

$$N_z = \frac{a_z}{e \sum_k k a_k} \int I_{ac}(t) dt \quad (4.4)$$

where the mean ion charge state is recognizable in the summation [67].

The ion fluence,  $F_z$ , of implanting ions with charge state  $z$  (and energy  $E_z$ ), was estimated as

$$F_z = \frac{N_z}{S} \quad (4.5)$$

where  $S$  is the area of the GE hole ( $\varnothing = 1 \text{ cm}$ ), bounding the implanted surface ( $S = 0.78 \text{ cm}^2$ ). The total ion fluence,  $F_t$ , of ions implanted per laser shot was calculated according to the following relation:

$$F_t = \sum_z F_z \quad (4.6)$$

The ion dose,  $D_z$ , of ions implanted with energy  $E_z$ , was calculated as the product between  $F_z$  and the number of laser shots,  $n$ , delivered during the implantation:

$$D_z = n F_z \quad (4.7)$$

The total ion dose,  $D_t$ , of implanted ions was calculated according to the analogous relation:

$$D_t = n F_t \quad (4.8)$$

Numerical values for  $N_z$ ,  $E_z$ ,  $F_z$ ,  $F_t$ ,  $D_z$  and  $D_t$  are reported in Table 4.1 for all the performed implantations. A 10% uncertainty should be considered, at least, for these data.

**Table 4.1.** Summary of the main parameters of the implanting ion beams and of the implantation conditions.

<b>Element</b>	<b>Al</b>	<b>Cu</b>	<b>Ge</b>
<b>N<sub>1</sub></b> ( x 10 <sup>10</sup> ions )	90	73	1.0
<b>N<sub>2</sub></b> ( x 10 <sup>10</sup> ions )	24	21	0.27
<b>N<sub>3</sub></b> ( x 10 <sup>10</sup> ions )	6.0	2.9	0.067
<b>F<sub>1</sub></b> ( x 10 <sup>10</sup> ions/cm <sup>2</sup> )	120	94	1.3
<b>F<sub>2</sub></b> ( x 10 <sup>10</sup> ions/cm <sup>2</sup> )	31	27	0.34
<b>F<sub>3</sub></b> ( x 10 <sup>10</sup> ions/cm <sup>2</sup> )	7.7	3.7	0.085
<b>F<sub>t</sub></b> ( x 10 <sup>10</sup> ions/cm <sup>2</sup> )	160	120	1.7
<b>E<sub>1</sub></b> ( keV )	40	40	40
<b>E<sub>2</sub></b> ( keV )	80	80	80
<b>E<sub>3</sub></b> ( keV )	120	120	120
<b>shots</b>	400	200	500
<b>D<sub>1</sub></b> ( x 10 <sup>12</sup> ions/cm <sup>2</sup> )	460	190	6.4
<b>D<sub>2</sub></b> ( x 10 <sup>12</sup> ions/cm <sup>2</sup> )	120	55	1.7
<b>D<sub>3</sub></b> ( x 10 <sup>12</sup> ions/cm <sup>2</sup> )	31	7.5	0.43
<b>D<sub>t</sub></b> ( x 10 <sup>12</sup> ions/cm <sup>2</sup> )	620	250	8.5
<b>Substrate</b>	Si(100) Si(111)	Si(100) Si(111)	Si(100) Si(111)

The total ion fluence was in the order of  $10^{10} - 10^{12}$  ions/cm<sup>2</sup> per pulse, depending on the target element. The total ion dose was chosen in the order of  $10^{13} - 10^{14}$  ions/cm<sup>2</sup>, after a simulation of the expected depth profiles, as explained in the next Section. Taking into account the sensitivity of the analytical techniques employed for the characterization of the implanted samples, such an order of magnitude for the total ion dose resulted in a concentration of the doping elements which usually assured a good detection quality along the depth profiles .

The separation in the TOF spectrum of the different ion groups, according to their charge state, is clearly visible in Fig. 4.4. The TOF spectrum was revealed as the one in Fig. 4.3 (dashed curve), using the FC coupled with the SR, except for the position of the detector, which in this case was placed in the drift tube at a greater distance from the acceleration gap. In such a way it was possible to carry out TOF mass-to-charge spectrometry and to resolve the bunches corresponding to the various ion species present in the accelerated beam.

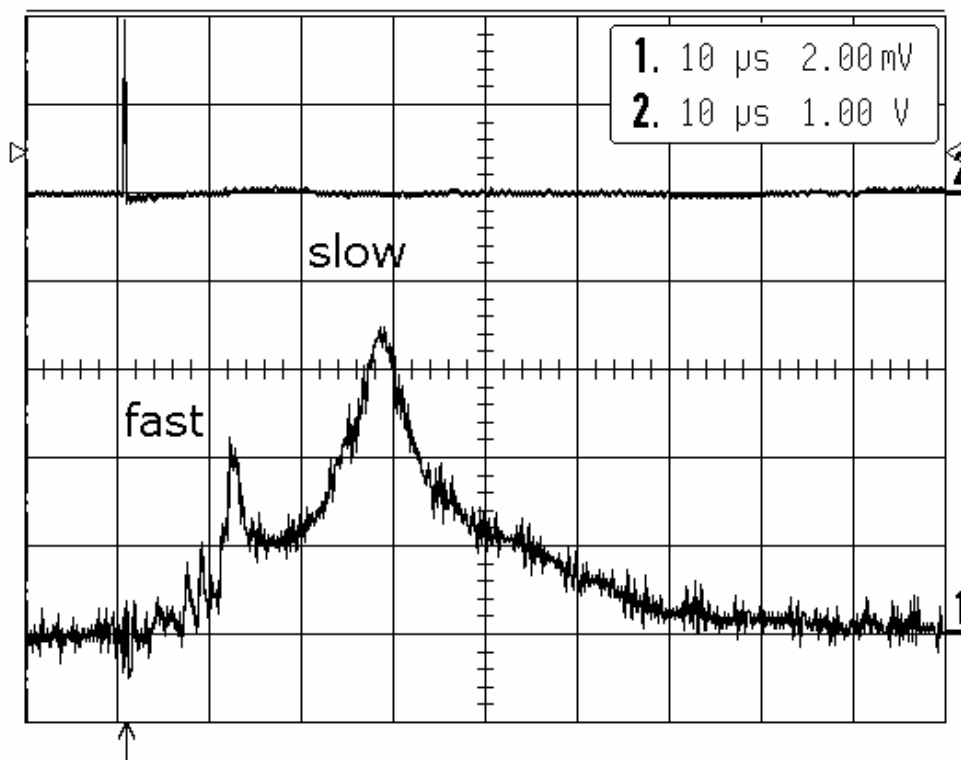


**Fig. 4.4.** Trace #1: Faraday cup signal, recorded along the drift tube, showing the TOF spectrum of the accelerated ion beam. Trace #2: laser pulse signal recorded by a fast photodiode and used as a trigger.

No trace of these components was evident in the TOF spectrum of Fig. 4.3, owing to the short path traveled by the accelerated ions and to the intrinsic temporal width, relatively large, of the ion groups which overlapped in the plasma bunch approaching the acceleration gap.

The fastest peaks in the TOF spectrum of Fig. 4.4 have TOF values compatible with low mass-to-charge ratios and initial kinetic energies of tens eV. These peaks are attributable to ions of hydrogen, elements adsorbed in the target,  $\text{Cu}^{+3}$  and  $\text{Cu}^{+2}$ . The slowest peak is due to  $\text{Cu}^{+1}$  ions.

### 4.3 Ion range distribution

The range,  $R$ , and the range straggling,  $\sigma$ , of ions implanted in amorphous Si ( $Z = 14$ ;  $M_a = 27.98$  amu; density:  $2.32 \text{ g/cm}^3$ ) were calculated by SRIM for the various values of  $E_z$ . The results are reported in Tables 4.2, 4.3 and 4.4 for Al ( $Z = 13$ ;  $M = 26.98$  amu), Cu ( $Z = 29$ ;  $M = 62.93$  amu) and Ge ( $Z = 32$ ;  $M = 73.92$  amu) ions, respectively. These data were useful *in primis* to estimate the maximum implantation depth and, next, to localize the contribution of the various ion groups with different energy in the simulated and measured depth profiles.

**Table 4.2.** Range and straggling values for implantation in Si of Al ions at the various energy values employed.

$E_z$ ( keV )	40	80	120
$R$ ( nm )	67	134	201
$\sigma$ ( nm )	29	51	70

**Table 4.3.** Range and straggling values for implantation in Si of Cu ions at the various energy values employed.

<b>E<sub>z</sub></b> ( keV )	40	80	120
<b>R</b> ( nm )	36	64	94
<b>σ</b> ( nm )	13	21	29

**Table 4.4.** Range and straggling values for implantation in Si of Ge ions at the various energy values employed.

<b>E<sub>z</sub></b> ( keV )	40	80	120
<b>R</b> ( nm )	33	59	84
<b>σ</b> ( nm )	11	18	25

SRIM calculations indicated roughly a maximum range of about 100 nm (including the straggling) for Cu and Ge implants, and of about 250 nm for the Al implant. Moreover, one can note that the range increases almost linearly as a function of the ion energy, as expected for energy values in this order of magnitude. So, the concentration peaks corresponding to the ion groups of different energy should be localized at regular steps in depth.

Simulations of the concentration profiles as a function of the penetration depth also were carried out by means of SRIM. A multi-energy beam was employed in the simulation, with the following energy spectrum,  $f(E)$ :

$$f(E) = \sum_z a_z \delta(E - E_z) \quad (4.9)$$

where  $E$  is the initial ion energy and  $\delta(\zeta)$  is the Dirac delta function with the usual normalization condition

$$\int_{-\infty}^{\infty} \delta(\xi) d\xi = 1 \quad (4.10)$$

Due to the similarity of the charge state distributions found for Al, Cu and Ge ions, standard values were chosen for the  $a_z$  coefficients, equal for all the three elements:

$$\begin{aligned} a_1 &= 0.75 \\ a_2 &= 0.20 \\ a_3 &= 0.05 \end{aligned} \quad (4.11)$$

Such a “standard” beam was employed in the simulations by changing only the implanting element from time to time, in order to generate depth profiles just for reference.

A total number of  $1 \cdot 10^5$  ions for each implanted element were simulated, following the above mentioned energy distribution. The resulting range distributions are reported in Fig. 4.5. The bin width is 1 nm. The distributions are normalized with respect to 1, but take into account that, for convenience, the histogram ordinate is reported in  $\text{cm}^{-1}$  rather than in  $\text{nm}^{-1}$ . In fact, it is easy to show that the stopping probability at a depth  $x$  per unit depth is equivalent to the ratio between the number density of implanted atoms at  $x$  and the fluence (or dose) of ions impinging on the sample surface. So, if the atom density and the fluence of incident particles are expressed, as usual, in  $\text{atoms}/\text{cm}^3$  and  $\text{atoms}/\text{cm}^2$ , respectively, then the stopping probability per unit depth has to be correspondingly expressed in  $\text{cm}^{-1}$ . Such considerations are very useful as they allow to calculate easily the expected dopant density at a depth  $x$ , by multiplying the ordinate value at  $x$  times the total ion dose  $D_t$ .

The shapes of the Cu and Ge depth profiles are quite similar, due to their close atomic mass values. Such a behavior is the consequence of the very close values for range and straggling at the same ion energy, as one can note by comparing Tables 4.3 and 4.4. On the contrary, the Al ions, lighter than the Cu and Ge ions, are expected to travel a considerably longer path in the Si bulk.

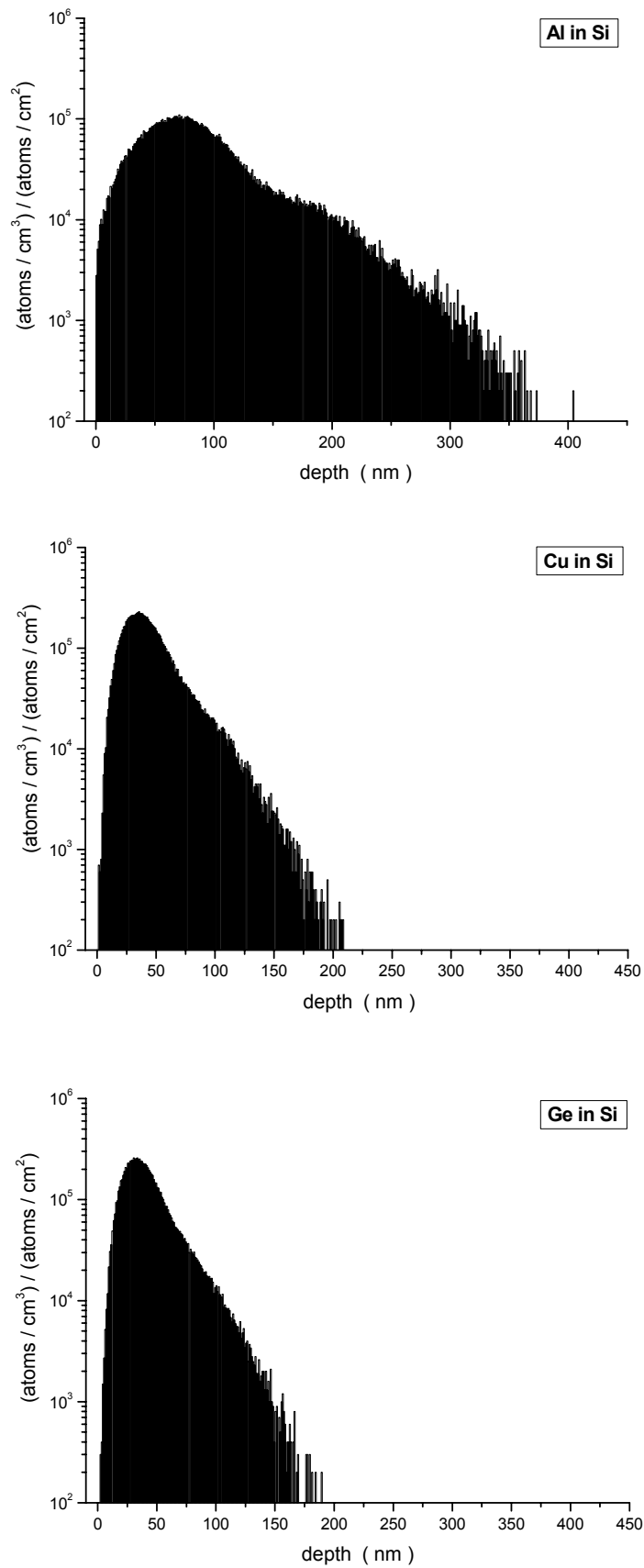


*Fig. 4.5. Range distributions of Al, Cu and Ge ions implanted in Si, as generated by a Monte Carlo simulation according to the multi-energy standard beam.*

As a consequence, the peak concentration of implanted atoms results higher for Cu and Ge ions with respect to Al ions, at the same ion dose. Expected numerical values of the peak atomic concentration are reported in Table 4.5.

However, one has to bear in mind that two important factors affected the actual depth profiles with respect to the simulation:

- the deposition of neutrals, which furthermore, having kinetic energy up to several hundreds eV, could be able to penetrate into the Si substrate up to a few nm;
- the contribution of the secondary ions produced in the extraction gap and only partially accelerated, which were distributed on a wide energy spectrum.

*Table 4.5. Expected values for peak density and concentration of implanted ions in Si, on the basis of the range distributions generated by SRIM. The values are given per single laser shot and for the total ion dose.*

<b>Implanted element</b>	<b>Al</b>	<b>Cu</b>	<b>Ge</b>
<b>F<sub>t</sub></b> ( x 10 <sup>10</sup> ions/cm <sup>2</sup> )	160	120	1.7
<b>Peak atomic density per laser shot</b> ( x 10 <sup>15</sup> atoms/cm <sup>3</sup> )	160	350	5.0
<b>D<sub>t</sub></b> ( x 10 <sup>12</sup> ions/cm <sup>2</sup> )	620	250	8.5
<b>Peak atomic density</b> ( x 10 <sup>18</sup> atoms/cm <sup>3</sup> )	62	70	2.5
<b>Peak atomic concentration</b> ( ‰ )	1.2	1.4	0.5

The deposition and co-implantation of neutrals resulted in a higher dopant concentration in the surface layer of the implanted samples, due to the high yield of neutrals with respect to ions (approximately in a ratio 10:1). The contribution of the

secondary ions produced in the extraction gap, and only partially accelerated, broadened this layer, resulting in overall concentration values higher than the simulated ones.

Referring to the Monte Carlo depth profiles in Fig. 4.5 and taking into consideration a concentration threshold of three orders of magnitude lower than the peak concentration, the endpoint of the range distribution can be established at a depth of about 400 nm for Al ions, and 200 nm for Cu and Ge ions.

The distribution peak is due to the 40 keV ions, of course. The presence of peaks related to 80 keV and 120 keV ions is not so clear in all the three profiles. This is due to the low relative abundance of the +2 ions with respect to the +1 ones, and of the +3 ions with respect to the +2 ones. In fact, on the basis of the charge state abundance values, the energy separation between an ion group and the next one is not enough to assure that the range straggling of the former does not cover the peak of the distribution of the latter.

Nevertheless, it is possible to observe a wide bump ranging from about 150 nm to 250 nm in the Al depth profile. It is due to the overlap of the 120 keV ion peak and the after-peak tail of the 80 keV ions; see Table 4.2 for comparison. The same “bump” effect can be made out at about 100 nm in the Cu and Ge profiles. Even in these cases it can be attributable to 120 keV ions; see Tables 4.3 and 4.4 for details.

Moreover, the presence of the +2 and +3 ion groups produces, in the descending part of all the three profiles, a clear deviation from the Gaussian shape expected for a monoenergetic beam. Such an asymmetry is particularly evident in the Al profile. For comparison, the depth profiles of the Al standard beam and of each beam component are shown separately in Fig. 4.6. The distribution in the upper panel is the summation of the three histograms in the lower panel, according to Eq. (2.31).

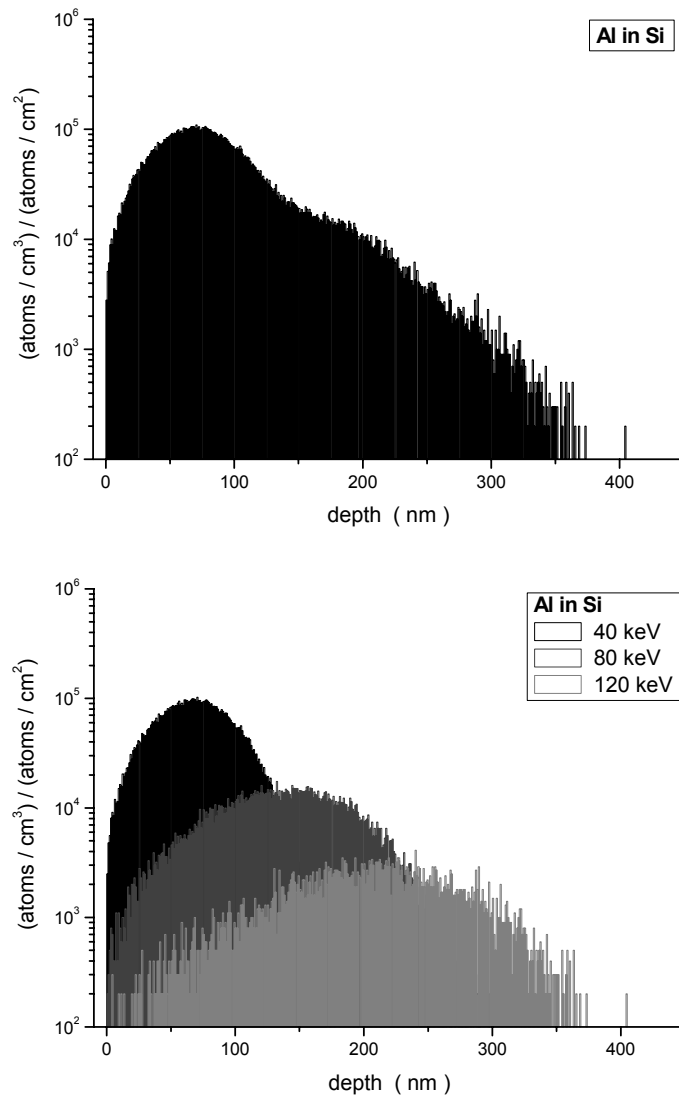


**Fig. 4.6.** Comparison between the overall depth profile of the Al ion standard beam (upper panel) and the range distributions of each beam component (lower panel).

#### 4.4 SEM-EDX analysis

SEM-EDX analysis was performed on the Al implanted samples, but these measurements did not reveal implanted ions, probably owing to the concomitance of several factors:

- large penetration depth of the probe electron beam in comparison with the thickness of the implanted layer;

- relatively low concentration of the dopant species;
- proximity of the Al and Si spectral lines;
- high background signal.

#### 4.5 RBS analysis

The RBS analysis performed at CEDAD, University of Lecce, Italy, on an Al implanted sample, did not reveal a significant spectrum for implantation, due to the overlap of the matrix (Si) and dopant (Al) signals. Apart from the low mass separation between Al and Si, which are adjacent elements in the periodic table, this measurement was particularly difficult because the matrix element was the heavier, so generating a backscattering spectrum which covered the signal from the analyte. On the other hand, the concentration of Al atoms was not sufficient to provide a clear peak or edge.

The RBS analysis at ETH, Zurich, Switzerland, was performed on a Ge implanted sample, operating at normal incidence and at a detection angle of  $115^\circ$  (“grazing exit”), in order to increase the count rate. The results are shown in Fig. 4.7.

One can note that the Ge signal-to-noise ratio (SNR) was poor, even for the relatively high implantation dose measured, *i.e.*,  $5 \cdot 10^{13}$  atoms/cm<sup>2</sup>. For reference, one must be aware that  $2 \cdot 10^{14}$  atoms/cm<sup>2</sup> is the amorphization threshold dose for Si [70]. The inferred implantation range, 150 nm, is in good agreement with the maximum range estimated by simulation. Moreover, the implantation depth measured by RBS has to be considered as a lower limit, because the sharp edge of the large Si signal limits the depth profiling range for Ge.

The RBS data permitted to calculate an implantation efficiency of the LIS-based system of approximately  $10^{11}$  atoms/cm<sup>2</sup> per laser pulse. This value is a factor of 10 higher than that recorded using the Faraday cup, because with RBS both charged (implanted) and neutral (deposited) particles are quantified, whereas the Faraday cup measurements provide information on charged particles only. The obtained value for the deposition-implantation fluence is in good agreement with own previous measurements that assessed a ratio of 1:10 among charged and neutral particles in the laser-produced plume [14].

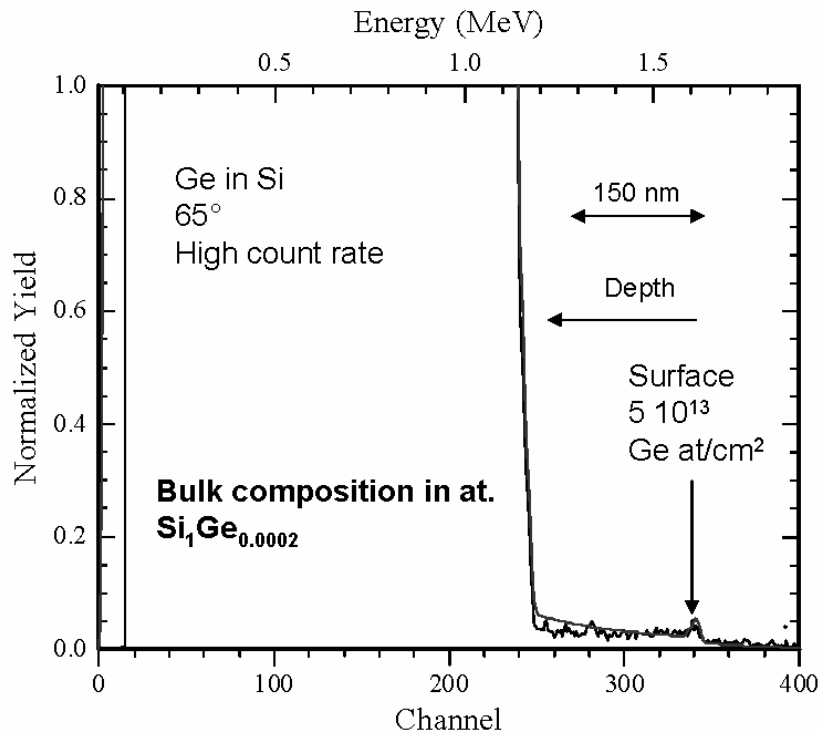


**Fig. 4.7.** RBS depth profiling of Ge implant in Si. The large band of Si covers all analytes in the region of lower masses (i.e., Al) and limits the depth profiling range.

A measurement on an Al implanted sample by means of the grazing exit configuration was tried at ETH as well, obtaining negative results also in this case. In fact, as it is evident in Fig. 4.7, the level of the Si signal is much higher (by orders of magnitude) with respect to the typical level of the analyte signal and, in such conditions, there was no chance to identify the signal from Al, stored in spectral channels below 250.

The poor SNR of the shown high depth resolution measurements (notwithstanding the high implantation dose) confirmed the necessity to implement high detection power analytical techniques for rapid and effective characterization of the implanted materials.

## 4.6 XPS analysis

XPS analysis was performed on Al and Cu implanted samples obtaining interesting results, with a good resolution in depth step (about 3 nm). Figure 4.8 shows the depth profiles.

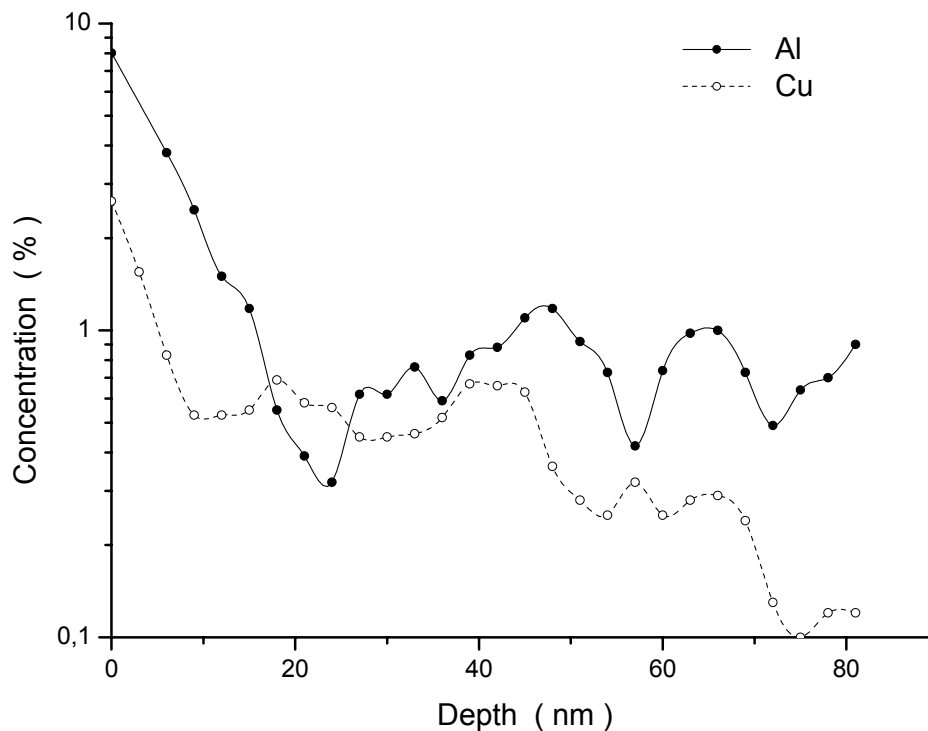


*Fig. 4.8. XPS depth profiling of Al and Cu implanted Si(111) samples.*

Near the surface one can see a decreasing trend of the atomic concentration for both the implanted elements. The concentration is rapidly decreasing in the first 10 nm depending on the analyte, and further below the profile is somehow jagged. The former effect can be ascribed to the neutral particles which, having kinetic energies of the order of hundreds eV, can be able to penetrate into the Si substrate up to a few nm. Also ions produced in the extraction gap by electron impact and only partially accelerated can contribute.

As regards the internal structures of the profiles, they are almost uniformly distributed on a range of a few tens nm and are attributable to the multi-energy components of the accelerated bunch and to their energy band width. High energy

secondary ions produced in the extraction gap, exhibiting a wide energy spread, contribute to this deeper implantation as well. In the Al profile, for depth values higher than 30 nm, the XPS trace probably reproduces the wide and squat peak of the corresponding histogram in Fig. 4.5, although a lot of fluctuations are present in the experimental profile. As regards the Cu profile, range data in Table 4.3 would suggest that the peaks around 40 nm and 60 nm are due to 40 keV and 80 keV ions, respectively. Even in this case the Monte Carlo profile appears more uniform and smooth than the experimental one.

In Fig. 4.8 it is possible to locate a cut-off for the Cu concentration at a depth of about 80 nm, while for the Al implanted sample the significant implantation range exceeds the measurement depth. Really, deeper measurements in the Cu implanted sample probably would have shown the 120 keV ions peak, which is located around or below 80 nm at concentration values of about 0.1%. An indication can be noted at the end of the trace. See, as a reference, Table 4.3 and the corresponding histogram of Fig. 4.5, in which a slight bump can be noted around 100 nm.

By XPS spectra the deposited-implanted dose was estimated to be approximately of the order of  $10^{15}$  atoms/cm<sup>2</sup>, in agreement with plasma diagnostics.

## 4.7 LA-ICP-MS analysis

LA-ICP-MS analyses were performed on Al, Cu and Ge implanted samples, at EMPA, Duebendorf, Switzerland. Such a technique allowed to estimate the presence of the implanted species with great sensitivity, but unfortunately these measurements resulted to be poor in depth resolution for the present case. With LA-ICP-MS it was not possible to define the monolayer-scale profile structure, but the implantation range could be correctly assessed resorting to a suitable ablation sampling or data processing.

The use of pulsed lasers for mass sampling produces individual aerosol batches, each one related to an ablated depth of 10 - 100 nm/pulse [71, 72] depending on the irradiance and wavelength. Such ablation depth would indeed be satisfactory for the purpose of determining the concentration profiles of ion implants. Ideally, the dopant content of such individual batches should be determined immediately, in order to obtain a pulse-resolved profiling. Nevertheless, aerosol dispersion within the ablation cell as well as along the transfer tubing contribute to pulse mixing and signal tailing,

respectively. Pulse mixing is due to the fact that the aerosol residence time inside the ablation cell is longer than the laser pulse-to-pulse interval, *e.g.*, 100 ms for 10 Hz repetition rate. Pulse-to-pulse crosstalk is controlled by the geometry of the ablation set-up (flow pattern), by the gas flows rate, and the analyte content, too.

LA-ICP-MS is usually performed in repetition rate mode and it works properly for deep implants (more than 1  $\mu\text{m}$ ) and regular depth profiles, providing acceptable depth resolution by a simple calibration of ablation time vs. crater depth, notwithstanding pulse mixing and signal tailing effects. Instead, problems arised with shallow depth profiles such as were obtained in the case of the LIS implanted samples. Nevertheless, the utilisation of LA-ICP-MS for the present analyses was just aimed at trying to improve the performances of this technique in the sub- $\mu\text{m}$  depth range. Furthermore, it should be not underestimated that the laser ablation facility used to implant might as well be implemented for on-site analytical characterization of the implanted samples.

The result of the measurement on a Ge implanted sample is reported in Fig. 4.9 as a function of the ablation time. The ablation time was calibrated against the ablation depth to obtain information on the depth distribution of the implant. The calibration procedure was carried out by measuring the crater profiles, which are shown in Fig. 4.10. To obtain the average ablation depth per pulse one divides the crater depth by the corresponding number of laser shots delivered. Results for Si(111) showed a crater depth of  $116 \pm 16 \mu\text{m}$ , where the roughness and non-planar floor of the crater were responsible for the 14% measurement uncertainty. For the Si(100) sample a value of  $107 \pm 6 \mu\text{m}$  was obtained. From these values, an average ablation depth of 96 nm/pulse for the Si(111) sample and 89 nm/pulse for the Si(100) sample could be calculated.

It is evident that such a depth step is even higher than the whole depth range sampled by XPS. But the main problem was that it resulted too wide with respect to the maximum implantation range obtained by the numerical simulation, so providing few experimental points (and with poor analytical significance) in the depth profile. The possibility to reduce the ablation sampling depth by significantly reducing the fluence of the laser beam, as shown to be successful for femtosecond systems [73], is risky for nanosecond laser ablation, because it would occasionally introduce element-dependent fractionation effects, as discussed elsewhere [74].

The direct conversion of the ablation time scale into the depth scale by means of the simple calibration described up to here resulted in a not realistic implantation depth of several microns. In fact, the trace of Fig. 4.9 indicates that only after 250 laser pulses the Ge signal, ranging from about 25s (signal onset) to 45 s, finally reaches the background level. Similar exaggerated results were found for Al and Cu implanted samples.

Indeed, extensive signal tailing stretches temporally the real concentration profile, which is an effect of set-up-related signal dispersion. In fact, the whole Ge peak has to be correctly attributed to shallow material removal by the first 3 - 4 laser shots. Therefore, LA-ICP-MS traces were more limited by signal dispersion than by depth resolution of laser sampling. Even in the case of reported ablation depths of 5-10 nm [73], the time required to entrain the aerosol out of the ablation cell into the tubing always extends the signals along the time axis, degrading the true profile as well as the pulse resolution.

An alternative LA-ICP-MS acquisition approach was developed to overcome the limitations due to signal dispersion and keep individual pulses resolved, *i.e.*, single shot profiling.

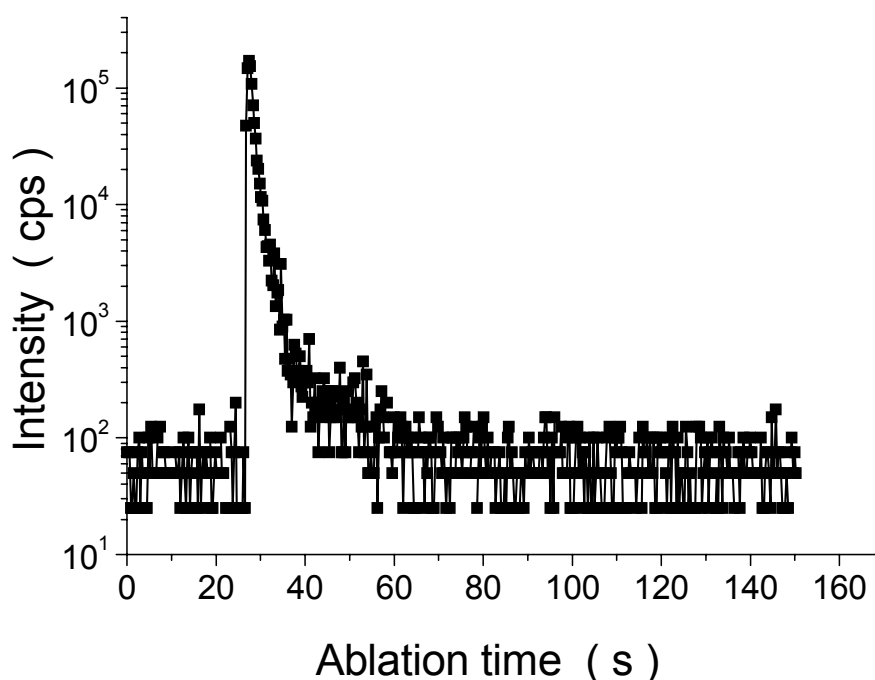


**Fig. 4.9.** Ge signal from LA-ICP-MS analysis of an implanted sample.

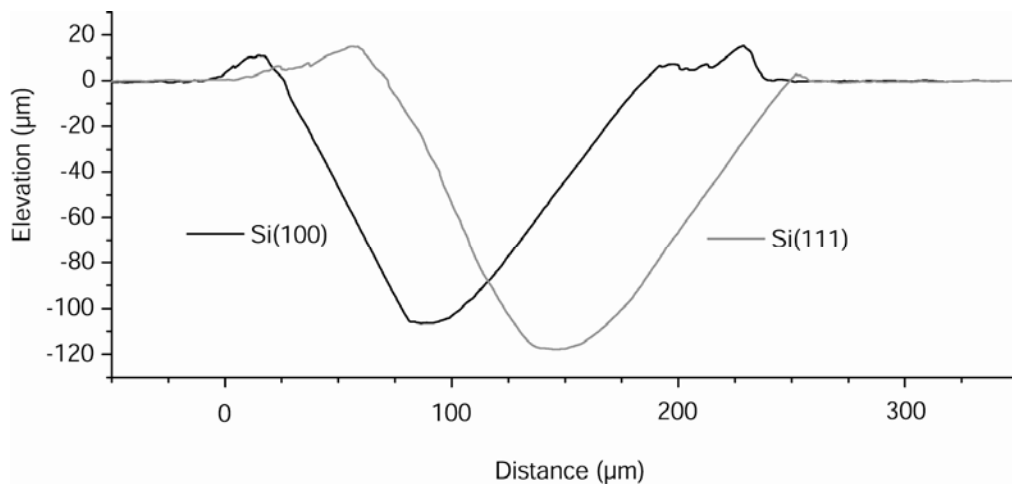


**Fig. 4.10.** Profile of ablated craters. An average ablation depth of 96 nm/pulse for the Si(111) sample and 89 nm/pulse for the Si(100) sample was calculated.

#### 4.8 Further analyses by LA-ICP-MS

Single shot profiling was realized by delivering one single pulse onto the implanted sample and letting the signal wane down to background level before releasing the next pulse. This (time consuming) approach permitted to obtain a pulse-resolved sequence of single shots whose integrals represented data points of the analyte concentration profile in the host material.

Fig. 4.11 shows the Ge profile in Si(100), where the Si yield has been used as internal standard to correct for shot-to-shot fluctuations. Shot-to-shot fluctuation in the ablation yield and in the ICP-MS system is in fact the main problem in single shot profiling.

The ablation depth per pulse was reduced down to about 50 nm by means of suitable expedients. Qualitatively the shape of the Ge profile compares well with the simulation results shown in Fig. 4.5, taking into account the contribution of neutrals and not fully accelerated ions in the first nanometres. The depth profile was tracked up to an analyte concentration 1000 times lower than its peak value (which was assumed equal to 1 as a reference value, see the first bin in the histogram of Fig. 4.11). The implantation depth related to the minimum detected concentration was found between

350 and 400 nm. Such a value was much higher than the maximum range determined by simulation, probably owing to crater effects.

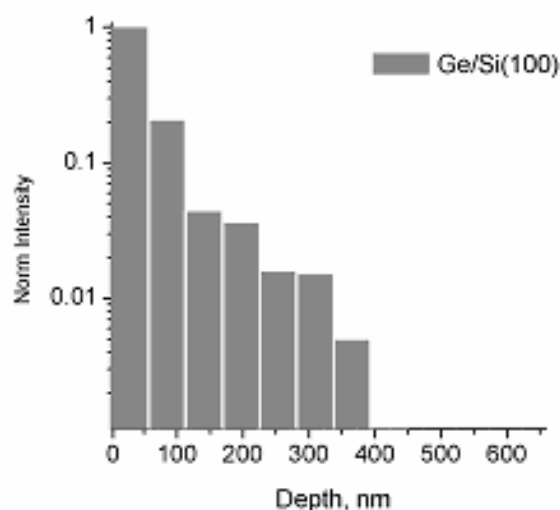


**Fig. 4.11.** Single shot profiling of Ge in Si(100). The Si signal (here not shown) was used as internal standard to correct for shot-to-shot fluctuations.

As regards the crater effects, one should use super-Gaussian laser beam profiles (commonly called “flat-top”) in order to avoid inter-layer mixing. Flat-top profiles guarantee homogeneous fluence over the whole irradiated surface. Unfortunately, the LA-ICP-MS system employed for the present measurements implemented an unstable resonator-type laser source, which generated a Bessel profile (so-called “ring” profile), resulting, after a great number of shots, in the crater profiles shown in Fig. 4.10. Therefore, the reliability of this analytical technique for depth profiling at very low concentrations could be improved using an energy-homogenised laser beam.

The optimization procedures discussed so far could be defined as *ab initio*, since they were all devoted to improve the quality of the results by finding optimum measurement conditions and operative techniques from the beginning. However, parallel to this, an alternative approach was developed to be able to re-process the data after their acquisition in repetition shot profiling, in order to correct for the bias introduced by signal dispersion.

In any case, the ablation time scale can be correctly transformed into the ablation depth scale by the above discussed approach using profilometry (*i.e.*, determining the ablation depth per pulse and multiplying it by the number of pulses per unit time). Instead, the signal intensity values need a suitable mathematical processing to recover the actual analytical information. In fact, due to signal dispersion, it is not generally true that a signal corresponding to a certain depth (its abscissa) is proportional to the analyte concentration at that depth, but such a signal represents the overlap of signals related to different positions within the sample up to that depth.

For this purpose, a deconvolution algorithm was developed, which provides a more appropriate assessment of the intensity – depth relation, taking into account the pulse mixing effect. Such a deconvolution technique is fully described in the Appendix.

## 5. A NOVEL FAST PULSER BY TRANSMISSION LINES FOR ION EXTRACTION

### 5.1 Introduction

In this Chapter it is illustrated the theoretical analysis, design, computer simulation, experimental realization and test of a circuit able to compress a rectangular voltage pulse and to increase its amplitude. Such a device can be useful to apply the high voltage to the acceleration gap in AC mode, generating single or repeated fast pulses with sub- $\mu\text{s}$  duration.

High voltage rectangular pulses of ultra-short duration are required in many industrial and research applications [75-78]. Generally, the generation of high voltage pulses is easily obtained until some hundreds kV by conventional circuits. For higher values, new pulse compression techniques must be developed. Normally, transmission line circuits offer the possibility of realizing fast rectangular pulses.

Unfortunately, a pulse forming circuit composed of a single transmission line halves the output voltage in application with a matched load. In single pulse forming lines (SPFLs), the corresponding current pulse is as high as  $V_C / 2R_0$ , where  $V_C$  is the line charging voltage and  $R_0$  is its characteristic impedance. The pulse duration,  $T$ , is given by  $T = 2\tau l$ , where  $l$  is the length of the line and  $\tau$  is the delay per unit length. Figure 5.1 shows a sketch of a SPFL.

The halving of the voltage occurring in this pulser is a great disadvantage, particularly when high output voltages are required. In order to avoid the voltage halving, the so-called “Blumlein line” [79] was developed, which is able to provide rectangular pulses of the same charging voltage,  $V_C$ , on a load impedance of  $2R_0$ , for a duration of  $2\tau l$ . The current value results in  $V_C / 2R_0$ .

The analysis of a novel voltage compressor (NVC) constituted by a transmission line circuit is reported here. Such a device is able to provide a rectangular matched pulse with a halved time duration, equivalent current and doubled voltage compared to the input pulse values. So, this technique can overcome many bias problems concerning the ion sources.

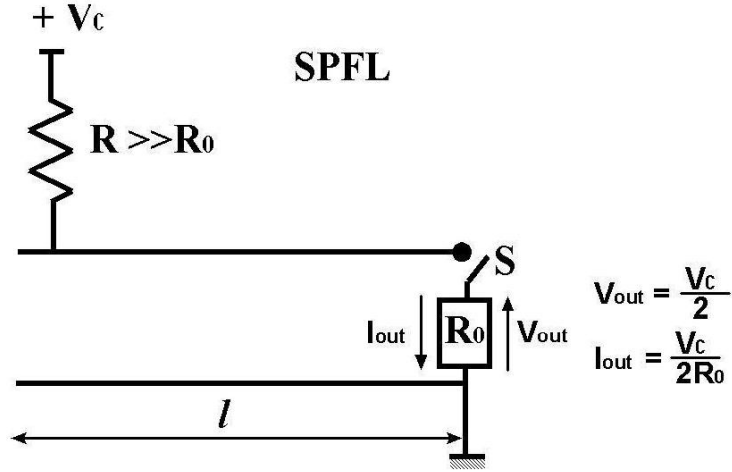


**Fig. 5.1.** Schematic sketch of a SPFL closed on its characteristic impedance  $R_0$ .  $S$ : fast switch;  $R$ : charging resistor.

## 5.2 Basic theory

The NVC working principle lies in the following reasoning. Let us consider the problem of determining voltage and current in two semi-infinite transmission lines (denoted as *line 1* and *line 2*) connected in series through a resistance  $R_l$  as in Fig. 5.2, when in each line a rectangular pulse travels towards the terminal in common with  $R_l$ .

Let the voltage of these pulses be expressed by:

$$V_{in,1}(x_1, t) = V_{0,1} \{ u(t - t_1 + \tau x_1) - u[t - (t_1 + T_1) + \tau x_1] \} \quad (5.1a)$$

$$V_{in,2}(x_2, t) = V_{0,2} \{ u(t - t_2 + \tau x_2) - u[t - (t_2 + T_2) + \tau x_2] \} \quad (5.1b)$$

where  $u$  is the Heaviside function;  $x_1$  and  $x_2$  are the spatial coordinates, oriented as in Fig. 5.2 ( $x_1, x_2 \geq 0$ );  $V_{0,1}$  and  $V_{0,2}$  are the voltage amplitudes;  $T_1$  and  $T_2$  are the pulse durations;  $t_1/\tau$  and  $t_2/\tau$  are the distances of the pulse leading edge from the line terminal ( $x_1, x_2 = 0$ ) at the time  $t = 0$ . Let  $R_0$  be the characteristic impedance of both lines and  $v = l/\tau$  be the propagation velocity of the signals.

In general, when a pulse reaches  $R_l$ , reflections will be produced in both lines at  $x_j = 0$  ( $j = 1, 2$ ) and a net current will flow through  $R_l$  from a line into the other one

and vice versa. Here, for *reflection* it is meant any progressive pulse, propagating towards increasing  $x$  values in the opposite direction with respect to the input pulse one. Actually, when the input pulse reaches the position  $x_j = 0$ , some of the stored energy is reflected backwards, while other is transmitted towards the other line through  $R_l$ . This last dissipates a fraction of the energy by Joule effect. In what follows the transmitted pulse will be regarded as a *reflection* in the line where it is travelling. Such a terminological convention is particularly useful when both input pulses are present at the same time on  $R_l$  and in each line the properly reflected component and the one transmitted from the other line add themselves in a single progressive pulse. In what follows conditions on the problem parameters ( $V_{0,j}$ ,  $t_j$ ,  $T_j$ ,  $R_l$ ) are established in order to avoid such *reflected pulses*.

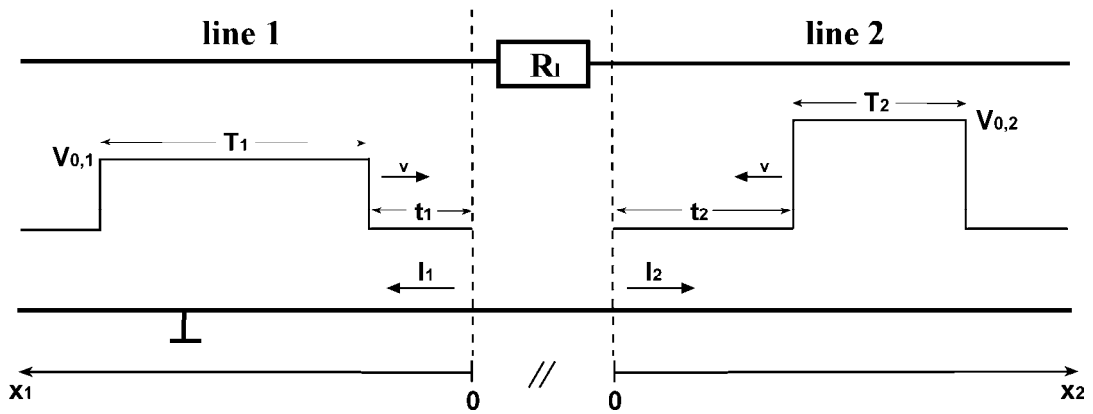


**Fig. 5.2.** System used to illustrate the theoretical basis of the voltage compressor.

In our case, indicating the voltage and current in the line  $j$  by  $V_j(x_j, t)$  and  $I_j(x_j, t)$ , respectively, their Laplace transforms,  $v_j(x_j, p)$  and  $i_j(x_j, p)$ , are in the well known form

$$v_j(x_j, p) = \alpha_j(p)e^{-px_j} - \beta_j(p)e^{px_j} \quad (5.2a)$$

$$i_j(x_j, p) = \frac{I}{R_0} [\alpha_j(p)e^{-px_j} + \beta_j(p)e^{px_j}] \quad (5.2b)$$

where  $\alpha_j(p)$  and  $\beta_j(p)$  ( $j = 1, 2$ ) are unknown functions to be determined by the boundary conditions.

For clearness, let us consider a simpler situation with  $t_1 = t_2 = 0$  and  $T_1 = T_2 = T_0$ . First of all, one can note that

$$-\beta_j(p)e^{px_j} = v_{in,j}(x_j, p) \quad (5.3)$$

where  $v_{in,j}(x_j, p)$  is the Laplace transform of  $V_{in,j}(x_j, t)$ . In fact,  $V_{in,j}(x_j, t)$  is the only regressive pulse in the problem.

In order to determine the  $\alpha_j$ 's, continuity condition of the flow of the net current through  $R_l$ ,  $I_{R_l}(t)$ , has to be imposed:

$$-I_1(0, t) = I_{R_l}(t) = I_2(0, t) \quad (5.4)$$

where the  $I_{R_l}$  sign has been chosen to be equal to the  $I_2$  one. Another boundary condition is given by the Ohm's law applied to the voltage fall on  $R_l$ :

$$V_1(0, t) - V_2(0, t) = R_l I_{R_l}(t) \quad (5.5)$$

By Laplace transforming Eqs. (5.4) and (5.5) and making use of Eqs. (5.2) and (5.3), a system of two equations in the unknowns  $\alpha_j(p)$  is obtained. The solutions are expressed by the following relations:

$$\alpha_1(p) = (R_l V_{0,1} + 2R_0 V_{0,2})P(p) \quad (5.6a)$$

$$\alpha_2(p) = (2R_0 V_{0,1} + R_l V_{0,2})P(p) \quad (5.6b)$$

where

$$P(p) \equiv \frac{1 - e^{-pT_0}}{(2R_0 + R_l)p}$$

The  $\alpha_j$ 's are the Laplace coefficients related to the reflected pulses. The condition to have  $\alpha_1=0$  is:

$$R_l V_{0,1} + 2R_0 V_{0,2} = 0 \quad (5.7a)$$

while the request to nullify  $\alpha_2$  is

$$2R_0 V_{0,1} + R_l V_{0,2} = 0 \quad (5.7b)$$

So,  $\alpha_1$  and  $\alpha_2$  are simultaneously null if and only if

$$R_l = 2R_0 \quad \text{and} \quad V_{0,1} = -V_{0,2} \quad (5.8)$$

In the end, in order to avoid reflections, the load resistance  $R_l$  must be twice than the characteristic impedance  $R_0$  and the input pulses must be synchronized and must have the same period and opposite voltage amplitude. Moreover, one can note that in such conditions, the difference of potential at  $R_l$  ends is equal to  $2V_{0,1}$  and the current through  $R_l$  is  $V_{0,1} / R_0$  for all the pulse duration, namely:

$$V_1(0,t) - V_2(0,t) = 2V_0 \{u(t-t_0) - u[t - (t_0 + T_0)]\} \quad (5.9a)$$

$$I_{R_l}(t) = \frac{V_0}{R_0} \{u(t-t_0) - u[t - (t_0 + T_0)]\} \quad (5.9b)$$

where

$$t_0 = t_1 = t_2, \quad T_0 = T_1 = T_2, \quad V_0 = V_{0,1} = -V_{0,2}$$

These theoretical results and a special circuit scheme were utilized in order to obtain the compression of a pulse, halving its duration and doubling its voltage amplitude.

### 5.3 Experimental design

Referring to Fig. 5.3, the NVC consists of a single pulse forming line (FL) connected in series to a storage line (SL) through a  $2R_0$  load impedance and a switch (S1). The FL line is long  $l$ , while the SL is long  $l/2$ . The load impedance can be short-circuited by means of a second switch (S2). The FL free terminal is open, while the SL one is always short-circuited.

The starting conditions are the following: the FL line is charged at a voltage  $V_C$  and the S2 switch is closed. At the time  $t=0$  the S1 switch closes the FL on the SL. Voltage and current in the FL,  $V_{FL}(x,t)$  and  $I_{FL}(x,t)$ , respectively, are given by the following relations [80], graphed in Fig. 5.4:

$$V_{FL}(x,t) = V_0 \{2u(t) - u(t - \tau x) - u[t - \tau(2l - x)]\} \quad (5.10a)$$

$$\text{for } 0 \leq t < \tau l$$

$$I_{FL}(x,t) = I_0 \{u(t - \tau x) - u[t - \tau(2l - x)]\} \quad (5.10b)$$

where  $V_0 = V_C / 2$  and  $I_0 = V_0 / R_0$ ; while in the SL the analogous relations are the following:

$$V_{SL}(x,t) = V_0 \{u(t - \tau x) - u[t - \tau(l - x)]\} \quad (5.11a)$$

$$\text{for } 0 \leq t < \tau l$$

$$I_{SL}(x,t) = I_0 \{u(t - \tau x) + u[t - \tau(l - x)]\} \quad (5.11b)$$

So, after S1 shutting, a leading edge of voltage  $-V_C/2$  and current  $V_C/2R_0$  travels in the FL with velocity  $v = -l/\tau$ , for a time  $0 \leq t \leq \tau l$  (see Fig. 5.4). Instead, in the SL a pulse of voltage  $V_C/2$  and current  $V_C/2R_0$  travels with velocity  $v = l/\tau$ . Then, at  $t = \tau l/2$ , it is reflected at the SL short-circuited terminal, giving rise to a pulse of voltage  $-V_C/2$  and current  $V_C/2R_0$  travelling backwards with velocity  $v = -l/\tau$ .

At  $t = l\tau$ , S2 switches off. For  $t > l\tau$  the situation is equivalent to have two pulses with  $t_0 = l\tau$ , opposite voltage amplitude and same duration  $T_0 = l\tau$  on the  $R_l$

ends in the circuit of Fig. 5.2. So, reflections are absent and voltages and currents in the two lines are given even by Eqs. (5.10) as regards FL, while  $V_{SL}$  and  $I_{SL}$  become:

$$V_{SL}(x,t) = -V_0 \{u[t - \tau(l+x)] - u[t - \tau(2l-x)]\} \quad (5.12a)$$

for  $t \geq l\tau$

$$I_{SL}(x,t) = I_0 \{2u(t) - u[t - \tau(l+x)] - u[t - \tau(2l-x)]\} \quad (5.12b)$$

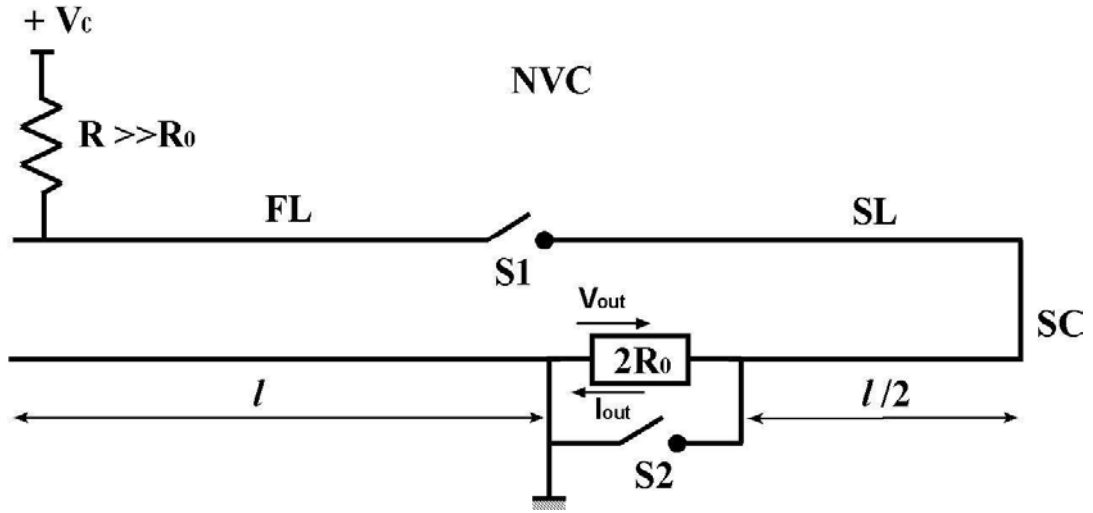


**Fig. 5.3.** Schematic sketch of the voltage compressor circuit, NVC. FL: transmission line; SL: storage line;  $2R_0$ : load impedance;  $R$ : charging resistor;  $S1$  and  $S2$ : fast switches.

The voltage  $V_{out}(t)$  and current  $I_{out}(t)$ , on the load impedance, are given by Eqs. (5.9a) and (5.9b), respectively, which become, by the substitutions  $t_0 = l\tau$ ,  $T_0 = l\tau$ :

$$V_{out}(t) = 2V_0 \{u(t - \tau l) - u(t - 2\tau l)\} \quad (5.13a)$$

$$I_{out}(t) = I_0 \{u(t - \tau l) - u(t - 2\tau l)\} \quad (5.13b)$$

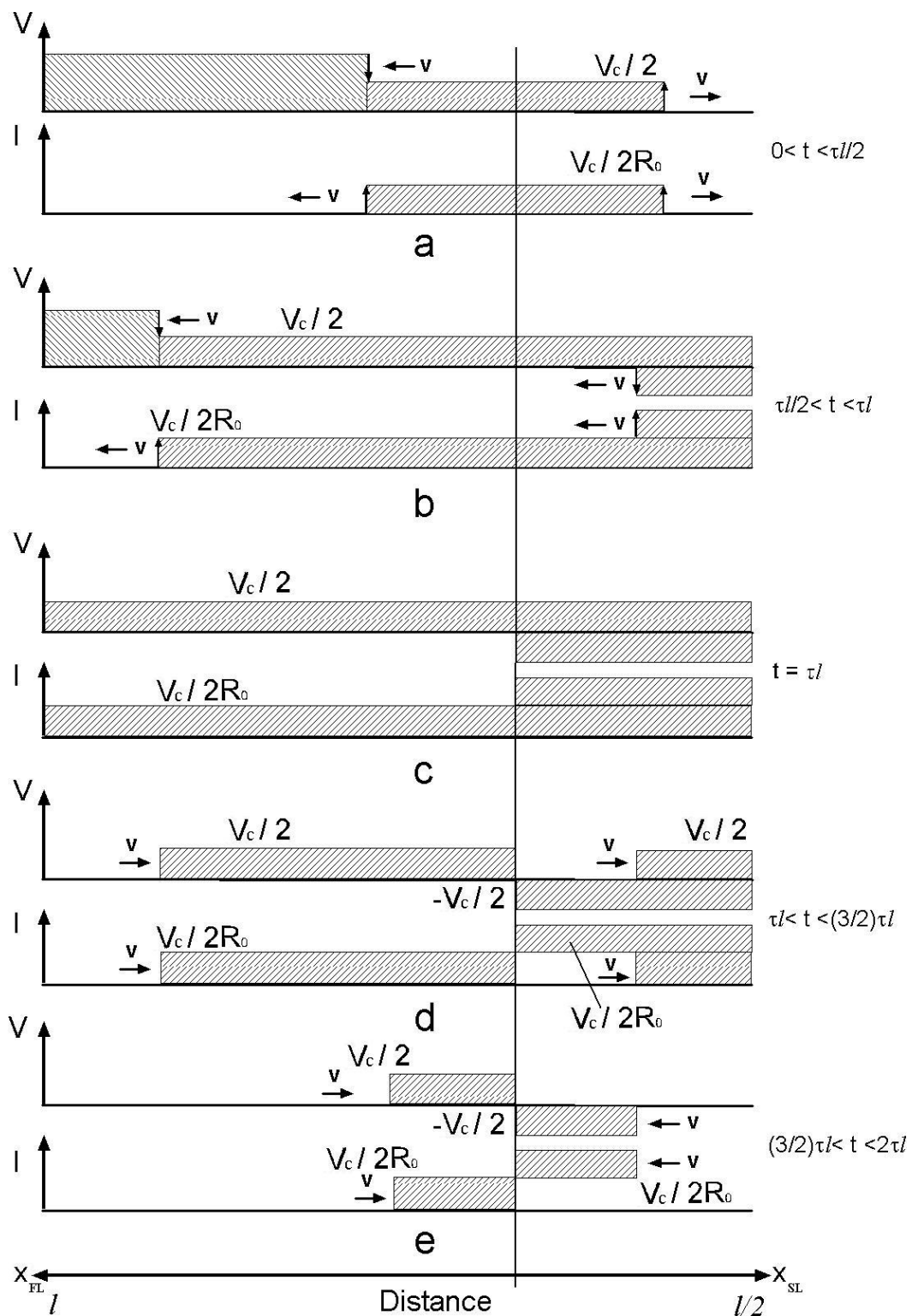


**Fig. 5.4.** Diagram of voltage and current along the lines at a)  $0 < t < \frac{1}{2}l\tau$ ; b)  $\frac{1}{2}l\tau < t < l\tau$ ; c)  $t = l\tau$ ; d)  $l\tau < t < \frac{3}{2}l\tau$ ; e)  $\frac{3}{2}l\tau < t < 2l\tau$ .  $v$  is the pulse velocity.

In such a way, an input pulse, expressed by  $V_{FL}(0, t)$ , with duration  $2\tau l$ , voltage  $V_0$  and current  $I_0$ , can be compressed in a matched output pulse,  $V_{out}(t)$ , with halved duration ( $\tau l$ ), doubled voltage ( $2V_0$ ) and equivalent current ( $I_0$ ).

## 5.4 Analytical treatment

Here a rigorous analysis of the NVC circuit for  $t \geq l\tau$  is presented, including boundary conditions at the NVC ends and effective starting conditions at  $t = l\tau$ . A generic value for  $R_i$  is considered. The analysis for  $0 \leq t < \tau l$  can be easily deduced by Ref. 80. By utilizing the same notation of Section 5.2, the general Laplace-transformed differential equations for the two transmission lines are the following:

$$\frac{\partial}{\partial x_j} v_j(x_j, p) = -\tau R_0 p i_j(x_j, p) + \tau R_0 i_{0,j}(x_j) \quad (5.14)$$

$$\frac{\partial}{\partial x_j} i_j(x_j, p) = -\frac{\tau}{R_0} p v_j(x_j, p) + \frac{\tau}{R_0} v_{0,j}(x_j)$$

where now  $j$  stands for FL or SL,  $p$  is the Laplace variable corresponding to the time variable  $t' = t - l\tau$  and  $v_{0,j}(x_j)$ ,  $i_{0,j}(x_j)$  represent starting conditions ( $t' = 0$ ) for voltage and current in the line  $j$ . By using Eqs. (5.10) and (5.11), the following relations are obtained:

$$\begin{aligned} v_{0,FL}(x_{FL}) &= V_{FL}(x_{FL}, \tau l) = V_0 \\ i_{0,FL}(x_{FL}) &= I_{FL}(x_{FL}, \tau l) = -I_0 \end{aligned} \quad (5.15)$$

$$\begin{aligned} v_{0,SL}(x_{SL}) &= V_{SL}(x_{SL}, \tau l) = 0 \\ i_{0,SL}(x_{SL}) &= I_{SL}(x_{SL}, \tau l) = 2I_0 \end{aligned}$$

Solutions for the system (5.14) are expressed by the relations

$$v_{FL}(x_{FL}, p) = \alpha_{FL}(p)e^{-p\tau x_{FL}} - \beta_{FL}(p)e^{p\tau x_{FL}} + \frac{V_0}{p} \quad (5.16a)$$

$$i_{FL}(x_{FL}, p) = \frac{I}{R_0} \left[ \alpha_{FL}(p)e^{-p\tau x_{FL}} + \beta_{FL}(p)e^{p\tau x_{FL}} - \frac{V_0}{p} \right] \quad (5.16b)$$

for the line FL, and by

$$v_{SL}(x_{SL}, p) = \alpha_{SL}(p)e^{-p\tau x_{SL}} - \beta_{SL}(p)e^{p\tau x_{SL}} \quad (5.17a)$$

$$i_{SL}(x_{SL}, p) = \frac{I}{R_0} \left[ \alpha_{SL}(p)e^{-p\tau x_{SL}} + \beta_{SL}(p)e^{p\tau x_{SL}} + 2\frac{V_0}{p} \right] \quad (5.17b)$$

for the line SL, where  $\alpha_{FL}(p)$ ,  $\beta_{FL}(p)$ ,  $\alpha_{SL}(p)$  and  $\beta_{SL}(p)$  are unknown functions to be determined by the following boundary conditions:

i) FL open end (at  $x_{FL} = l$ )

$$i_{FL}(l, p) = 0 \quad (5.18a)$$

ii) SL short-circuited end (at  $x_{SL} = l/2$ )

$$v_{SL}(l/2, p) = 0 \quad (5.18b)$$

iii) current flow continuity through  $R_l$  (see Section 5.2)

$$-I_{FL}(0, p) = I_{R_l}(l, p) = I_{SL}(0, p) \quad (5.18c)$$

iv) voltage fall on  $R_l$

$$V_{FL}(0, p) - V_{SL}(0, p) = R_l I_{R_l}(l, p) \quad (5.18d)$$

Substituting expressions given by Eqs. (5.16) and (5.17) into Eqs. (5.18), the following system is obtained:

$$\alpha_{FL} e^{-p\tau l} + \beta_{FL} e^{p\tau l} - \frac{V_0}{p} = 0 \quad (5.19a)$$

$$\alpha_{SL} e^{-p\tau l/2} - \beta_{SL} e^{p\tau l/2} = 0 \quad (5.19b)$$

$$\alpha_{FL} + \beta_{FL} + \alpha_{SL} + \beta_{SL} + \frac{V_0}{p} = 0 \quad (5.19c)$$

$$R_0\alpha_{FL} + R_0\beta_{FL} - (R_l + R_0)\alpha_{SL} - (R_l - R_0)\beta_{SL} - (2R_l - R_0)\frac{V_0}{p} = 0 \quad (5.19d)$$

Solutions for the Laplace coefficients are the following:

$$\alpha_{FL}(p) = (R_l - 2R_0)\frac{V_0}{p} \frac{\delta(\delta - 1)}{\Delta} \quad (5.20a)$$

$$\beta_{FL}(p) = \frac{V_0}{p} \frac{(R_l + 2R_0)\delta - R_l}{\Delta} \quad (5.20b)$$

$$\alpha_{SL}(p) = -2\frac{V_0}{p} \frac{\delta[R_l\delta - (R_l - R_0)]}{\Delta} \quad (5.20c)$$

$$\beta_{SL}(p) = -2\frac{V_0}{p} \frac{R_l\delta - (R_l - R_0)}{\Delta} \quad (5.20d)$$

where

$$\delta \equiv e^{p\tau}$$

$$\Delta \equiv (R_l + 2R_0)\delta^2 - 2R_0\delta - (R_l - 2R_0)$$

Laplace antitransforms of Eqs. (5.16) and (5.17) have not analytical expressions when the coefficients are given by Eqs. (5.20), except for the cases  $R_l = 2R_0$  and  $R_l = 0$ . Reflections at the  $R_l$  ends for  $\tau l < t < 2\tau l$  can be evaluated by the simplified analysis exposed in Section 5.2, substituting in Eqs. (5.6)

$$t_1 = t_2 = \tau l, \quad T_1 = T_2 = \tau l, \quad V_{0,1} = -V_{0,2} = V_0$$

Considering just the case  $R_l = 2R_0$ , Eqs. (5.20) reduce to

$$\alpha_{FL}(p) = 0 \quad (5.21a)$$

$$\beta_{FL}(p) = \frac{V_0}{p\delta} \quad (5.21b)$$

$$\alpha_{SL}(p) = -\frac{V_0}{p} \quad (5.21c)$$

$$\beta_{SL}(p) = -\frac{V_0}{p\delta} \quad (5.21d)$$

By inserting these Laplace coefficients into Eqs. (5.16) and (5.17), and antitransforming, voltage and current in the two lines as functions of  $t'$  are obtained. The substitution  $t' = t - l\tau$  gives the suitable expressions as functions of  $t$ , for  $t \geq l\tau$ , namely Eqs. (5.10) and (5.12).

## 5.5 Simulation

The behaviour of the NVC was preliminarily tested by using a circuit simulator software, “Pspice” [81]. Figure 5.5 shows the circuit scheme employed for the simulation. In this experimental setup the FL was used as a SPFL in order to generate the rectangular pulse applied to the SL. 12 m and 6 m long 50  $\Omega$  coaxial cables were employed for the FL and the SL, respectively;  $\tau = 5$  ns/m for both transmission lines. Two transistors, TS1 and TS2, were used as switches. The load resistance was R2. The charging voltage was limited by the maximum operating voltage of the lines and switches used in this experiment. It was chosen a maximum input voltage of 300 V, given through a charging resistance R1 much larger than  $R_0$ . The resistance R4 was required because the simulator needed that the short-circuited end of the SL was also grounded; actually, lacking R4, a floating potential at that end was returned.

At  $t = 0$  TS1 switches on, and after 60 ns TS2 switches off. Figure 5.6 shows the result of the simulation when the R2 value is 100  $\Omega$ . The upper trace shows the voltage waveform at the exit of the FL line (input pulse), as sampled by the probe P1. The lower trace shows the compressed output pulse, as sampled by the probe P2. Simulated waveforms confirm analytical solutions given in Eqs. (5.10) and (5.13). Spikes are present in both signals, due to the finite time increment used in numerical calculation.

Computer simulation is particularly useful in analyzing the NVC behaviour when the value  $R_l$  of the load resistance is different from  $2R_0$  and difficulties arise in antitransforming the Laplace coefficients. In such a situation, multiple reflections arise not only at the load resistance ends (as in the ideal case discussed in Section 5.2,

dealing with semi-infinite lines), but even at the FL open end and SL short-circuited end.

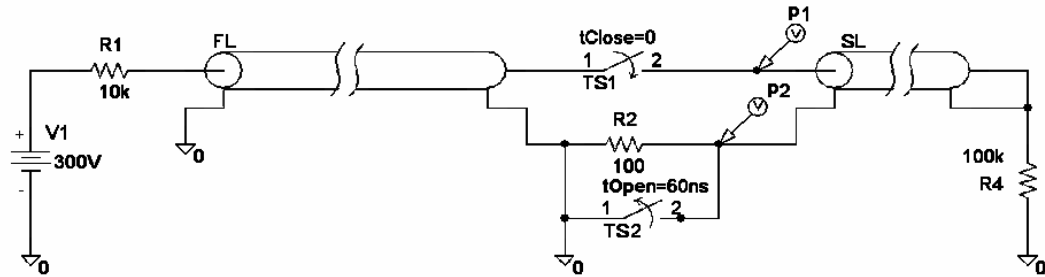


*Fig. 5.5. Circuit scheme employed for the NVC simulation.*

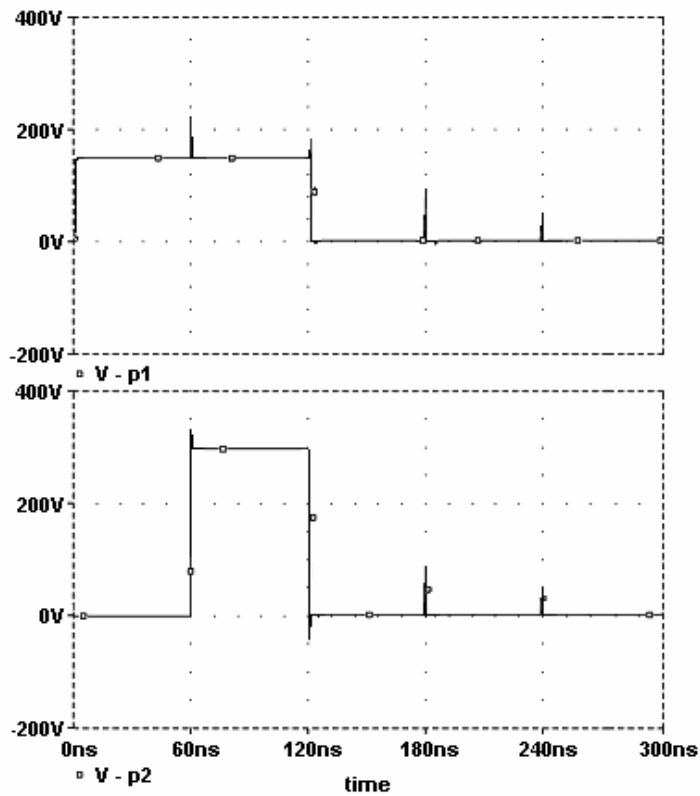


*Fig. 5.6. Simulated waveforms of the voltage pulses obtained by the NVC when the charging voltage value is 300 V. The upper trace shows the waveform at the exit of the FL line; the lower trace shows the waveform on the 100  $\Omega$  load resistor. The maximum output voltage is 300 V.*

As an example, the NVC behaviour when  $R_l$  is  $50 \Omega$  was simulated. Waveforms sampled by P1 and P2 are shown in Fig. 5.7. Multiple *reflections* (in the sense of Section 5.2) propagate and add themselves along the lines. Changes in waveforms occur at 60 ns steps, due to the length of the lines. Signal attenuation is due to the energy loss on the load by Joule effect. It should be underlined that the  $100 \Omega$  resistance realizes the fastest energy transfer to the load.

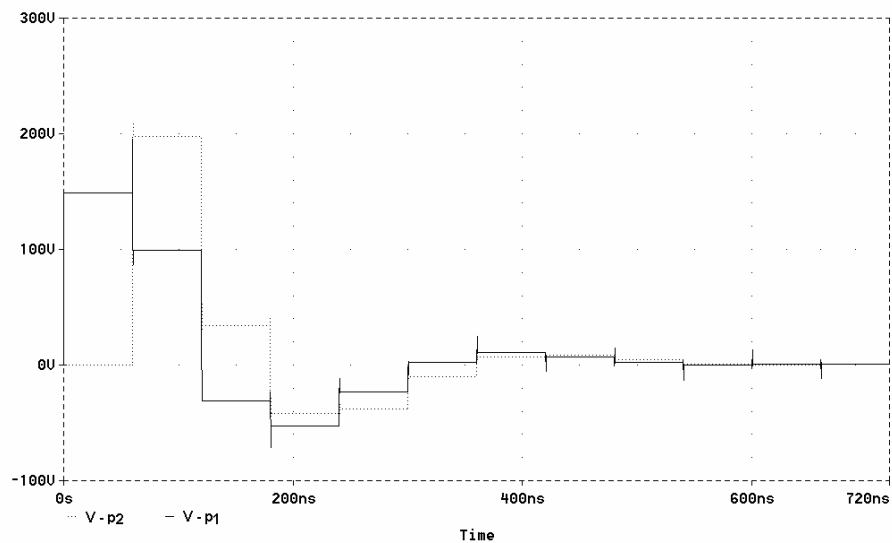


**Fig. 5.7.** Simulated waveforms of the voltage pulses obtained by the NVC when the load resistance value is  $50 \Omega$ . The continuous trace shows the waveform at the exit of the FL line; the dotted trace shows the waveform on the load resistor.

## 5.6 Experimental apparatus and results

Figure 5.8 shows the sketch of the experimental circuit. The components are as described above, except for the absence of the resistance  $R_4$ . Two fast transistor switches (Behlke HTS 21-14) were used as TS1 and TS2, and a  $100 \Omega$  resistor was used as load impedance. Two voltage probes, P1 and P2, were used to analyze the circuit, as shown in Fig. 5.8. The TS1 and TS2 switching was triggered by an external circuit.

The experimental results are shown in Fig. 5.9. The lower trace shows the voltage at the exit of the FL line, measured by P1. It presents a discontinuity after 60

ns owing to a parasitic capacitance of the transistor TS2 during its aperture. The upper trace shows the output pulse, measured by P2, 300 V high, 60 ns wide, as predicted by Eqs. (5.13). Experimental and simulated waveforms are in excellent agreement.

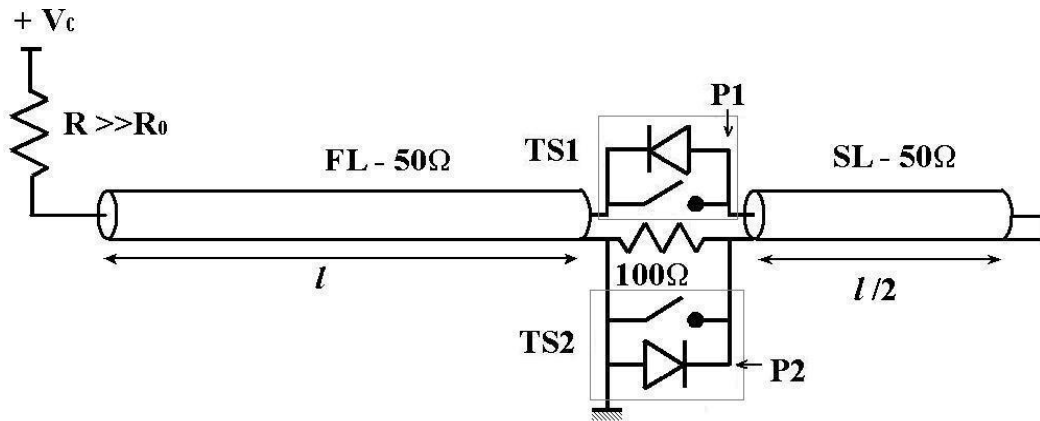


**Fig. 5.8.** Schematic sketch of the NVC apparatus. FL: 50  $\Omega$ , 12 m long transmission line, used as SPFL; SL: 50  $\Omega$ , 6 m long storage line; R: charging resistor; TS1 and TS2: fast transistor switches; P1 and P2: high impedance oscilloscope probes.

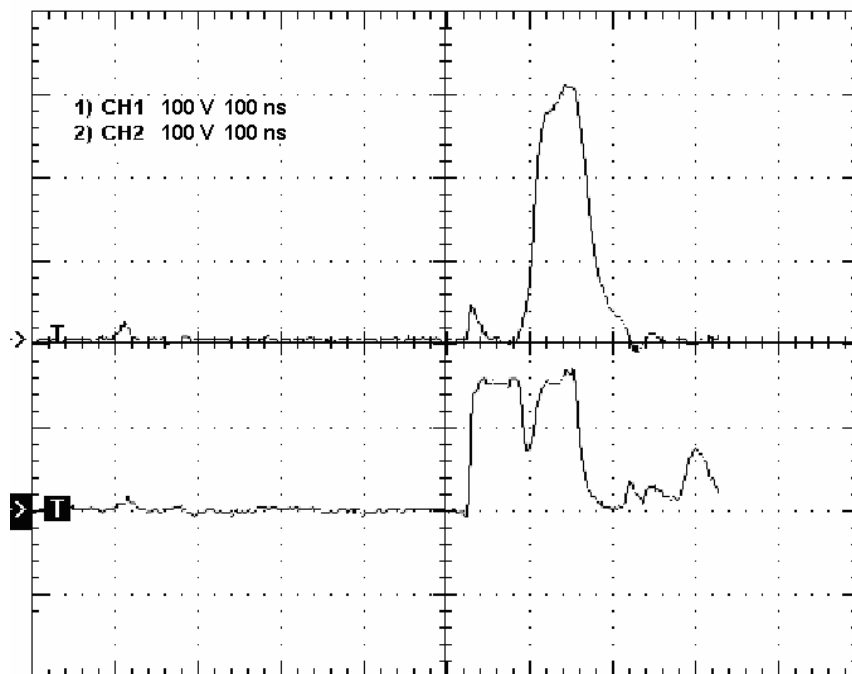


**Fig. 5.9.** Waveforms of the voltage pulses measured on the NVC with a charging voltage of 300 V. The lower trace shows the waveform at the exit of the FL line; the upper trace shows the waveform on the 100  $\Omega$  load resistor. The maximum output voltage is 300 V.

## 5.7 Discussion

The compression factor achieved by means of the voltage compressor was 2 (halved duration, doubled voltage). The compression factor could be increased to  $2^n$  by connecting in cascade  $n$  NVC circuits, each of the proper sizes and suitably triggered.

The NVC can be useful to apply the high voltage to the acceleration gap of the LIS chamber in AC mode, in order to avoid arcing when such a phenomenon can not be controlled or limited in DC mode. The use of the AC mode becomes indispensable, if one wants to retain the simple extraction-implantation configuration here employed, when higher accelerating voltage values (quite a lot of tens kV) and/or higher ion flux values are required. In such a case, the gap bias voltage has to be delayed for several microseconds with respect to the laser pulse [13] and/or the bias pulse duration has to be suitably reduced with respect to the plasma bunch one.

In extreme conditions, a single or repeated high voltage fast pulses, with duration of tens or hundreds ns, could be necessary. The NVC characteristics make it a useful biasing device in this working regime. The utilization of a train of short pulses (50 – 100 ns), with a period of some  $\mu$ s, is particularly attractive in order to cover the whole duration of the plasma bunch ( $\sim 15 \mu$ s at the extraction point), so maximizing the yield of extracted ions. For this purpose, the TS1 and TS2 switches should be suitably triggered by an external time unit; moreover, the SPFL stage of the NVC could be replaced by an external pulser with lower performances, so using the FL just as an input line and eliminating the presence of the TS1 switch. Experiments on ion implantation in AC mode by using the NVC will be carried out in the future.

## 6. CONCLUSIONS

### 6.1 Summary of the main results

The importance of developing LISs has been recently motivated by the application of ion beams for surface modifications of different materials, by the realization of complex thin films and by the construction of hybrid ion sources based on a combination of LIS and ECR sources. Among the advantages of employing LISs, it will be recalled here the ability to ionise every element, even from non-conductive or refractory targets; the easiness to produce plasma utilising commercially available lasers of high power; the high ion yield per laser shot; the generation of high charge state ions; and the possibility to get mixed ion beams by irradiation of multi-elemental targets.

In the present work, experiments aimed at demonstrating the feasibility of ion implantation via LIS, at tens - hundreds keV energy, have been reported. A compact and versatile LIS, employing an external electric field (+HV, DC) for ion acceleration, was set up, characterized and tested for implantation.

An excimer laser (KrF, 248 nm wavelength, 70 mJ/pulse and 23 ns FWHM pulse duration) was pulsed on solid targets, in order to allow the generation and expansion of a plasma bunch. Typically, the laser beam was focused on the various targets in a 1 mm<sup>2</sup> spot, with an irradiance of about  $3.5 \cdot 10^8$  W/cm<sup>2</sup>.

By applying a high voltage on the LIS accelerating gap, ions were extracted from the ablated plasma and accelerated towards a substrate. What appeared immediately evident was that the technique of acceleration and the geometry of the experimental configuration had to be suitably planned and implemented in order to avoid arcing in the plasma and, in case, the deposition of the neutral component on the substrate surface. In fact, the developed experimental set-up provided that, before reaching the extraction gap, the plasma plume had the possibility of expanding adiabatically inside a suitable “expansion chamber”, connected mechanically and electrically to the target stem, which the extraction potential was applied to. Such a setup allowed to apply a positive high voltage in DC mode. Implantations of Al, Cu and Ge ions in Si substrates were carried out operating at 40 kV acceleration voltage and 1 Hz laser repetition rate.

At the extraction point, the abundance of the various ion species was determined mainly by the ion angular distributions in the free expanding plasma, and its knowledge was of primary importance in forecasting the shape of the implantation profiles. Assuming a phenomenological model for the plasma plume, which emphasized the presence of various “groups of particles”, useful equations and scaling laws were derived for several physical quantities of interest in ion diagnostics, extraction and implantation, such as the particle density; the angular distribution and forward peaking; and the ion current and fluence.

The relative abundance and the energy distribution of the various ion charge states freely expanding in the laser plasma were characterized by means of two electrostatic TOF spectrometers: a potential barrier spectrometer and an IEA with deflecting electrodes. Charge states up to +3 were revealed. For all three ablated materials, the relative abundance values in the extraction solid angle were roughly in the ratio 1:0.25:0.07 for +1, +2 and +3 ions, respectively. Previous measurements assessed a ratio of about 1:10 between charged and neutral particles in the laser-produced plume. The overall ion fluence was measured using Faraday cup diagnostics, both on the free expanding plasma and on the accelerated beam, and was in the order of  $10^{10}$  -  $10^{12}$  ions/cm<sup>2</sup> per pulse, depending on the ablated material. The implantation area was circular in shape, 1 cm in diameter, and covered an acceptance solid angle of about  $3 \cdot 10^{-3}$  sr with respect to the plasma point-source on the target.

Most of this information was utilized for the computer simulation of the depth profiles in the implanted samples, by employing the well-known SRIM Monte Carlo code. Actual profiles were affected by two other important factors which was not possible to take into account in the simulation:

- deposition of neutrals, which furthermore, having kinetic energies up to several hundreds eV, could be able to penetrate into the Si substrate up to a few nm;
- the contribution of the secondary ions produced in the extraction gap and only partially accelerated, which were distributed on a wide energy spectrum.

The implanted samples were characterized by means of several analytical techniques, SEM-EDX, RBS, XPS and LA-ICP-MS, commissioned to various national and foreign laboratories. An implantation range wider than 100 nm resulted for all the implants, in good agreement with the theoretical estimates for ions having an energy of

40 keV per unit charge. Long tails at very low concentration were generally found in the depth profiles, due to range straggling of +2 and +3 ions.

XPS resulted the most accurate analytical technique for this shallow and complex depth profiling. XPS measurements showed a profile modulation which could be very probably ascribed to the co-presence of ion components characterized by different energy values. The contribution of the neutral particles was evident in the surface layer (up to a few nm) of the implanted samples. RBS measurements also showed a strong deposition of the neutrals on the substrate surface. RBS and XPS results allowed an estimate of the ion fluence in agreement with the electrostatic detectors, as well as an estimate of the plasma fractional ionization in agreement with previous measurements. The order of magnitude of the measured analyte density ranged from  $10^{19}$  to  $10^{16}$  atoms/cm<sup>3</sup> per laser pulse along the implantation range. For reference, the Si atomic density is about  $5 \cdot 10^{22}$  atoms/cm<sup>3</sup>. Such values have to be compared, for example, with the typical concentrations used for doping in electronics:  $\sim 10^{13}$  atoms/cm<sup>3</sup> in weakly doped Si and up to  $10^{20}$  atoms/cm<sup>3</sup> in heavily doped Si (n<sup>+</sup>, p<sup>+</sup>).

LA-ICP-MS offered the possibility to drill easily the implanted substrates and allowed to estimate the maximum implantation depth. On the other side, depth resolution was poor. Anyway, the applicability of LA-ICP-MS for LIS implantation characterization was investigated for three main reasons:

- affinity of LA-ICP-MS with many topics relevant for the research on LIS and ion implantation;
- to try to improve the performances of this technique in the sub- $\mu\text{m}$  depth range;
- the possibility of implementing on-site analytical characterization of the implanted sample in the same laser ablation system used to implant.

Problems arised with shallow depth profiles such as were obtained in the case of the LIS implanted samples. Notwithstanding the good detection power (up to  $10^{-5}$  in atomic concentration for the present analyses), the depth resolution, crater effects and pulse mixing resulted critical factors hard to be overcome. Many efforts were done both to correct signal analysis for pulse mixing and to avoid this effect at all. In the former approach, which was based on signal acquisition in repetition laser shooting, a deconvolution algorithm was developed; in the latter case, single shot profiling was employed, obtaining satisfactory results. The implementation of the signal

deconvolution algorithm in the present analyses was strongly biased by the poor depth resolution, resulting in few “effective” data points, and by signal fluctuations and noise, resulting in a little accurate determination of the signal waning time constant. All these factors has to be improved and kept under control if one wants to apply LA-ICP-MS for fine and fast analyses of so shallow implants.

To conclude, the results of the present study point out that the LIS implantation has the potential to become an important tool for modification of the surface layers of solids, in order to improve material properties (*e.g.*, hardness, wear and corrosion resistance, coefficient of dry friction, etc.).

## 6.2 Performances

The LIS performances for ion implantation are encouraging, especially with respect to PIII. In fact, ion dose values of the order of  $10^{12}$  ions/cm<sup>2</sup> are on the high-end of doses observed in conventional PIII.

On the contrary, typical values for the extracted current found in the present study, 10 – 20 mA, averaged over the whole duration of the ion bunch ( $\sim 15$   $\mu$ s), are hard to be compared with commercial beamline implanter, usually working in the range 1 – 10 mA, but with stationary beams. Moreover, the beam size can reach 20 cm<sup>2</sup> for low current ( $< 1$  mA) implanter. On the other side, such devices are enormously expensive ( $\sim 1$  M\$).

Nevertheless, it should be pointed out that the implantation efficiency, namely the ratio between the number of implanted ions and the overall number of produced ions, was very low for the experimental set-up employed in this study, due to the narrow extraction solid angle ( $3 \cdot 10^{-3}$  sr). Taking into account measurements on the ion angular distribution [58], it was possible to estimate an implantation efficiency of the order of  $10^{-3}$  for Cu<sup>+1</sup> ions, on the basis of Eqs. (2.22) and (2.27). An improvement of this figure of merit would result in a corresponding increase of the implantation current.

Moreover, a low laser repetition rate was used precautionarily in these experiments, in order to avoid complications with the striking of discharges. The laser repetition rate is another important parameter to be considered for increasing the average current in pulsed implantation.

Experiments on ion implantation from ablation plasma were carried out also by Qi *et al.* [13], who used the two experimental configurations shown in Fig. 1.3, namely: in one case the substrate and laser target surfaces were oriented parallel to one another, while, in the other case, the target was perpendicular to the substrate. Qi *et al.* generated plasma in the same conditions employed in the present study, namely by means of a KrF laser (248 nm wavelength, 20 ns pulse duration), whose beam was focused to a fluence on the target between 5 and 20 J/cm<sup>2</sup>. The laser was operated at a higher repetition rate, 10 Hz. The laser target consisted of Ti, while the substrates were Si wafers or Al alloy disks. The distance between the ablation spot and substrate was about 4 cm for both the configurations.

In the configuration of Fig. 1.3a (target parallel to substrate), Qi *et al.* needed a HV pulse, suitably delayed with respect to the laser pulse, in order to avoid arcing between the negatively biased substrate and the target. Such a solution required the application of a rather complex timing technique. On the contrary, in the configuration of Fig. 1.3b (target perpendicular to substrate), they were able to accelerate ions by applying HV in DC mode. In any case, at so short target-substrate distances, *i.e.*, high plasma density ( $\sim 10^{14}$  ions/cm<sup>3</sup> [13]), the accelerating voltage values they used were severely limited, without any doubt, by the occurrence of discharges. The maximum HV value referred in their work is about 8 kV. They obtained an implanted dose of the order of 10<sup>12</sup> ions/cm<sup>2</sup> per pulse, just as it was typically found in the present study. Nevertheless, they refer an implantation efficiency of the order of 10%, much higher than the value estimated in this study.

The basic difference between Qi's approach and the present one is in the ion extraction. In the former case, the ion extraction occurs through a wide Child sheath, just as in PIII; in the latter, a suitable extractor is employed, consisting of an expansion chamber and an extraction-acceleration gap. Although in a minimal configuration, such an extraction system makes this technique more similar to ion gun implantation than PIII. In fact, the present set-up has got all the characteristics of an ion source for accelerators. The well-defined geometrical characteristics of the accelerated bunch assure a better directionality of the implanting ion flux, a more uniform dose distribution over the implanted surface and a higher definition of the boundary of the implantation surface. In Qi's set-up a wider variability in performances is expected as a function of the accelerating potential.

### 6.3 Further developments

In the future, the research activity will be devoted to the following aspects:

- maximization of the ion dose per laser pulse, by means of the optimization of the extraction technique and, in case, the employment of a focusing magnetic field;
- increase of the repetition rate of the laser pulse;
- increase of the ion penetration depth, by employing higher charge states and accelerating voltages;
- identifying and testing of practical applications of the implantation technique via LIS.

A more sophisticated version of expansion chamber, just realized, will be used in the short-term. It has a cylindrical geometry, coaxial with the target, and its structure is modular, telescopic and adjustable. A photograph is reported in Fig. 6.1. It will allow to adapt the expansion length to various density regimes of the plasma, depending on the laser beam irradiance and the extraction voltage. Moreover, it will allow a more efficient and rapid evacuation of the ablated material from its interior, offering the possibility to work at high laser repetition rate.

Experiments on ion implantation by applying HV in AC mode have been planned in the next future. If one wants to retain the simple extraction-implantation configuration here employed, the use of the AC mode becomes indispensable when higher accelerating voltage values (quite a lot of tens kV) and/or higher ion flux values are required. In such a case, the gap bias voltage has to be delayed for several microseconds with respect to the laser pulse [13] and/or the bias pulse duration has to be suitably reduced with respect to the plasma bunch one. In extreme conditions, single or repeated HV fast pulses, with duration of tens or hundreds ns, might be necessary.

A novel fast pulser has been realized at the Laboratory of Applied Electronics of the Department of Physics of Lecce [55, 56]. Its functioning is based on a transmission line circuit and has been fully described in Chapter 5. Its implementation can be useful to apply HV to the acceleration gap in AC mode, in order to avoid arcing when such a phenomenon can not be controlled or limited in DC mode.



**Fig. 6.1.** *A photograph of the new expansion chamber. Note, in the lower stage, the laser beam inlet port, on which a quartz window will be mounted, and, in the upper stage, the extraction hole, 1 cm in diameter.*

Strictly speaking, such a device is better qualifiable as a “voltage compressor”, since it is able to halve the duration of a pulse in input and to double its voltage amplitude. The input pulse can be provided by an external pulser or can be generated by the “compressor” itself, depending on the experimental configuration employed. The voltage compressor can generate also a series of pulses, if suitably triggered. In fact, the utilization of a train of short HV pulses (50 – 100 ns), with a period of some  $\mu\text{s}$ , is particularly attractive in order to cover the whole duration of the plasma bunch during the extraction stage ( $\sim 15 \mu\text{s}$  at the extraction point in the present set-up), so maximizing the yield of accelerated ions.

## 6.4 Further potential applications of LISs

The previous considerations about LIS advantages and performances for ion implantation remain valid for other applications of LISs as well. In §1.1 the applications in the field of ion accelerators have been underlined. In particular, the employment of LISs for the development of compact accelerators useful in cancer radiotherapy (hadrontherapy) should be stressed.

Apart from LA-ICP-MS, at the moment laser ablation has a rather limited exploitation among the analytical techniques, notwithstanding some extremely interesting characteristics. For example, its exploitation would be particularly favourable in the analysis of radioactive materials, on account of the easiness in sample preparation, the reduced destructivity, the quickness of measurement, and the possibility to treat as usual materials with high boiling point.

The development of LISs would provide extremely powerful and versatile devices immediately applicable in the most common analytical techniques, such as TOF - mass spectrometry, sector field mass spectrometry and quadrupole mass spectrometry. In fact, for many materials and analytical purposes, the ion yield at laser wavelengths in the UV-B/UV-C band and at irradiance values in the order of 0.1 - 1 GW/cm<sup>2</sup> is high enough that further ionization of the ablated aerosol, like in ICP-based devices, could be avoided.

On the grounds of such considerations, it should be particularly interesting the exploitation of LISs in the field of electromagnetic isotope separation. A source based on multiple laser beams, employing a suitably shaped target and operated at high repetition rate (> 100 Hz), would have the potential to fulfill the requirements of the isotope production on industrial scale (time-averaged current higher than 1 mA). In fact, an overall ion yield of the order of or higher than 10 mg/h can be typically expected for a 100 Hz, single-beam LIS, according to the data reported in the literature on laser ablation plasma at 1 – 10 J/cm<sup>2</sup> for a large number of elements.

In this respect, it should be carefully investigated the possibility of employing LISs for uranium enrichment for military purposes via electromagnetic isotope separation, starting from “raw” materials (such as powder of uranium oxide concentrate, suitably compacted or sintered) rather than “higher level” feed materials such as UCl<sub>4</sub> or UF<sub>6</sub>.

# APPENDIX

## An algorithm for pulse mixing deconvolution in LA-ICP-MS measurements

### A.1 Introduction

The experimentally obtained profile in Fig. 4.9 is the result of a series of intermediate processes, whose understanding is important to develop effective data processing procedures. In a first instance, the depth resolution is easily related to the ablation process, considering the average crater depth per pulse. In a second instance, the detection instrumentation, *i.e.*, ICP-MS, digitalizes the analytical (analogical) signal and provides a stream of data points. Obviously, the latter is to be related to the acquisition settings, *e.g.*, number of isotopes, dwell time, settling time and so on. Thus, the time-step between two neighbouring data points gives the minimum depth-related information that can be inferred from the raw analytical signals.

Thereafter, the real analytical signal is turned into a broken line trace, biased by the set-up-induced signal dispersion. This phenomenon causes an overlap of signals related to different depths in the sample, altering the actual depth profile of the implanted analyte, so that all the acquired LA-ICP-MS raw signals need to be processed to extract correct analytical information.

Such a problem was particularly evident on the LIS-implanted samples investigated in the present work, owing to their shallow implantation depth. Aim of this Appendix is to describe the procedures developed for pulse mixing deconvolution and correction of tailing effects in LA-ICP-MS experimental signals.

### A.2 Mathematical foundations

It has been shown [82] that the signal intensity of a LA-ICP-MS measurement can be put into relation to the operating conditions by the following relation:

$$I(t) = I_o \cdot \left(1 - \frac{T_0}{t}\right) \cdot e^{-\frac{F}{V}(t-T_0)} \cdot u(t-T_0) \quad (\text{A.1})$$

where  $I(t)$  is the signal intensity at the time  $t$  from the laser action ( $t = 0$ );  $I_o$  is a multiplicative factor proportional to the analyte concentration in the sample and determines the signal peak intensity;  $T_o$  is the transfer time to transport the laser-induced aerosol from the sampling site to the detection unit (*i.e.*, proportional to the tube length);  $F$  is the carrier gas flow rate;  $V$  is the volume of the ablation cell; and  $u$  is the Heaviside step function.

The relation defines the profile of a single shot, whereas for continuous ablation one needs to sum the equation over the whole number of shots. So, denoting by  $t_i$  ( $i = 0, 1, 2, \dots$ ) the generic time at which the  $(i + 1)$ -th laser pulse is delivered, the related signal  $I_i(t)$  follows straightforward to be expressed by:

$$I_i(t) = I_{o,i} \cdot \left(1 - \frac{T_o}{t - t_i}\right) \cdot e^{-k[t - (T_o + t_i)]} \cdot u[t - (T_o + t_i)] \quad (\text{A.2})$$

where the constant  $k = F/V$  has been introduced. For continuous ablation with a laser repetition rate  $f$ ,  $t_i$  is given by the simple relation:

$$t_i = i \cdot \Delta \quad (\text{A.3})$$

where  $\Delta = 1/f$ . The corresponding ablation depth, or, better, ablation depth range,  $D_i$  can be written, in terms of  $t_i$ , as:

$$D_i = [t_i f d, d \cdot (t_i f + 1)] \quad (\text{A.4})$$

where  $d$  is the ablation depth per pulse. The cumulative signal  $\tilde{I}(t)$ , for  $t < t_n$ , is then given by the following expression:

$$\tilde{I}(t) = \sum_{i=0}^{n-1} I_i(t) \quad , \quad t < t_n \quad (\text{A.5})$$

Note that, under the approximation  $T_0 \approx 0$  (practically valid for a transfer time shorter than 1 - 2 s, *i.e.*, tube length shorter than 1.5 m at a carrier gas velocity of 80 - 100 cm/s), Eq. (A.2) simplifies to curves with a sharp leading edge, decreasing in accordance with a purely exponential law (see Fig. A.1):

$$I_i(t) \approx I_{o,i} \cdot e^{-k(t-t_i)} \cdot u(t-t_i) \quad (\text{A.6})$$

As a consequence, Eq. (A.5) can be put in the useful form:

$$\tilde{I}(t) \approx e^{-k(t-t_{n-1})} \sum_{i=0}^{n-1} I_{0,i} e^{-k(t_{n-1}-t_i)} \quad , \quad t_{n-1} \leq t < t_n \quad (\text{A.7})$$

Now, one can recognize, from Eqs. (A.5) and (A.6), that the sum in Eq. (A.7) is just  $\tilde{I}(t_{n-1})$ . So, Eq. (A.7) can be re-written as:

$$\tilde{I}(t) \approx \tilde{I}(t_{n-1}) \cdot e^{-k(t-t_{n-1})} \quad , \quad t_{n-1} \leq t < t_n \quad (\text{A.8})$$

Such a factorisation can be favourably used to implement an algorithm for data deconvolution. If the signal detection rate coincides with the laser pulse rate ( $f$ ) and the time difference between ablation and detection is negligible ( $T_0 \approx 0$ ), data points at times  $t_i$  are obtained,  $\tilde{I}(t_i)$ , each in coincidence with the arrival of the leading edge (and hence the intensity peak value) of a single pulse signal. Finally, it is now straightforward to derive from Eq. (A.8) the following algorithm, which can be used to extract the physically significant quantity  $I_{0,n}$  from the generic  $n$ -th data point:

$$\tilde{I}(t_n) = \tilde{I}(t_{n-1}) \cdot e^{-k\Delta} + I_{0,n} \quad (\text{A.9})$$

In practice, a little shift  $\delta$  between the detection time and the ablation time should be considered to take into account a finite value of  $T_0$ , even if small. In order to sample  $\tilde{I}(t)$  on the arrival of the maximum,  $I_{max,i}$ , of each single pulse signal, the detection time,  $t'_i$ , has to be set as:

$$t'_i = t_i + \delta \quad (\text{A.10})$$

where  $\delta$  is given by the following relation expressing the point of maximum of Eq. (A.1):

$$\delta = \frac{1 + \sqrt{1 + \frac{4}{kT_0}}}{2} \cdot T_0 \quad (\text{A.11})$$

Moreover, for  $T_0 \ll \Delta$ , Eq. (A.1) can be anyway approximated by an exponential function for  $t \gtrsim \Delta$ . So, under the further approximation  $kT_0 \ll 1$ , Eq. (A.9) can be modified as it follows:

$$\tilde{I}(t'_n) \approx \tilde{I}(t'_{n-1}) \cdot e^{-k\Delta} + I_{\max,n} \quad (\text{A.12})$$

where  $I_{\max,n}$  is related to  $I_{0,n}$  by the calculation of the maximum of Eq. (A.2), at  $t = t_i + \delta$ :

$$I_{\max,n} = I_{0,n} \cdot \left(1 - \frac{T_0}{\delta}\right) \cdot e^{-k(\delta - T_0)} \quad (\text{A.13})$$

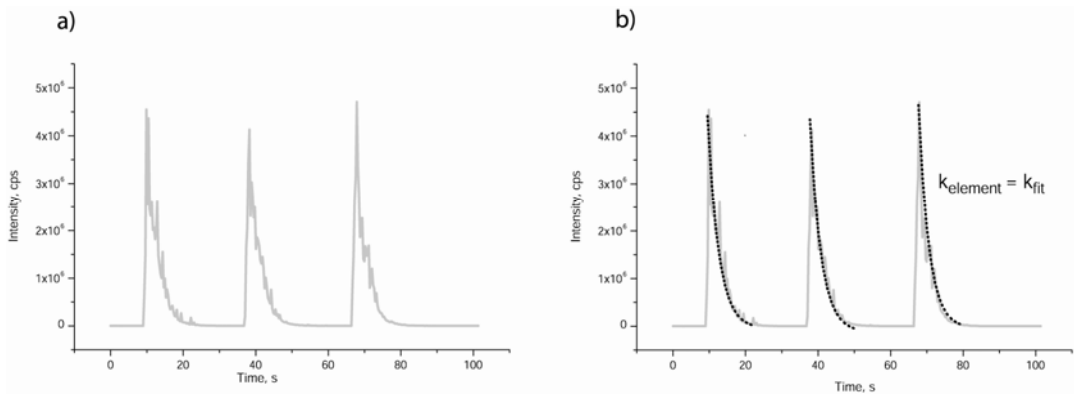


**Fig. A.1.** Individual signals from single shots are acquired each at a time (a). Then the experimental signals are fitted and the signal waning constant,  $k$ , is determined (b).

### A.3 Experimental implementation

First of all, one needs to record the profile of the single pulse signal and to determine experimentally the waning constant,  $k$ , which describes the signal exponential decay. To do this, one can either ablate a sample in single shot mode and then fit the peaks (Fig. A.1), or, after the completion of the depth profile acquisition, stop the ablation and acquire the waning leg (Fig. A.2). In this way, one might fit the terminal part of the analytical signals in order to obtain information on the signal waning constant for any individual analyte.

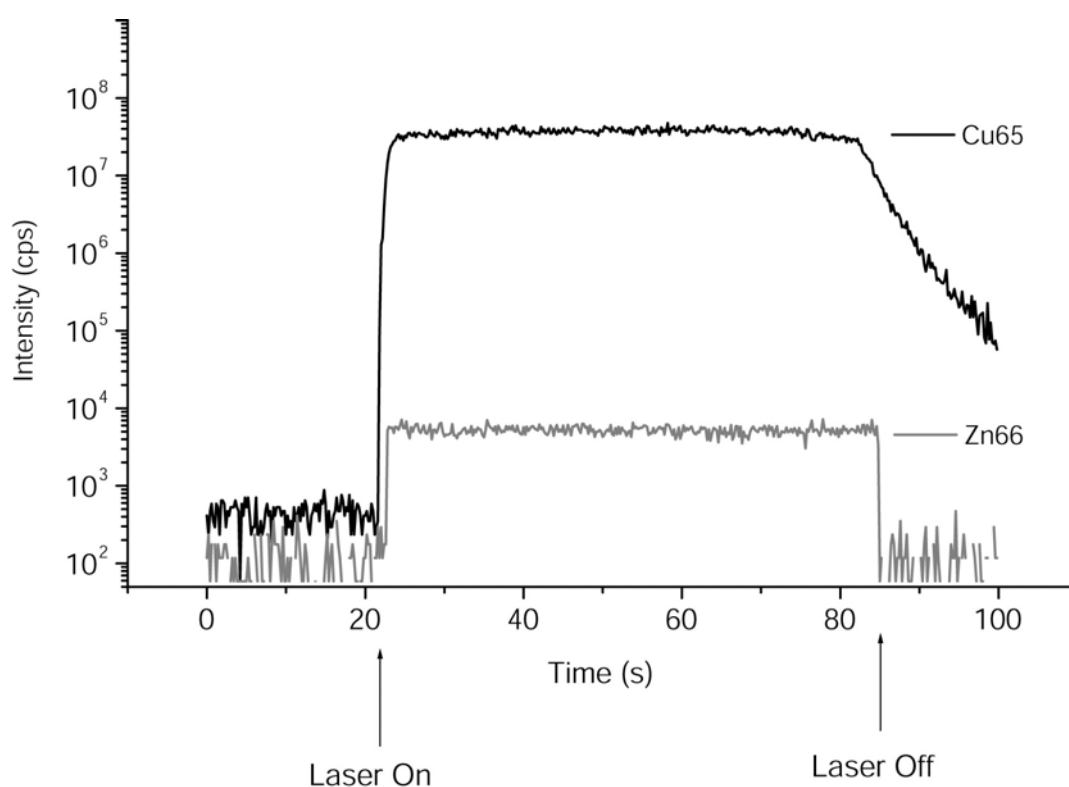


**Fig. A.2.** LA-ICP-MS signals of Cu and Zn as obtained from the ablation of a Cu sample with traces of Zn. Note the different waning times, depending on the abundance of the elements introduced into the measurement set-up.

In Fig. A.1a a sequence of single shots is shown, that are experimentally fitted in Fig. A.1b. Once one has plotted the signal profile, this curve defines a set of data

points that provide information derived from the same depth within the sample. Of course, if signal tailing did not occur, then such a set of data points should lie on a narrow line (spike). The signal width (FWHM) is reported in Fig. A.3 as a function of the carrier gas flow through the ablation cell, which is one of the experimental set-up parameters influencing signal dispersion.

Figure A.4 shows the Ge depth profile derived from the trace of Fig. 4.9 after signal processing with the present method. The bin width is about 90 nm. Apart from the different depth resolution, the reconstructed profile is not in good agreement with the one acquired by single shot profiling (Fig. 4.11). In particular, the relative height of the first two bars of the histogram in Fig. A.4 is unacceptable. Depth profiling was surely affected by crater effects as well as by the noise of the LA-ICP-MS signals, which influenced the goodness of the fitting procedure and decay rate constant determination.

Measurements in the Si(100) samples resulted in a signal waning constant  $k_{Ge} = 1.25 \text{ s}^{-1}$  for Ge, which is slightly different from the  $k_{Al} = 1.30 \text{ s}^{-1}$  for Al and  $k_{Cu} = 1.50 \text{ s}^{-1}$  for Cu. Element-dependent flush speed is the direct consequence of the element-dependent distribution of the laser-induced aerosol particles in classes of different size. Calculation of the flush frequency  $k$  from the ratio of the experimental carrier gas flow rate ( $F = 0.9 \text{ l/min}$ ) and the volume of the ablation cell ( $V = 30 \text{ ml}$ ) gives an expected value of  $k = F/V = 0.5 \text{ s}^{-1}$ . It probably indicates that calculations based on 30 ml cell volume, *i.e.*, the geometric size, are considering also dead volume regions, *i.e.*, regions where the carrier gas does not sweep the cell efficiently or at all. The measured value  $k_{Ge} = 1.25 \text{ s}^{-1}$  permits to calculate that, for  $F = 0.9 \text{ l/min}$ , the effective flushed cell volume is about  $V = 12 \text{ ml}$ , *i.e.*, 40% of the whole geometric volume.

Moreover, the signal decay law can divert from a pure exponential function on an intensity range of several orders of magnitude (see the Cu trace in the graph of Fig. A.2, where a semi-logarithmic scale is used). The operative difficulties in a precise determination of  $k$  and its possible variations during signal waning are the most delicate points in the practical implementation of the deconvolution algorithm here presented.

Nevertheless, the employment of the algorithm on the analysis of a deeper implant was satisfactory, and the results were in good agreement with the theoretical

expectations. A glassy carbon substrate implanted with high energy Ge ions was analysed, by employing the same experimental set-up previously utilized for the measurements on the Si substrates with a laser repetition rate of 10 Hz.

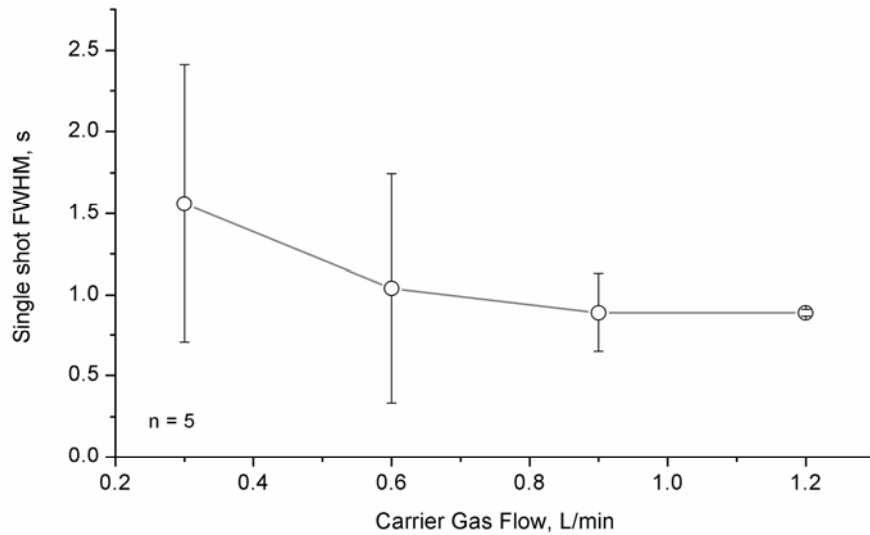


**Fig. A.3.** Signal dispersion (FWHM) as a function of the carrier gas flow rate through the ablation cell. Statistics on five laser shots ( $n = 5$ ) for each data point was applied.

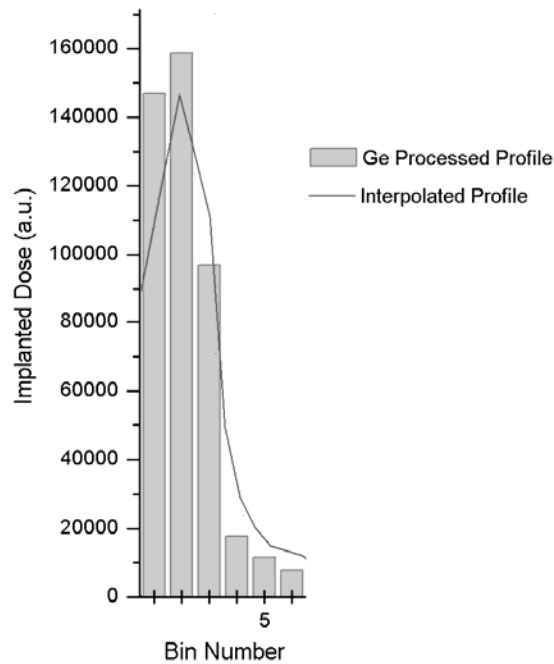


**Fig. A.4.** Depth profile of Ge implanted in Si(100) after signal processing to overcome pulse mixing. Bin width is about 90 nm.

The implantation was carried out at the PALS (Prague Asterix Laser System) Research Centre of the Academy of Sciences of the Czech Republic, in Prague. Implanting ions were produced by irradiating in vacuum a Ge target with an intense laser beam (438 nm wavelength, 400 ps pulse length, 40 J pulse energy, focused beam spot diameter of 100  $\mu\text{m}$ ) emitted by the high power iodine laser PALS (third harmonic) [38]. The laser power density was of the order of  $10^{16}$  W/cm<sup>2</sup>. Ions with very high charge states (even higher than +25) and kinetic energy up to 4 MeV were generated in such irradiance conditions. These ions implanted directly into the substrate, without the employment of an external electric field. Ten laser shots were delivered, yielding an ion dose of about  $3 \cdot 10^{14}$  ions/cm<sup>2</sup> at the substrate position.

LA-ICP-MS depth profiling is shown in Fig. A.5. The ablation rate was about 100 nm per laser shot. The significant implantation depth was higher than 1  $\mu\text{m}$ .

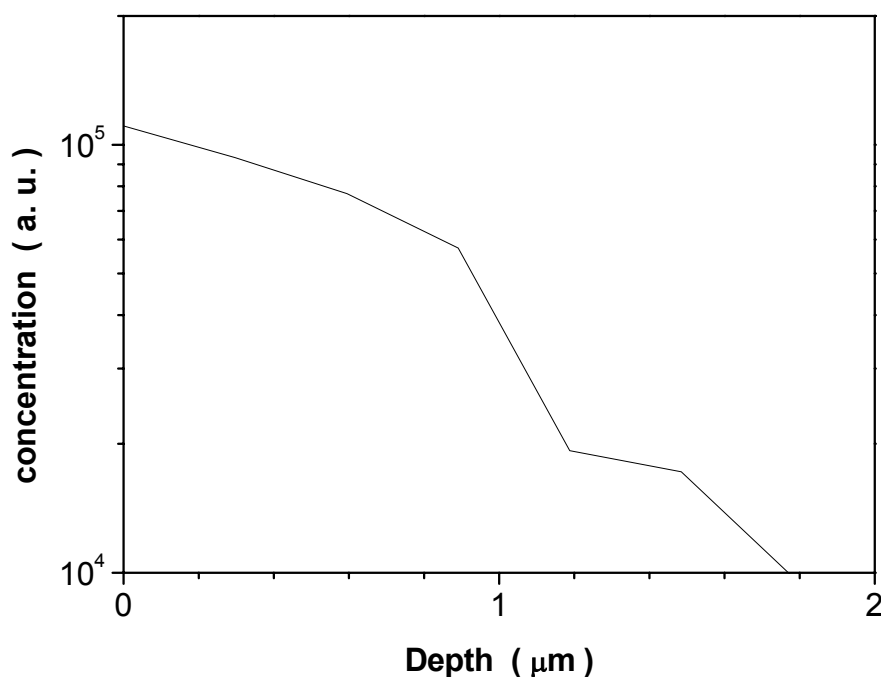


**Fig. A.5.** LA-ICP-MS depth profile of a glassy carbon sample implanted with high energy Ge ions generated by the PALS laser beam. The deconvolution algorithm was applied to the original LA-ICP-MS signal in the time domain. Depth resolution was about 100 nm.

## REFERENCES

1. R. Kelly and R. W. Dreyfus, *Surf. Sci.* **198**, 263 (1988).
2. V. Nassisi, F. Belloni, D. Doria and A. Lorusso, in: *Plasma Production by Laser Ablation (PPLA 2003)*, S. Gammino, A. M. Mezzasalma, F. Neri, L. Torrisci, Eds., World Scientific Publishing, Singapore, 2004, pp. 127 - 132.
3. F. Belloni, D. Doria, A. Lorusso and V. Nassisi, in: *Plasma Production by Laser Ablation (PPLA 2003)*, S. Gammino, A. M. Mezzasalma, F. Neri, L. Torrisci, Eds., World Scientific Publishing, Singapore, 2004, pp. 156 - 162.
4. L. Torrisci, S. Gammino, L. Andò and L. Laska, *J. Appl. Phys.* **91**, 4685 (2002).
5. D. Doria, F. Belloni, A. Lorusso and V. Nassisi, in: *Plasma Production by Laser Ablation (PPLA 2003)*, S. Gammino, A. M. Mezzasalma, F. Neri, L. Torrisci, Eds., World Scientific Publishing, Singapore, 2004, pp. 170 - 176.
6. L. Laska, K. Jungwirth, B. Kralikova, J. Krasa, E. Krousky, K. Masek, M. Pfeifer, K. Rohlena, J. Skala, J. Ullschmied, J. Badziak, P. Parys, L. Ryc, A. Szydlowski, J. Wolowski, E. Woryna, G. Ciavola, S. Gammino, L. Torrisci and F. P. Boody, *Rev. Sci. Instrum.* **75**, 1546 (2004).
7. S. Gammino, L. Torrisci, G. Ciavola, L. Andò, L. Celona, S. Manciangli, J. Krasa, L. Laska, M. Pfeifer, K. Rohlena, A. M. Mezzasalma, C. Gentile, A. Picciotto, J. Wolowski, E. Woryna, J. Badziak, P. Parys, D. Hitz and G. D. Shirkov, *J. Appl. Phys.*, **96**, 2961 (2004).
8. D. B. Chrisey and G. K. Hubler, Eds., *Pulsed Laser Deposition of Thin Film*, Wiley, New York, 1994, pp. 117-118.
9. I. V. Roudskoy, *Laser Part. Beams* **14**, 369 (1996).
10. L. Laska, J. Krasa, M. Pfeifer, K. Rohlena, S. Gammino, L. Torrisci, L. Andò and G. Ciavola, *Rev. Sci. Instrum.* **73**, 654 (2002).
11. T. R. Sherwood, *Rev. Sci. Instrum.* **63**, 2789 (1992).
12. H. Haseroth and H. Hora, *Laser Part. Beams* **14**, 393 (1996).
13. B. Qi, R. M. Gilgenbach, M. C. Jones, M. D. Johnston, Y. Y. Lau, L. M. Wang, J. Lian, G. L. Doll and A. Lazarides, *J. Appl. Phys.* **93**, 8876 (2003).
14. F. Belloni, D. Doria, A. Lorusso, V. Nassisi, L. Torrisci, L. Calcagnile, G. Quarta, D. Bleiner and D. Manno, *Nucl. Instrum. Meth. B* **240**, 36 (2005).
15. M. Rosinski, J. Badziak, F. P. Boody, S. Gammino, H. Hora, J. Krasa, L. Laska, A. M. Mezzasalma, P. Parys, K. Rohlena, L. Torrisci, J. Ullschmied, J. Wolowski, E. Woryna, *Vacuum* **78**, 435 (2005).

16. G. Dearnaley, J. H. Freeman, R. S. Nelson and J. Stephen, *Ion Implantation*, American Elsevier Publishing Co., New York, 1973.
17. E. Rimini, *Ion Implantation: Basics to Device Fabrication*, Kluwer Academic Publishers, Boston, 1995.
18. L. Rubin and W. Morris, *Semicond. Internat.* **20**, 77 (1997).
19. H. Ryssel and I. Ruge, *Ion Implantation*, John Wiley and Sons, New York, 1986.
20. J. F. Ziegler, Ed., *Ion Implantation: Science and Technology*, Ion Implant Technology Co., Edgewater, 2000.
21. E. Chason, *J. Appl. Phys.* **81**, 6513 (1997).
22. M. I. Current, *J. Vac. Sci. Tech. A* **14**, 1115 (1996).
23. J. R. Conrad, J. L. Radtke, R. A. Dodd, J. Worzala and N. C. Tran, *J. Appl. Phys.* **62**, 4591 (1987).
24. J. R. Conrad, U.S. Patent No. 4764394 (1988).
25. J. T. Sheuer, M. Shamim and J. R. Conrad, *J. Appl. Phys.* **67**, 1241 (1990).
26. R. P. Fetherston, M. M. Shamim and J. R. Conrad, U.S. Patent No. 5693376 (1997).
27. P. K. Chu, S. Qin, C. Chan, N. W. Cheung and L. A. Larson, *Material Science and Engineering* **R17**, 207 (1996).
28. D. J. Rej, R. J. Faehl and J. N. Matossian, *Surface and Coatings Technology* **96**, 45 (1997).
29. A. Anders, Ed., *Handbook of Plasma Immersion Ion Implantation*, Wiley, New York, 2000.
30. S. Qin, N. McGruer, C. Chan and K. Warner, *IEEE Trans. Electron Devices* **39**, 2354 (1992).
31. B. P. Wood, I. Henins, D. J. Rej, H. A. Davis, W. Waganaar, R. E. Muenchausen, G. P. Johnson and H. K. Schmidt, *Nucl. Instrum. Meth. B* **96**, 429 (1995).
32. I. G. Brown, *Rev. Sci. Instrum.* **65**, 3062 (1994).
33. B. Qi, R. M. Gilgenbach, Y. Y. Lau, M. D. Johnston, J. Lian, L. M. Wang, G. L. Doll and A. Lazarides, *Appl. Phys. Lett.* **78**, 3785 (2001).
34. B. Qi, Y. Y. Lau and R. M. Gilgenbach, *Appl. Phys. Lett.* **78**, 706 (2001).
35. F. P. Boody, R. Hopfl, H. Hora and J. C. Kelly, *Laser Part. Beams* **14**, 443 (1996).

36. L. Torrisci, S. Gammino, A. M. Mezzasalma, J. Badziak, P. Parys, J. Wolowski, E. Woryna, J. Krása, L. Láska, M. Pfeifer, K. Rohlena and F. P. Boody, *Appl. Surf. Sci.* **217**, 319 (2003).
37. D. Bleiner, F. Belloni, D. Doria, A. Lorusso and V. Nassisi, *J. Anal. At. Spectrom.* **20**, 1337 (2005).
38. A. Lorusso, F. Belloni, D. Doria, V. Nassisi, J. Wolowski, J. Badziak, P. Parys, J. Krása, L. Láska, F. P. Boody, L. Torrisci, A. Mezzasalma, A. Picciotto, S. Gammino, L. Calcagnile, G. Quarta and D. Bleiner, *Nucl. Instrum. Meth. B* **240**, 229 (2005).
39. D. J. Rej, *Handbook of Thin Film Process Technology*, Institute of Physics, Philadelphia, 1996.
40. R. E. Clausing, L. L. Horton, J. C. Angus and P. Kiodl, *Diamond and Diamond-like Films and Coatings*, Plenum, New York, 1991.
41. X. He, W. Li and H. Li, *J. Vac. Sci. Technol. A* **14**, 2039 (1996).
42. S. Neuville and A. Matthews, *Matt. Res. Bull.* **22**, 22 (1997).
43. N. G. Utterback, S. P. Tang and J. F. Friichtenicht, *Phys. Fluids* **19**, 900 (1976).
44. J. C. S. Kools, T. S. Baller, S. T. De Zwart and J. Dieleman, *J. Appl. Phys.* **71**, 4547 (1992).
45. J. Lindhard, M. Scharff and H. E. Schiott, *Mat. Fys. Medd. Dan. Vid. Selsk.* **33**, n. 14 (1963).
46. H. A. Bethe and J. Ashkin, "Passage of radiations through matter", in: *Experimental Nuclear Physics*, vol. 1, E. Segrè, Ed., John Wiley & Sons, New York, 1953.
47. S. K. Ghandhi, P. Kwan, K. N. Bath and J. M. Borrego, *IEEE Electron Device Letters* **3**, 48 (1982).
48. J. F. Ziegler and J. P. Biersack, software SRIM-2003 ([www.srim.org](http://www.srim.org)), 2003.
49. J. F. Ziegler, J. P. Biersack and U. Littmark, *The Stopping and Range of Ions in Solids*, Pergamon Press, New York, 1985.
50. A. Lorusso, F. Belloni, D. Doria and V. Nassisi, in: *Plasma Production by Laser Ablation (PPLA 2003)*, S. Gammino, A. M. Mezzasalma, F. Neri, L. Torrisci, Eds., World Scientific Publishing, Singapore, 2004, pp. 184 - 190.
51. D. Doria, A. Lorusso, F. Belloni and V. Nassisi, *J. Plasma Phys.* **72**, 229 (2006).
52. F. Belloni, D. Doria, A. Lorusso and V. Nassisi, *Rev. Sci. Instrum.* **75**, 4763 (2004).

53. L. Marra, F. Belloni, A. Lorusso, L. Martina and V. Nassisi, *Rad. Eff. Def. Solids* **160**, 621 (2005).
54. F. Belloni, D. Doria, A. Lorusso and V. Nassisi, *Proceedings del XVII Congresso dell'Associazione Italiana del Vuoto*, Venezia Lido, Italy, June 28 – July 2, 2004, pp. 55 – 60.
55. V. Nassisi, F. Belloni, D. Doria and A. Lorusso, *Rev. Sci. Instrum.* **74**, 5201 (2003).
56. F. Belloni, D. Doria, V. Nassisi and G. Palamà, *Nucl. Instrum. Meth. A* **537**, 614 (2005).
57. A. Lorusso, J. Krasa, K. Rohlena, V. Nassisi, F. Belloni and D. Doria, *Appl. Phys. Lett.* **86**, 081501 (2005).
58. D. Doria, F. Belloni, A. Lorusso, J. Krása, V. Nassisi, K. Rohlena and L. Velardi, *Rad. Eff. Def. Solids* **160**, 663 (2005) .
59. A. Lorusso, F. Belloni, D. Doria, V. Nassisi, J. Krása and K. Rohlena, *J. Phys. D: Appl. Phys.* **39**, 294 (2006).
60. E. Woryna, P. Parys, J. Wolowski and W. Mroz, *Laser Part. Beams* **14**, 293 (1996).
61. V. Nassisi and A. Pedone, *Rev. Sci. Instrum.* **74**, 68 (2003).
62. D. Doria, A. Lorusso, F. Belloni, V. Nassisi, L. Torrisi and S. Gammino, *Laser Part. Beams* **22**, 461 (2004).
63. H. Bubert and H. Jenett, Eds., *Surface and Thin Film Analysis*, Wiley-VCH, Chichester, 2002.
64. D. Bleiner, P. Lienemann, A. Ulrich, H. Vonmont and A. Wichser, *J. Anal. At. Spectrom.* **18**, 1146 (2003).
65. F. Belloni, D. Doria, A. Lorusso, V. Nassisi and J. Krasa, *Rev. Sci. Instrum.* **77**, 03B301 (2006).
66. D. Doria, A. Lorusso, F. Belloni, V. Nassisi, L. Torrisi and S. Gammino, *Proceedings del XVII Congresso dell'Associazione Italiana del Vuoto*, Venezia Lido, Italy, June 28 – July 2, 2004, pp. 195 – 199.
67. J. Krasa, A. Lorusso, D. Doria, F. Belloni, V. Nassisi and K. Rohlena, *Plasma Phys. Control. Fusion* **47**, 1339 (2005).
68. F. Belloni, D. Doria, A. Lorusso, V. Nassisi and L. Torrisi, *Proc. SPIE Int. Soc. Opt. Eng.* **5777**, 974 (2005).
69. F. Belloni, D. Doria, A. Lorusso and V. Nassisi, *Nucl. Instrum. Meth. B* **240**, 40 (2005).

70. J. Narayan and O. W. Holland, *J. Appl. Phys.* **56**, 2913 (1984).
71. J. H. Barnes, G. D. Schilling, G. M. Hieftje, R. P. Sperline, M. Bonner Denton, C. J. Barinaga and D. W. Koppenaal, *J. Am. Soc. Mass Spectrom.* **15**, 769 (2004).
72. D. Bleiner, *Spectrochim. Acta B* **60**, 49 (2005).
73. V. Margetic, K. Niemax and R. Hergenröder, *Anal. Chem.* **75**, 3435 (2003).
74. R. E. Russo, X. L. Mao, O. V. Borisov and H. Liu, *J. Anal. At. Spectrom.* **15**, 1115 (2000).
75. A. Luches, V. Nassisi, A. Perrone and M. R. Perrone, *Physica* **104C**, 228 (1981).
76. S. D. Korovin, G. A. Mesyats, V. V. Rostov, M. R. Ul'maskulov, K. A. Sharypov, V. G. Shpak, S. A. Shunailov and M. I. Yalandin, *Techn. Phys. Lett.* **28**, 81 (2002).
77. L. Shao-chi, B. Zhi-xiang, G. Guang-yuan, T. Shi-qing, W. Yun-rong, *Appl. Phys. Lett.* **38**, 328 (1981).
78. V. Nassisi, *Appl. Phys. B* **53**, 14 (1991).
79. A. C. Kolb, *IEEE Trans. Nucl. Sci.* **22**, 956 (1975).
80. V. Nassisi and A. Pedone, *INFN Technical Report*, INFN/TC-02/28 (2002).
81. *PSpice8* by MicroSim Inc.
82. D. Bleiner, Ph.D. thesis, ETH dissertation no. 14665, 2002.

## **LIST OF THE MAIN ABBREVIATIONS**

AC : Alternating Current

DC : Direct Current

DLC : Diamond-Like-Carbon

EC : Expansion Chamber

ECR : Electron Cyclotron Resonance

ECRIS : Electron Cyclotron Resonance Ion Source

EDX : Energy Dispersive X-ray spectroscopy

FC : Faraday Cup

FWHM : Full Width at Half Maximum

GE : Grounded Electrode

HV : High Voltage

IBAD : Ion Beam Assisted Deposition

ICP : Inductively Coupled Plasma

IEA : Ion Energy Analyzer

LA-ICP-MS : Laser Ablation – Inductively Coupled Plasma – Mass Spectrometry

LIS : Laser Ion Source

NVC : Novel Voltage Compressor

PBF : Potential Barrier Filter

PIII : Plasma Immersion Ion Implantation

PLD : Pulsed Laser Deposition

RBS : Rutherford Backscattering Spectrometry

RF : Radio-Frequency

SEM : Scanning Electron Microscope

SL : Storage Line

SNR: Signal-to-Noise Ratio

SPFL : Single Pulse Forming Line

SR : Suppression Ring

TL : Transmission Line

TOF : Time Of Flight

XPS : X-ray Photo-electron Spectrometry

## ACKNOWLEDGEMENTS

I would like to express my acknowledgement to several people, who have made this thesis possible.

First and foremost, I thank my Ph.D. supervisor, Prof. Vincenzo Nassisi, Responsible of the Laboratory of Applied Electronics of the Department of Physics of the University of Lecce, Italy. I thank him for offering this work, which I found challenging and rewarding. This work would not have been possible without his experience and dedication. I am thankful for his unwavering support and encouragement during my doctoral studies.

Prof. L. Torrisi (Laboratori Nazionali del Sud – INFN, Catania, Italy, and University of Messina, Messina, Italy) is acknowledged for the experiments carried out at Laboratori Nazionali del Sud – INFN and for invaluable suggestions.

Dr. J. Krasa and Dr. K. Rohlena are acknowledged for offering a three-months “Marie Curie” fellowship at the Institute of Physics of the Academy of Sciences of the Czech Republic, in Prague. In particular, Dr. Krasa is acknowledged for stimulating discussions and invaluable suggestions.

Dr. D. Bleiner (Department of Chemistry, University of Antwerp, Belgium) and Dr. M. Dobeli (Paul Scherrer Institute and ETH, Zurich, Switzerland) are acknowledged for the RBS measurements. Dr. Bleiner is also acknowledged for stimulating discussions and for the LA-ICP-MS analyses when he worked at the Swiss Federal Laboratories for Materials Research (EMPA), Duebendorf, Switzerland.

Prof. L. Calcagnile (Department of Engineering of Innovation and CEDAD, University of Lecce, Italy) is also acknowledged for the RBS measurements.

Prof. A. Perrone (Department of Physics, University of Lecce, Italy) and Dr. H. Du (Advanced Materials Research Institute, University of Northumbria, Newcastle, UK) are acknowledged for the XPS analyses.

Prof. D. Manno (Department of Materials Science, University of Lecce, Italy) is acknowledged for the SEM-EDX analyses.

Mr. V. Nicolardi (Department of Physics, University of Lecce, Italy) is acknowledged for his invaluable technical support in the experimental activity.

Miss Cristina Belloni is acknowledged for her kind support in the manuscript paging.